Last Copy
do not Remove

ROTOR WAKE BEHAVIOR IN A TRANSONIC COMPRESSOR STAGE AND ITS EFFECT ON THE LOADING AND PERFORMANCE OF THE STATOR

Mohammad Durali

GT&PDL Report No. 149 April 1980

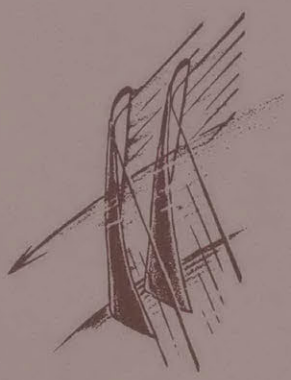

GAS TURBINE & PLASMA DYNAMICS LABORATORY
MASSACHUSETTS INSTITUTE OF TECHNOLOGY
CAMBRIDGE, MASSACHUSETTS

ROTOR WAKE BEHAVIOR IN A TRANSONIC COMPRESSOR STAGE AND ITS EFFECT ON THE LOADING AND PERFORMANCE OF THE STATOR

Mohammad Durali

GT&PDL Report No. 149 April 1980

This research, carried out in the Gas Turbine and Plasma Dynamics Laboratory, MIT, was supported by the NASA Lewis Research Center under Grant No. NGL-22-009-383.

ABSTRACT

The structure and behavior of wakes from a transonic compressor rotor and their effects on the loading and performance of the downstream stator have been studied experimentally.

The rotor is 2 feet in diameter with a tip Mach number of 1.23 and a measured pressure ratio of 1.66. Time and space resolved measurements have been completed of the rotor and stator outlet flows, as well as of the pressure distribution on the surface of the stator blades. The data is analyzed and the rotor-stator viscous interaction is studied both qualitatively and quantitatively.

It is found that the wakes from this rotor have large flow angle and flow Mach number variations from the mean flow, significant pressure fluctuations and a large degree of variation from blade to blade and from hub to tip. There is a significant total pressure defect and practically no static pressure variation associated with the stator wakes. Wakes from the rotor exist nearly undiminished in the exit flow of the stator and decay in the annular duct behind the stator.

The pressure at all the points along the chord over each of the stator blades' surfaces, fluctuates nearly in phase in response to the rotor wakes, that is the unsteady chordwise pressure distribution is determined by the changes in angle of incidence to the blade and not by the local velocity fluctuations within the passage. There are large unsteady forces on the stator blade, induced by the rotor wakes, as high as 25% of the steady forces.

The stator force due to the rotor wakes lags the incidence of the wake on the leading edge by approximately 180^{0} for most radii.

TABLE OF CONTENTS

LIST OF SYMBOLS

A	area
a	speed of sound
c	blade chord length
cp	specific heat
k	compressible reduced frequency
M	Mach number
P, p	pressure
P_i	pressure at ith diaphragm on the probe
P_s	static pressure
PS_i	ith transducer on stator blade pressure surface
P_t	total pressure
R	gas constant
R	radius
SS_i	ith transducer on stator blade suction surface
T	temperature
T	time normalized by blade passing period
t	time
U	rotor rotational velocity
V	flow velocity
$\dot{w}$	mass flow rate
x	distance along the chord
α	blade angle
β	flow angle

θ	tangential flow angle
γ	stagger angle
γ	ratio of specific heat
σ	blade solidity
ϕ	radial flow angle
Φ	turning angle
η	efficiency
ω	frequency, rad/sec
Ω	reduced frequency $\Omega = c\omega/2V$
ρ	density

Subscripts

t	tip
t	stagnation conditions
r	in relative coordinates
θ	in tangential direction
x	in axial direction

LIST OF FIGURES

CHAPTER 1

INTRODUCTION

In recent years transonic compressors and fans have received much attention from aircraft engine designers. This is due to the improvements made in thrust-to-weight ratio of the aircraft engine by using high pressure ratio transonic compressor stages. Typical stages of this kind have a rotor that operates with moderate supersonic relative velocities near the tip and high subsonic velocities near the hub. The high overall pressure ratio of such stages requires the outflow from the rotor to have large swirl and high subsonic velocities.

The swirl put into the air by the rotor has to be removed by stator blades before flow enters the next stage. A significant fraction of overall static pressure rise across the stage comes from the removal of this swirl by the stator. Flow through the stator is very unsteady as a result of the rotor wakes being transported through the stator passages.

The rotor wakes subject the stator to large changes in incidence angle and as they are transported through the blade row they subject the suction surfaces to unfavorable pressure gradients and impinge on the pressure surface of the stator blades. These effects result in large unsteady forces on the blades and potentially to increased viscous losses.

Time averaged pressure measurements carried out between the blade rows using stagnation pressure probes, hold the stators responsible for one-third of the overall stage losses. But a time averaging measurement

of this kind does not yield information about the mechanism by which the losses due to unsteadiness in the stator occur. The aeroelastic response of the stator to excitation by rotor wakes, and fan noise generated as a result of rotor wakes interacting with stators are other important phenomena which deserve extensive detailed studies if optimum designs are to be achieved.

Current design practice assumes flow at a mean angle and Mach number and uses experimental results from two dimensional cascades tested in steady state flow, to calculate the required blade solidity and geometry. Although this method has given acceptable results, it clearly does not form a basis for an optimum design to minimize the losses due to unsteady flow.

The complex flow field associated with the interaction between the blades in a compressor has limited theoretical studies to two dimensional, inviscid flow through cascades of simple geometries. The well known formulations of Kemp and Sears [1,2] for aerodynamic interference between moving blade rows have been extended by Horlock [4] to include chordwise gusts.

Experimental measurements of pressure on isolated airfoils in unsteady flow have supplied a great deal of information about the unsteady flow over airfoils for example [13,15], but comparable data for cascades is scarce. Blade measurements of unsteady pressure have been done at mid-span on stator blades of low speed high hub-to-tip radius ratio test compressors [5,6,7], but these results leave open many questions concerning

the effects of compressibility and hub-to-tip variation in highly loaded transonic stages. The rotor wakes in a highly loaded transonic compressor may be very different from those modeled by two dimensional theories or found in low speed stages, having large radial flows, significant pressure fluctuations and a high degree of variation from blade to blade and from hub to tip [8].

There is therefore a need for documentation of the rotor wakes structure and interaction with the stator in a typical transonic stage, to provide a basis for development of more accurate models for the rotor-stator interaction in transonic compressor stages. The objective of this research was to construct a data base that will contribute to meeting this need.

The M.I.T. Transonic Compressor is typical in the sense of having a normal tip Mach number of 1.2, pressure ratio of 1.6 and conventional blade shapes. It is not a highly developed design, hence it has somewhat higher losses than the best contemporary stages with these design parameters. But this is not considered a serious disadvantage for the present purposes of advancing the phenomenological understanding of the rotor-stator interaction.

For this study one stator blade was instrumented with high frequency miniature pressure transducers to allow time resolved measurements on both the suction and pressure surfaces. The instrumented blade was made to traverse radially across the annulus to obtain the distributions of static pressure on the blade as a function of time at all radii. The steady and unsteady loads on the stator blades can then be calculated

by integration of the pressure over the blade surfaces.

In order to relate the response of the stator blades to the wakes from the rotor, time resolved radial and circumferential surveys of the flow fields behind the rotor and behind the stator were also carried out. Such data gives information about the structure and the frequency content of the rotor wakes before and after interaction with the stator. It is obtained by using the M.I.T. miniature pressure probe (also known as the 5-way probe), [10], to survey the flow field behind the rotor and behind the stator. Radial surveys with the probe behind the rotor furnish measurements by which the flow angles, total and static pressure and flow Mach numbers can be calculated (as a function of time and radial and circumferential positions).

A similar time resolved map of flow properties behind the stator was obtained by replacing the traversing blade with another blade similar to the rest of the stator blades, and allowing the stator to slowly rotate during the probe traverse. Since the rotor blade passing rate is much higher than the stator blade passing rate, the result is a time resolved measurement of events connected with rotor blade passing, while the radial and circumferential surveys are essentially quasi steady.

Some attempt was made to correlate the stator measurements with the stator inflow and outflow, but this task remains in need of much more work. It is hoped that the documentation of the flow will be sufficiently complete to allow others to carry on with this effort.

CHAPTER 2

APPARATUS and INSTRUMENTATION

The experiments were performed in the M.I.T. Blowdown Compressor Facility. The blowdown facility is described in detail in reference [9]; for future reference it is briefly described here, along with the experimental apparatus unique to the present study.

2.1 The Blowdown Facility

It consists of a compressor test section which is initially separated from a supply tank by an aluminum diaphragm. The test section is followed by a dump tank into which the compressor discharges. The facility is capable of accommodating transonic stages having a tip diameter up to 23.25 inches (Fig. 2-1).

To prepare for a test the system is evacuated. The supply tank is then filled with a mixture of 82% Argon and 18% Freon-12. This mixture has a ratio of specific heat equal to 1.4, but the speed of sound in this mixture is about 75% of that in air, hence the desired Mach numbers can be achieved at lower shaft speeds and lower stress levels. The supply tank is filled to 495 mm Hg. when the M.I.T. compressor stage is to be tested.

The rotor is then brought to speed in vacuum. The test starts by rupture of the diaphragm which allows the gas in the supply tank to flow through the test section. A throttle plate downstream of the test section controls the mass flow through the stage.

During the test time the rotor is driven by its own inertia, hence slowing down as it works on the fluid. The supply tank total pressure and temperature also decrease as a result of expansion of the gas into the dump tank. By correct matching of the rotor inertia and supply tank pressure the Mach number and rotor inlet velocity triangle can be kept constant.

The forward flow duration time is only about 0.2 seconds after which the gas sloshes back and forth until it comes to rest (Fig. 2-2). The first 70 milliseconds of this time period is essential to establish the flow through the test section. The next 40 milliseconds is the quasi-steady period during which the useful data is to be taken. After this period the throttle orifice behind the stage unchokes and the stage rapidly stalls as a result of the increased pressure ratio across the test section. Measurements are made through several instrumentation ports along the length of the test section.

2.2 The M.I.T. Compressor Stage

This compressor stage originally designed by Kerrebrock [9] has a transonic rotor with a tip tangential Mach number of 1.2. The stage has a design pressure ratio of 1.6.

The rotor has 23 blades, an inlet hub to tip diameter ratio of 0.5 and an outlet hub/tip diameter ratio of 0.64 with a tip diameter of 23.25 inches. The relative Mach number at the tip is 1.3 and the inlet axial Mach number is 0.5. The design parameters for the rotor are listed in Table 2-1. The rotor is followed by a stator 3/4" axially spaced.

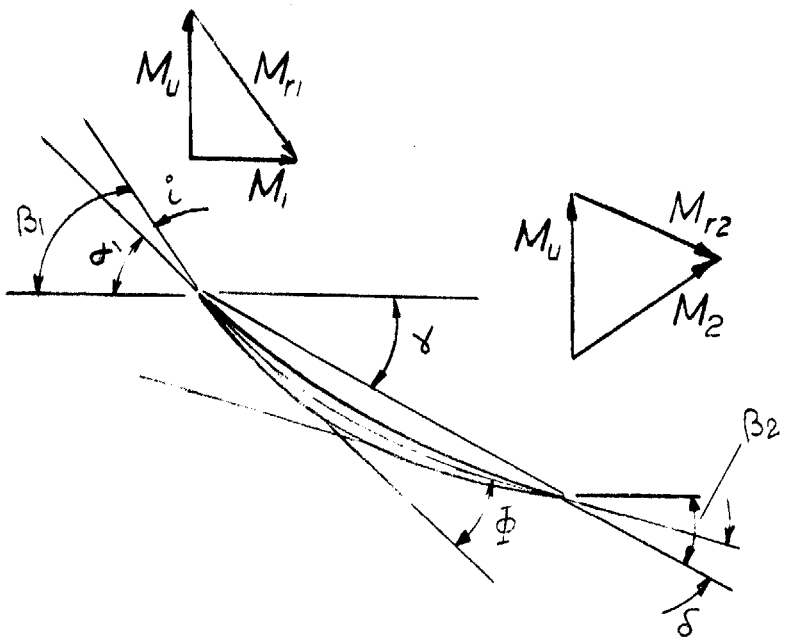

R_1/R_t	0.5	0.6	0.7	0.8	0.9	1.0
R_2/R_t	0.64	0.71	0.78	0.85	0.93	1.0
M_t	0.60	0.72	0.84	0.96	1.08	1.2
M_{r1}	0.78	0.88	0.98	1.07	1.29	1.30
β_1	50.2	55.2	59.2	62.5	65.2	67.4
β_2	23.8	35.7	44.2	50.6	55.6	59.5
σ_r	2.00	1.67	1.43	1.25	1.11	1.00
D_r	0.50	0.49	0.45	0.43	0.40	0.38
i_c	11.5	10.4	9.9	7.7	4.5	1.3
c	22.0	14.7	9.0	7.5	6.7	8.1
α_1	38.7	44.8	49.3	55.0	61.2	66.1
α_2	16.7	30.1	40.3	47.5	54.1	58.0
γ	28.9	38.1	45.0	51.1	56.3	61.7
t/c	0.10	0.086	0.072	0.058	0.044	0.030
M_2	0.68	0.65	0.62	0.60	0.58	0.57

Table 2-1. The Rotor Blade Design Parameters

The stator has 48 blades and an outlet hub/tip diameter ratio of 0.68. The stator blades initially designed by Kerrebrock [9] could not be used in this experiment, since they had radially varying stagger, while the traversing blade is required to have a constant shape from tip to hub and uniform twist so that the stagger angle and cross section can be held constant at each radius during the traverse.

These two requirements led to a design for the stator that does not completely remove the swirl put into the flow by the rotor*. The blades have a total twist of 11.5 degrees from hub to tip (a chord length of 1.9" and a maximum thickness to chord ratio of 0.07). The design parameters for the stator are listed in Table 2-2.

To enable a survey of the flow field behind the stator in the circumferential direction as well as in the radial direction the stator assembly is supported on bearings and is allowed to rotate during the test time. The motion of the stator, at rest before the test, is caused by the torque acting on the stator due to swirl in the flow. The moment of inertia of the stator assembly is chosen large enough to avoid the stator's spinning too fast. The maximum angular velocity of the stator is 2% of the rotor angular velocity. During the traversing blade experiments the stator assembly is locked in position to prevent rotation (Fig. 2-1b), one of the 48 blades being replaced by the traversing blade.

2.3 Traversing Blade Assembly

The traversing blade has the same sectional geometry as the rest of the blades, but is three times longer. At the hub and the tip teflon guides keep the blade at a constant setting angle during the traverse. At

*The optimum design in this case would be to have the mean flow from the stator in the axial direction.

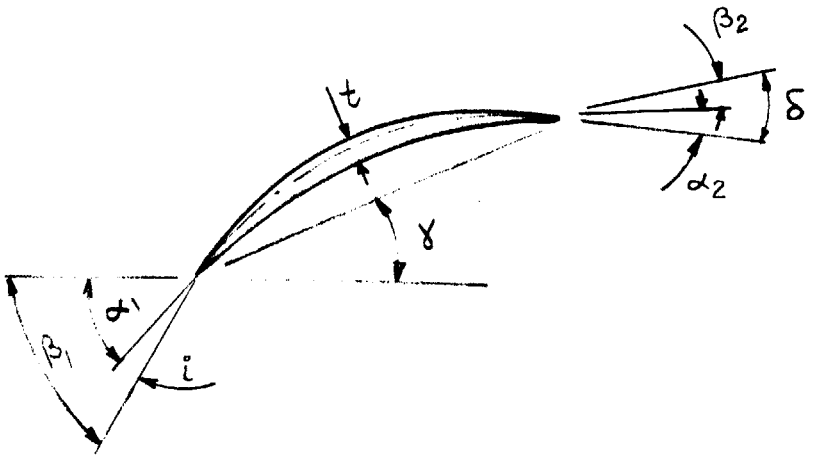

R/R_t	0.68	0.74	0.8	0.86	0.93	1.00
σ_s	1.57	1.41	1.28	1.18	1.08	1.00
D_s	0.55	0.53	0.52	0.52	0.48	0.47
β_1	47.5	44.6	42.0	39.4	37.0	35.0
i	7.23	6.73	6.66	6.28	6.14	5.96
δ	6.54	6.76	6.86	7.07	7.37	7.62
α_1	40.27	37.87	35.34	33.12	30.96	29.04
α_2	2.77	0.37	-2.16	-4.38	-6.64	-8.56
β_2	9.31	7.13	4.7	2.69	0.73	-0.84
ϕ	37.5	37.5	37.5	37.5	37.5	37.5
γ	21.52	19.12	16.54	14.37	12.11	10.29

Table 2-2. Design Parameters for Stator

the ends of the traverse the instrumented location of the blade goes into cavities beneath the teflon guides, providing reference pressures at each boundary at the annulus (Fig. 2-3).

The traversing blade is moved by a pneumatic driver which is designed to move the blade with a nearly constant traverse speed and quick acceleration and deceleration at the two ends. The total traverse time is controlled and can be as short as 25 milliseconds including the start and stop. A typical trace of the blade position versus time is shown in Figure 2-4.

The traversing blade is instrumented at one spanwise position and five chordwise locations on each of the suction and pressure surfaces, the locations on the suction and pressure surfaces being displaced about 0.25" spanwise from each other. The transducers used here are Entran miniature silicon semiconductor transducers installed on Invar rings for stress isolation (Fig. 2-5a). The straingauge transducer itself is a silicon circular diaphragm 0.056" in diameter and 0.001" thick, with a Wheatstone bridge on the back. The transducers have a natural frequency of 150 KHz. and can withstand pressure differences up to 50 psi.

To stress isolate the transducers, they were assembled on Invar rings of 0.125" diameter and 0.025" thick. Each transducers has five leads, four essential to complete the bridge and one for thermal compensation. The complete transducer assemblies were then flush mounted on the blade surface, being isolated from the blade with soft epoxy (Fig. 2-5b). All the transducers have a vacuum line connected to their back for pressure reference.

2.3.1 Orientation of Transducers and Stress Isolation

Although considerable effort was put into stress isolation of the transducers, the attempt was not wholly successful. Low frequency vibration of the blade due to mechanical shocks from large acceleration and deceleration at the two ends of traverse, as well as the D-C loading due to torsion of the blade during the traverse introduce low frequency noise with large amplitude to the pressure signal measured by the transducers.

Careful examination of the signals from all the transducers during a test shows the following characteristics. For the first harmonic of the blade bending vibration (at 250 Hz) which dominates the low frequency disturbance, the phase and the amplitude of the vibrations are sensed differently by different transducers. For transducers which are at the same chordwise location but placed on opposite surface of the blade there is always a phase difference of 180° between the noise signals. But the transducers located on the same side of the blade sense the noise with no phase difference although with different amplitudes. The difference in phase and amplitude of the noise seen by different transducers could not be explained by an argument based on their geometrical location on the blade.

Figure 2-7 shows the shape and the configuration of the bridge elements on the diaphragms. It can be seen that if the diaphragms are strained in x-x direction the resistance of the bridge elements will not be affected. On the other hand the maximum change in the resistance of

the bridge elements will happen when the diaphragms are strained in the y-y direction.

Based on this argument the sensitivity of the transducers to stress in the blade depends on the relative orientation of the x and y axes with the direction of principle strain. For bending mode vibrations of the blade the signals from three different transducers are compared in Fig. 2-8.

This problem could have been avoided by carefully installing the transducers such that x-x axis lies along the blade span. But this problem was identified during the experiment.

Here the problem was dealt with by two means:

1) Since the bending vibration signal was nearly a pure frequency it was removed by a narrow band digital filter.

2) The strain loadings that affect the measurements were determined by covering the transducers to isolate them from pressure variations, then repeating the blowdown tests. The signal so obtained could then be subtracted from the original pressure signal to remove the noise.

2.2.5 Thermal Compensation of Transducers

Since the strain-gauge elements have very little thermal capacity and large temperature coefficients of resistivity, they are very sensitive to temperature changes. This is a problem faced by all users of such high frequency transducers to some degree. For the instrumented blade all the transducers were thermally compensated using resistive compensation circuits.

The resistive compensation does not eliminate the temperature sensitivity completely, but as the transducers on the blade are surrounded by large amounts of metal and are located far enough apart (relative to their size) to prevent heating by the excitation power, the resistive compensation seemed adequate.

2.4 The 5-Way Probe

The time dependent radial and circumferential distribution of Mach numbers and flow angles as well as total and static pressure were determined using a spherical probe [10].

The probe consists of a nearly spherical head on which transducers of the type described in 2.3 are mounted (Fig. 2-9). One transducer in the center is surrounded by four others so located that the surface of each is at a 45° angle from the next one. The heat transfer characteristics of the sphere in high Mach number flows make the thermal drift problem more severe for the probe than for the stator blade. In this case the resistive compensation did not suffice. To overcome the thermal drift problem the current through a branch of the bridge was recorded too. This signal is a measure of thermal drift because the current through the bridge does not change due to pressure changes. By correct scaling this signal can be subtracted from the pressure signal to correct for thermal drift (Fig. 2-10).

The probe is traversed across the annulus using a pneumatic driver. The total traverse time can be as little as 25 milliseconds. The traverse ports are numbered 1 through 7 in Fig. 2-1b.

2.5 Other Time Dependent Measurements

The flow quantities in the facility which have a time constant of variation on the order of one millisecond are referred to as low speed quantities. Such quantities are wall static pressure at different locations of the test section and the supply and the dump tank stagnation pressures. These pressures are measured using pressure transducers which have a lower natural frequency and are more stable.

The high frequency pressure at the casing, such as gapwise pressure distribution or the pressure at the leading edge of the rotor, are measured using high frequency pressure transducers of a similar type to the one described in Section 2.3. The rotor angular position was also monitored electronically and recorded during the test time.

2.6 Data Storage Layout

The signal from the blade or probe transducers and also the low frequency data were first amplified. The amplified signal was then recorded two ways:

a) digital storage, using an analog to digital converter (A/D) having six high speed channels, each capable of sampling data at a rate of 100,000 points per second. The digitized data was then transmitted to a computer and stored on the disc.

b) analog temporary storage, in which a 14-channel high speed FM tape recorder was used. The tape recorder can record data with a tape speed up to 120 inches per second. The tape recorder was used because the A/D did not have the capacity to accept all of the data during the test time. After the test the

tape recorder was played back at 120 inches per second to the analog to digital convertor. This way the rest of the data channels were digitized and sent to the computer to be stored on the disc. All the data was backed up onto digital magnetic tape for permanent storage (Fig. 2-11).

CHAPTER 3

DATA ANALYSIS

As mentioned before the data taken during each test was stored on computer disc and digital magnetic tapes. The unique opportunity presented by the Gas Turbine Laboratory computer facility for data acquisition and reduction made it possible to analyze the data in a very accurate and efficient manner.

To be able to study rotor wake related phenomena in the compressor, the data sampling frequency had to be much higher than the rotor blade passing frequency. During the test time the analog signals from high frequency transducers are sampled at a rate of 100 KHz. by the analog to digital convertor. For each test over 150,000 data points were recorded.

The analysis of the data can be divided into two parts, probe data analysis and the analysis of the data from the traversing blade. In the following the steps involved in the analysis of each set of data are described in some detail.

3.1 Probe Data Analysis

The results of the calibration of a 5-way probe model in a two-inch diameter free jet were used to reduce the probe data. The model probe was geometrically similar to the actual probe and was twice as large. Pressure taps were located on the model probe at the same locations as the high frequency transducers on the probe.

For several values of flow Mach number and different values of ϕ and θ angles (see Fig. 2-9) the pressures at the five points on the probe were recorded. The following nondimensional parameters were then retrieved from the calibration measurements and plotted versus ϕ and θ:

$$KP_i = \frac{P_i - P_s}{(P_3-P_1) + (P_2-P_1)} = f(\phi,\theta,M) \qquad i = 2,3 \tag{3.1}$$

$$F_{45} = \frac{P_4 - P_5}{(P_4-P_1) + (P_5-P_1)} = g(\phi,M) \tag{3.2}$$

$$F_{23} = \frac{P_2 - P_3}{(P_3-P_1) + (P_2-P_1)} = h(\phi,\theta,M) \tag{3.3}$$

$$C_{P1} = \frac{P_1 - P_s}{P_t - P_s} = j(\phi,\theta,M) \tag{3.4}$$

$$H = \frac{P_t - P_s}{(P_3-P_1) + (P_2-P_1)} = k(\phi,\theta,M) \tag{3.5}$$

$$P_t = P_s\left(1 + \frac{\gamma-1}{2} M^2\right)^{\gamma/\gamma-1} \tag{3.6}$$

The functions on the right hand-side of Eq. (3.1) to (3.5) are the calibration functions which depend on pitchwise and radial angles and Mach number. Having these calibration functions, the above set of

equations could be solved for each data point to calculate total and static pressures and flow angles. A computer program was written that numerically solves the above set of equations for each data point.

Note that according to Eqs. (3.1) to (3.5) five known pressures, P_1 to P_5, are used to find four unknown parameters (total and static pressures and flow angles). This says that there is a redundancy in the analysis. Ideally these equations should form a consistent system of equations that enables us to use the redundant piece of information to check the calculations. But actually the information from transducer P_5 (transducer next to the stem of the probe) was not used in this analysis, for it results in unrealistically high negative radial flow angles. This is partly due to the geometrical differences between the stems of the actual and the calibrated probes. Also the thermal drift characteristic of transducer P_5 is different from the other four, hence the compensation scheme used for other transducers is inadequate for P_5. To overcome this difficulty a local pressure coefficient for transducer P_4 was used instead of F_{45} (Eq. (3.2)), defined as follows:

$$C_{P4} = \frac{P_4 - P_s}{P_t - P_s} = \ell(\phi, M) \tag{3.7}$$

Using C_{P4} requires a higher number of iteration steps, because the solution requires an initial prediction for three of the parameters used in the equations (P_t, P_s, M).

The calculated flow parameters for measurements between rotor and stator and behind the stator at different axial and radial positions are shown in Figs. 4-1 to 4-33.

3.2 Traversing Blade Data Analysis

It was pointed out in Chapter 2 that the transducers mounted on the blade were strain sensitive and that the data from the blade was disturbed by low frequency noise and some D-C offset. The output signals from the transducers on the blade are the result of the following effects:

i) actual static pressure at the point,

ii) strain due to twist of the blade during the traverse and aerodynamic loadings on the blade;

iii) strain due to large radial forces during acceleration and deceleration at the two ends of the traverse; and finally

iv) strains due to mechanical vibration.

From all these only the first, the static pressure, is of interest here and all the others are assumed to be disturbances to be separated from the signal. The traversing blade data was used to study phenomena related to rotor blade wakes and also to determine the steady state loadings on the stator blades. The separation of the disturbances from the desired pressure signal was done in different ways for the steady and unsteady pressures.

3.2.1 High Frequency Studies

For the study of the high frequency part of the pressure signals the data was filtered using a digital filter. Fortunately the

vibratory noise in the data had a frequency (250 Hz.) much lower than blade passing frequency (3500 Hz). Therefore use of a digital filter with sharp enough band pass (50 Hz max.) guarantees that the information contained in the frequency range of interest is well preserved. This digital filter played a very important role in the analysis of the blade data, therefore it deserves a few words. The computer program of this filter was written on the basis of the logic presented in [11]. The related subprograms presented in Ref. [11] were modified to give the program the capability of filtering frequencies as low as .00025 of the sampling frequency. The filter could have up to 2000 terms. The result of band-pass filtering (edges at 50 and 1000 Hz.) performed on a typical signal from one of the transducers on the blade is shown in Fig. 3-1. Filtering at this frequency range does not introduce a loss of power in lower or higher dominant frequencies. The results of spectral analysis of the signal before and after filtering are shown in Fig. 3-2.

For high frequency studies the data was high pass filtered at 2000 Hz. and then run through a chain of programs to calculate: frequency content of the unsteady pressure distribution on the stator blade, axial and tangential forces and pitching moment on the blade due to wakes, and frequency content of the forces acting on the blade. The results of the above calculations are shown in Fig. 4-34 through Fig. 4-48.

3.2.2 Steady State Studies

The steady part of the pressure measurement can not be separated from the noisy signal by filtering only. To achieve a separation the transducers on the blade were covered with small aluminum caps

to completely isolate them from pressure inputs. The instrumented blade was then put back into the facility and the same traversing blade tests were repeated. These tests clearly yields the measurement of loading and vibratory stress signals.

The D-C pressure distribution was then found as follows: the loading signal was subtracted from the original signal and the result was then low pass filtered at 100 Hz. Figure 4-49 shows the chordwise pressure distributions on the stator blades at three radii. The radial distribution of steady state axial and tangential forces on the stator blade are shown in Fig. 4-50.

CHAPTER 4

RESULTS

4.1 Rotor Overall Performance

The overall performance of the rotor is calculated from both the probe measurements and wall static measurements. The calculations show that the rotor has an average total pressure ratio of 1.66, changing from 1.71 at the tip to 1.6 at the hub (Fig. 4-1b), and an average total-to-total isentropic efficiency of 0.80 (see Appendix A), changing from 0.58 at the tip to 0.90 at the hub (Fig. 4-1d). In calculating the time-resolved efficiency Euler's equation was used to find total temperature ratio across the rotor. These calculated efficiencies may not be directly comparable to values determined by conventional steady state methods of stagnation temperature and pressure measurement. They should be comparable for the portion of the flow which has not undergone extensive viscous interaction, but not necessarily for the wakes. This point requires further examination. A corrected mass flow rate of 115 lbm/sec was also measured (mass flow is corrected to standard sea level conditions). The mass flow through the stage has been calculated by four different methods. These methods (see Appendix B) and the corresponding calculated values are as follows:

i) from the measured rate of pressure drop in the supply tank (114.5 lbm/sec);

ii) from the measured static pressure downstream of the stage before the choke plate (116 lbm/sec);

iii) from the rotor inlet Mach number which is computed from the static pressure upstream of the rotor (109.7 lbm/sec); and,

iv) from the integration of the flow quantities measured by the probe along the radius (104.5 lbm/sec).

The results of the first two methods agree within 2%. The mass flow calculated by method iii is 5% lower than the first two methods. Comparison of the results of pressure measurement on the casing using a high frequency transducer with those from a low frequency transducer which was originally used to measure static pressure upstream of the rotor, showed that the latter measures a pressure higher than the actual temporal mean wall static pressure. Although the low frequency transducer was located two rotor chords upstream of the rotor, it appears that it was influenced by the upstream shocks from the rotor. The measurement by the low frequency transducer located 1 rotor chord upstream of the rotor was 20% higher than the weighted average of the pressure measured by a high frequency transducer at the same location. Although the mechanism leading to this error has not been determined this indicates that low frequency response pressure transducers with conventional pressure tappings may give unreliable results upstream of transonic rotors where strong shocks exist.

Method iv gives a mass flow much lower than the other three methods. This is partly due to excluding the boundary layer regions at the hub and the tip in integration and in part due to the error in the D-C level of the flow quantities measured by the probe.

4.2 Stage Overall Performance

The stage has an average total pressure ratio of 1.57 and an average efficiency of 70% (radially averaging the circumferentially averaged flow behind the stator). A stage pressure ratio of 1.6 and an efficiency of 73% result from radially averaging the time averaged total pressure measured downstream of the stator at the middle of the stator passage. These stage efficiencies are calculated by assuming constant total temperature across the stator and finding the stage total temperature rise from Euler's equation. Consequently the results are very sensitive to the level of the measured total pressures behind the stator. Clearly the overall performance of the stage should not be judged on the basis of these values. However the changes in these efficiencies across the wakes in every axial position can be used to estimate the losses. This suggests an average 2.5% decrement in total pressure and 3% decrement in efficiency due to stator wakes. Most of these losses come from the stator hub region. The causes of these losses are discussed later.

The torque acting on the rotor and stator should balance with the changes in the fluid's angular momentum. The torque acting on the rotor calculated from the rate at which the rotor slows down as it works on the fluid during the test time is 850 lbf·ft (normalized to atmospheric conditions in the supply tank) and from the change in the angular momentum across the rotor the torque is calculated to be 1116 lbf·ft. The large difference between the two numbers is due to insufficient resolution in the measurement of the rotor speed which results in an incorrect calculation of rotor deceleration. The dynamic coupling between the rotor

and the drive motor, and the flexibility of the interconnecting shaft and couplings plus the oscillations in the supply tank pressure make the rotor speed oscillate with a frequency higher than the shaft rotational frequency. These oscillations cause up to 25% changes in rotor deceleration, which cannot be detected if the rotor speed is measured with a one pulse-per-revolution tachometer, as was done here.

The stator torque was calculated by three different methods and the results agree within the experimental accuracy. Dynamic calculation using stator acceleration gives 750 lbf.ft (normalized for atmospheric conditions in the supply tank), the fluid angular momentum balance gives 800 lbf.ft and integration of the pressure over the blade surface using the traversing blade data gives 850 lbf.ft torque for the stator. This agreement provides an important consistency check on the stator pressure data.

4.3 Flow Field Behind the Rotor

The analyzed probe data behind the rotor are shown in Figs. 4-3 to 4-9, in which the rotor outlet flow angles and Mach numbers as well as total and static pressure ratio, local efficiency and rotor outlet relative Mach number are plotted versus blade passing periods for three different radius ratios. In each of Figs. 4-3 to 4-9 the ensemble average over 3 blade passages is presented at the right.

The data presented in Figs. 4-3 to 4-9 show that there is a large tangential and radial flow angle variation associated with the wakes, sometimes up to 25° or more. The radial flow angle is large and positive near the suction side, drops down across the passage and reaches a negative

value on the pressure side. This says that there is a radial shear in the wake, shedding streamwise vorticity downstream. There are significant total and static pressure fluctuations in the wakes and the flow Mach number changes as much as 30% across the wake (Figs. 4-6, 4-7). The local efficiency is near 100% in the "inviscid" flow between the wakes near the hub and drops down in wakes (Fig. 4-8). Near the tip the efficiency is low also in the flow between wakes, apparently due to shock pressure losses.

The significance of the ensemble averages is that the most periodic part of the signal will be emphasized, since the blade-to-blade variations are suppressed. Comparison of the ensemble averages to the true time dependent signals shows there are large blade-to-blade variations, particularly in the pressure ratios.

Comparison between the data from different radii shows that near the hub there is a much larger velocity defect in the wakes, a higher pitchwise flow angle variation and a larger axial Mach number defect, than at other radii. The axial Mach number in the wake reduces to 50% of its mean value near the hub.

Close to the tip, there is a large degree of variation between the wakes from different blades and the wakes are not nearly as strong as they are at other radii.

Figure 4-9 compares the rotor outlet relative Mach number for three different radii. It shows that the relative flow Mach number is nearly constant across the passage and drops down in the wakes.

The results presented in Figs. 4-3 to 4-9 show that the outlet flow from the rotor is very unsteady, highly three dimensional and the wakes from the rotor are very different from the two dimensional models adopted in theoretical studies.

4.4 Flow Behind the Stator

The results of probe data analysis behind the stator are shown in Fig. 4-10 through Fig. 4-30, for different axial and radial positions. Figures 4-10 to 4-18 correspond to measurements at a plane which is only 0.1 rotor chord downstream of the stator. In each figure the data from the circumferential survey of the probe over the outlet of a full stator passage plus the wakes of the two bounding blades are shown. The data in the mid-passage shows the time history of the rotor wakes as they are convected through the stator passage and the two stator wakes on the sides of the figures show the stator wake structure under the influence of rotor wakes (consult Fig. 4-10 on the top).

For some of the flow quantities such as radial and tangential flow angles and Mach number the data reduction program is incorrect when the probe is aligned with the stator trailing edge, due to insufficient spatial resolution of the probe in this region. The "spikes" in these regions should therefore be ignored.

The following results can be observed in reference to Figs. 4-10 to 4-18. The stator wakes are deeper and stronger at the tip than they are at the hub. This is mainly due to the large mean angle of incidence at the inlet to the stator near the tip region. According to the tangential angle plots the flow is turned more by the suction side than by the pressure

side, and there is a large total pressure drop in the stator wakes, whereas static pressure is nearly constant in the stator wakes.

One interesting point is that the rotor wakes still exist nearly undiminished in the flow downstream of the stator. In fact the radial and tangential flow angles in the stator "inviscid" flow change as much as 20° due to the rotor wakes (Figs. 4-10, 4-13, 4-16), and there are significant total and static pressure fluctuations in the flow downstream of the stator as a result of the rotor wakes. Comparison of the results for different radii shows that unsteadiness related to the rotor wakes appears more regularly in the tip region, while close to the hub some of the wakes seem to have been filled up.

Similar sets of data from measurement at one and two rotor chord lengths behind the stator are shown in Figs. 4-19 to 4-27 and 4-28 to 4-30. The rise in Mach number levels and the static pressure drop in the set of data presented in Figs. 4-28 to 4-30 are due to the fact that the corresponding measurement port is close to the throttle orifice and the flow acceleration towards the orifice opening shows in the data. Nevertheless the unsteady part of the data at mid-span (the data shown in Figs. 4-28 to 4-30) can be used for comparison.

Comparison between these three sets of data for the three axial positions behind the stator and the data taken between rotor and stator gives the following results: the rotor wakes appear nearly undiminished in the exit of the stator relative to the rotor exit whereas they are seen to decay at a more rapid rate in the annular duct behind the stator

(see Figs. 4-31 and 4-32). The stator wakes decay very rapidly so that at a distance of one rotor chord behind the stator they have virtually ceased to exist.

4.5 Traversing Blade Results

Figures 4-34 to 4-39 show the unsteady pressures measured on the stator blade at different radii. On each figure the curves are from top to bottom the measurements at 20, 35, 50, 65 and 80 percent of the chord for both the suction and the pressure surfaces of the stator blade. In part "b" of each figure the power spectra of the pressure signals are plotted. These figures show that the pressure on the surface of the stator blade changes periodically with a dominant frequency equal to rotor blade passing frequency.

The probe data shown in Figs. 4-3 to 4-9 at different radii are so chosen in time as to correspond to the flow properties at the leading edge of the stator for the periods at which the unsteady traversing blade data are analyzed at corresponding radial positions. (Note these two sets of data come from two different tests.)

An immediate result of the comparison among the pressure traces (Figs. 4-34 to 4-39) is that they are very nearly in phase, but this phase relationship does not support the simple convective models of wake behavior in stator in which on blade pressure fluctuations are associated with the local wake induced velocity fluctuations. In reference to Figs. 4-3 to 4-9 (which show the flow properties at the stator leading edge), it can be seen that as the angle of incidence to the blade is changed due to the rotor wakes, the pressure at all the points on the

blade changes almost immediately. These observations lead to the conclusion that the chord-wise pressure distribution on the stator blades is determined by the change in circulation around the blade as a result of the change in angle of incidence, the local velocity fluctuations within the stator passage having a lower order effect on the unsteady chordwise pressure distribution.

These results are in qualitative agreement with previous work on isolated airfoils and cascades. Based on Sears' calculation [1,2] for incompressible flow over an isolated airfoil, the pressure at all points over the chord changes in phase in response to the gust. Moreover the experimental observations of Commerford and Carta [13] showed that for an isolated airfoil in a compressible flow there is no phase difference between the pressure fluctuations on the pressure surface, and that there is a scattering in the phase for the suction surface.

A large scattering in the phase angle of the pressure fluctuations over the chord can also be observed in the experimental results of Fleeter, Jay and Bennet [7]. However the phase angles for most points over the chord seem to be nearly equal for their 100% corrected speed operation data, a point which seems to have been ignored by the authors.

Furthermore the time marching calculations of Mitchell [16] also showed that the unsteady pressure distribution over a blade in a cascade does not depend on the local fluctuations within the passage, which agrees with what we have found.

The unsteady data from the traversing blade can be presented in forms that are more descriptive as far as the loadings on the stator are

concerned. Figure 4-40 to Fig. 4-42 show the instantaneous pressure distribution over the chord of the blade for 30 time intervals during one rotor blade passing period, for three different radius ratios. In part "d" of each of these figures the absolute radial and tangential flow angles and total Mach number of the flow at the leading edge of the blade are plotted for one blade passing period. The values of the angles and Mach number are also written on the top of each pressure distribution plot. The distribution of the unsteady lift coefficient (normalized pressure difference across the blade) over the chord is shown in similar fashion in Figs. 4-43 to 4-35. Finally the unsteady tangential and axial forces and pitching moment acting on the stator blades are plotted versus rotor blade passing periods for three different radius ratios in Figs. 4-46 to 4-48. Next to each loading plot its spectral density is also plotted. Comparison of the plots in Figs. 4-40 to 4-45 gives an animated picture of what happens to the pressure distribution around the stator blade as the wakes go by. For all the radii the introduction of the wake to the leading edge of the stator is associated with a large negative tangential force on the blade which is mostly acting on the middle and rear part of the blade.

Comparison between the data presented in Figs. 4-3 to 4-9 with the unsteady force plots (Figs. 4-46 to 4-48) shows that the wave form of the tangential force very much follows the shape of the incoming gust, and the dominant frequencies in both cases are the rotor blade passing frequency and its harmonics. As mentioned earlier a positive incidence as a result of wake passage seems to result in a negative

tangential force on the stator blade. To find the exact phase relationship between the corresponding frequency components of the force and the gust they were both decomposed into their Fourier components at blade passing frequency and its harmonics. It turns out that the phase between the components of force and the components of the gust referred to the stator leading edge is a constant at each radius and equal to 90° for the hub region and about 180° for other radii.

Arnoldi [12] showed that the phase angle between the gust and the induced lift calculated from Sears' function becomes a constant (equal to 45°) for reduced frequencies higher than 2, if the gust is to be referred to the leading edge instead of the mid chord of the airfoil.

The reduced frequency based on rotor blade passing frequency* "Ω" is equal to 3.58. Although the compressible reduced frequency parameter $K = \Omega M/(1-M^2)^{1/2}$ for the fundamental harmonic is about 3 which is well above the incompressible limit, it seems that our results are in qualitative agreement with the result for isolated airfoils in incompressible flow. Actually the effect of inter blade phase angle becomes less as the reduced frequency goes above 2 [12], which says for high reduced frequencies the blades in a cascade will behave like isolated airfoils.

---

*Reduced frequency Ω is defined as $\Omega = \frac{c\omega}{2v}$ where c is the stator chord length, ω is the rotor blade passing frequency in radians and v is the mean stator inlet flow velocity.

The radial variation of the measured phase angle between the force and the gust (90° for the hub region and 180° for other radii) is most likely due to the variation in the mean angle of incidence to the stator blade. It was shown by Commerford and Carta [13] that as the mean angle of incidence to an isolated airfoil is increased the phase between the gust and the induced lift differs more from the value predicted by the Sears' function.

In Fig. 4-50 the steady state tangential and axial force variation with radius are shown. Figure 4-49 shows the steady pressure distribution and lift coefficient versus chord length for different radii. Comparing Fig. 4-46 to 4-48 with Fig. 4-50 shows that the amplitude of the unsteady tangential force on the blade is as high as 25% of its steady state value, and for axial force this figure is 15%.

The frequency content of the unsteady load on the stator blade is of great importance to the designer. According to Figs. 4-46 to 4-48 the axial and tangential forces on the blade oscillate with rotor blade passing frequency near the hub and at rotor blade passing frequency and its second harmonic at other radii. However the pitching moment oscillates at rotor blade passing frequency and its fourth harmonic near the tip and at blade passing frequency and its second harmonic at other radii.

CHAPTER 5

CONCLUSIONS

1. A time and space resolved survey of the flow downstream of a transonic rotor shows that the rotor wakes have:

   i) large pitchwise flow angle variations, up to 25°,

   ii) large radial outflows with a radial angle up to 30°,

   iii) significant total and static pressure gradients,

   iv) significant Mach number variation, and

   v) large degree of variation from tip to hub and from blade to blade.

Therefore they have a highly three dimensional structure and are very different from two dimensional models.

2. Ensemble averaging of blade-to-blade measurements suppresses the blade-to-blade variation, especially for the pressure measurements, and may lead to a distorted view of the rotor stator interaction.

3. Time and space resolved measurements of flow behind a row of stator blades downstream of the transonic compressor rotor show that:

   i) under the influence of the rotor outflow, the wakes from the stator are deeper and stronger near the tip than they are near the hub;

   ii) there is a significant total pressure defect and practically no static pressure variation associated with stator wakes;

iii) the wakes from the rotor exist nearly un diminished in the exit flow from the stator but the decay in the annular duct behind the stator;

iv) unsteadiness related to rotor wakes appears more frequently in the tip region.

4. Analysis of time resolved measurements of the stator blade surface pressure from tip to hub lead to the following conclusions:

i) the pressure distribution over the stator blade is nearly periodic with a frequency equal to rotor blade's passing frequency;

ii) the pressure fluctuations are nearly in phase at all points along the chord, the chordwise unsteady pressure distributions being determined by the changes in the angle of incidence and not by the local velocity fluctuations within the stator passage.

iii) there are large rotor wake induced, unsteady forces on the stator blades, as high as 25% of the steady forces for the configuration investigated.

iv) the unsteady axial and tangential forces on the stator blades fluctuate with rotor blade passing frequency in the tip region, and with rotor blade passing frequency and its second harmonic at other radii;

v) there seems to be a scattering in phase and magnitude of the forces on the blade relative to those of the rotor wakes, that cannot be predicted by existing two-dimensional models.

5. The data presented here form a basis for development of models for rotor stator interaction which more accurately represent the actual wake structure in transonic compressor stages.

REFERENCES

[1] N.H. Kemp and W.R. Sears, "Aerodynamic Interference Between Moving Blade Rows", J. of Aeronautical Sc., Vol. 20, No. 9, Sept. 1953.

[2] N.H. Kemp and W.R. Sears, "The Unsteady Forces Due to Viscous Wakes in Turbomachines", J. of Aeronautical Sc., Jul. 1955, pp. 478.

[3] J.L. Kerrebrock and A.A. Mikoljczak, "Intra Stator Transport of Rotor Wakes and Its Effect on Compressor Performance", J. of Eng. for Power, No. 70-GT-39, 1970.

[4] J.H. Horlock, "Fluctuating Lift Forces on Airfoils Moving Through Transverse and Chordwise Gusts", J. of Basic Eng., Vol. 90, 1968, p. 494/500.

[5] H.E. Gallus, "Results of Measurement of the Unsteady Flow in Axial Subsonic and Supersonic Compressor Stages", AGARD-CP-177.

[6] H.E. Gallus, W. Kummel, J.F. Lambertz and T. Wallmann, "Measurement of the Rotor-Stator-Interaction in a Subsonic Axial Flow Compressor Stage", R.F.M., Symposium in Aeroelasticity in Turbomachines, Oct. 1976, p. 169.

[7] S. Fleeter, R.L. Jay and W.A. Bennet, "Rotor Generated Unsteady Aerodynamic Response of a Compressor Stator", J. of Eng. for Power, 78-GT-112, 1978.

[8] W.T. Thompkins, Jr., "An Experimental and Computational Study of the Flow in a Transonic Compressor Rotor", M.I.T. G.T.L. Report No. 129, 1976.

[9] J.L. Kerrebrock, "The M.I.T. Blowdown Compressor Facility", M.I.T. GTL Report No. 108, 1970.

[10] W.A. Figeiredo, "Spherical Pressure Probe for Retrieving Freestream Pressure and Directional Data", GTL Report No. 137, Aug. 1977.

[11] J.F. Kaiser and W.A. Reed, "Data Smoothing Using Low-Pass Digital Filters", Rev. Sci. Instrum., Vol. 48, No. 11, Nov. 1977.

[12] R.A. Arnoldi, "Unsteady Airfoil Response", NASA SP-207, pp. 247-256.

[13] G.L. Commerford and F.O. Carta, "Unsteady Aerodynamic Response of a Two-dimensional Airfoil at High Reduced Frequency", AIAA Journal, Vol. 12, No. 1, Jan. 1974, pp. 43-48.

[14] J.J. Adamczyk and R.S. Brand, "Scattering of Sound by an Airfoil of Finite Span in a Compressible Stream", J. of Sound and Vibration, Vol. 25, 1972, pp. 139-156.

[15] D.W. Holmes, "Experimental Pressure Distribution on Airfoils in Transverse and Streamwise Gusts", Cambridge University Publication CUED/A-Turbo/TR 21(1970).

[16] N.A. Mitchell, "Non-Axisymmetric Flow through Axial Turbomachines", Ph.D. Thesis, St. John's College, Cambridge University, England, 1979.

[17] R. Mani, "Compressibility Effects in the Kemp-Sears Problem", NASA SP-304, Part II, 1974, pp. 513-533.

[18] S. Fleeter, "Fluctuating Lift and Moment Coefficient for Cascaded Airfoils in a Nonuniform Compressible Flow", AIAA J. of Aircraft, Vol. 10, No. 2, Feb. 1973.

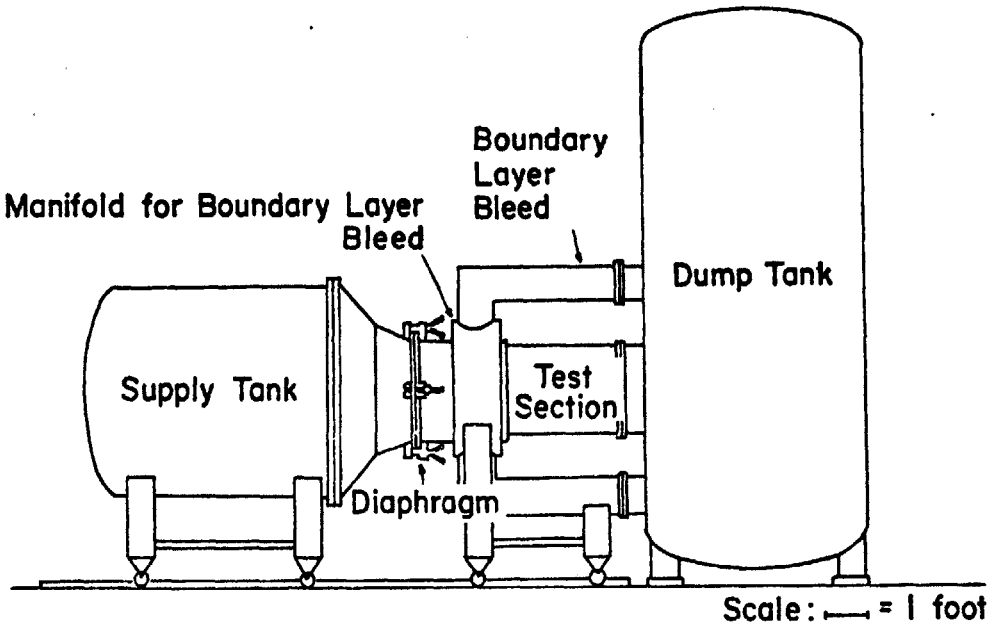

FIG. 2-1a View of the M.I.T. Blowdown
Compressor Facility

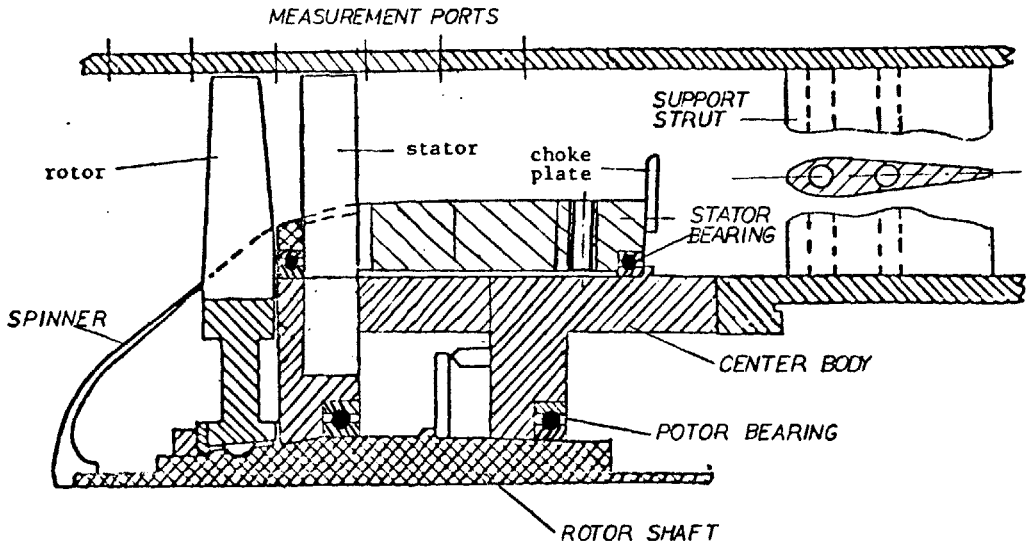

FIG. 2-1b Sectional View of the Test Section
(Stator Free to Move)

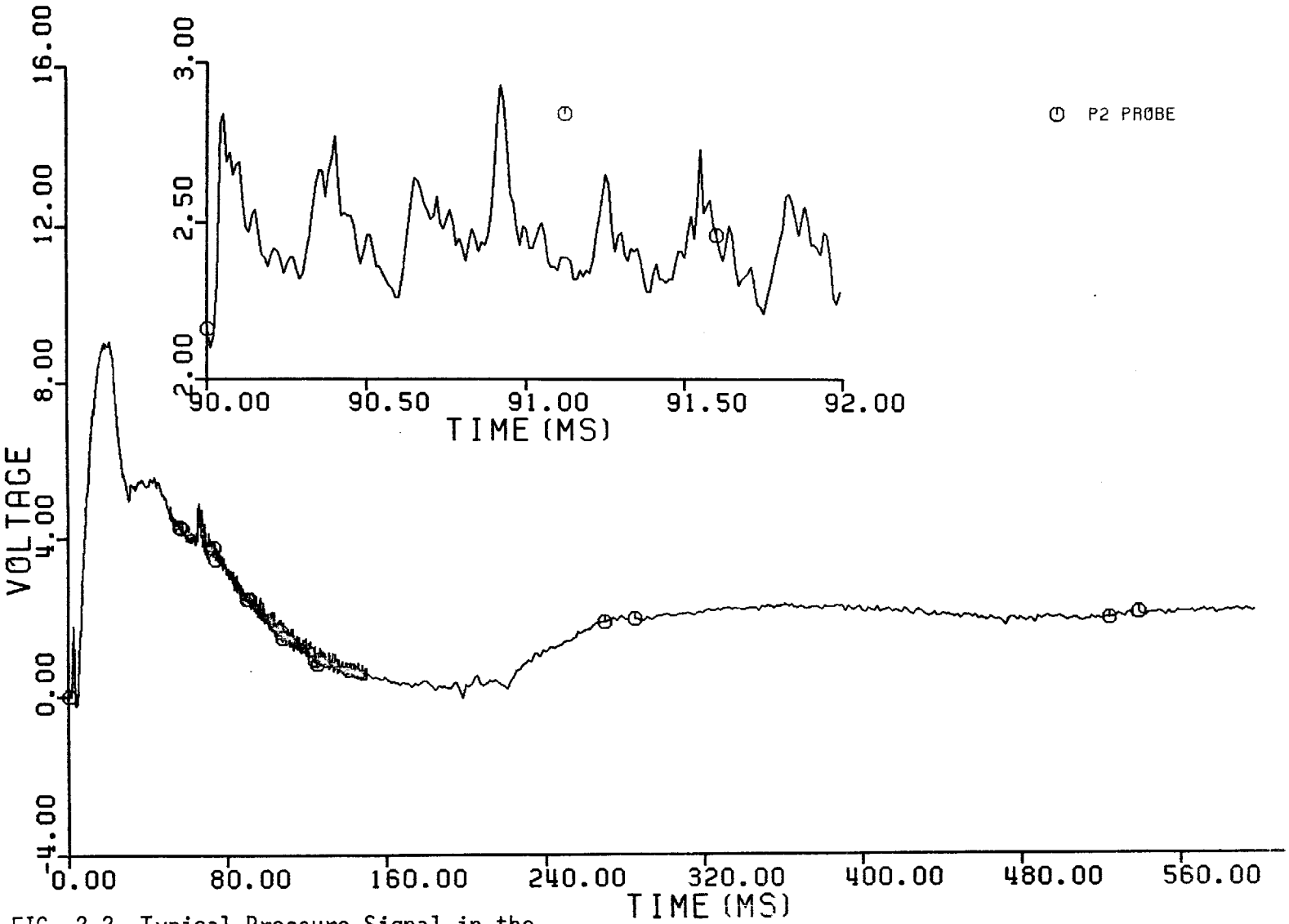

FIG. 2-2 Typical Pressure Signal in the Blowdown Tunnel During the Experiment

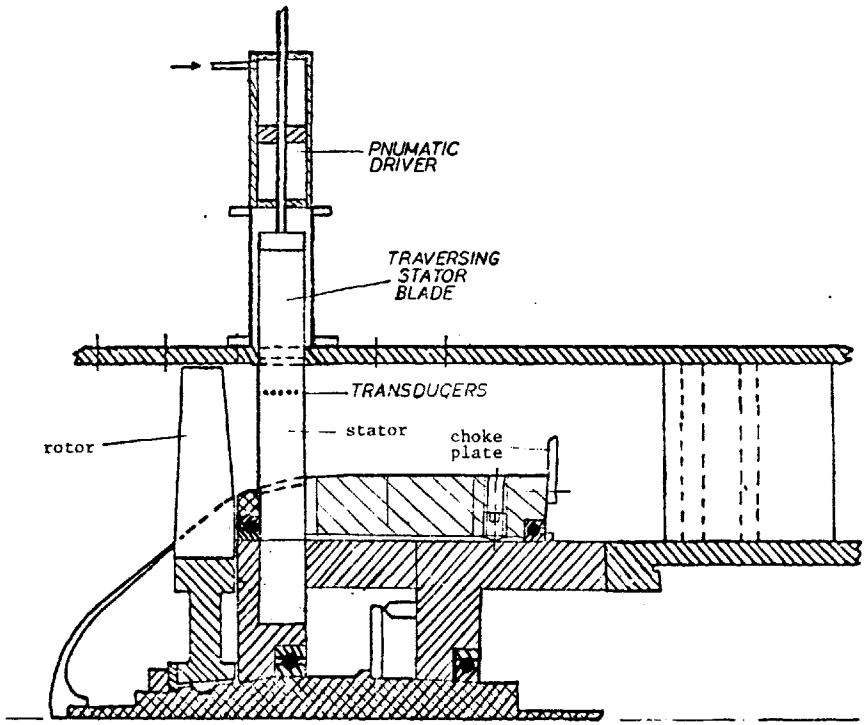

FIG. 2-3 Sectional View of the Test Section with Traversing Blade Installed

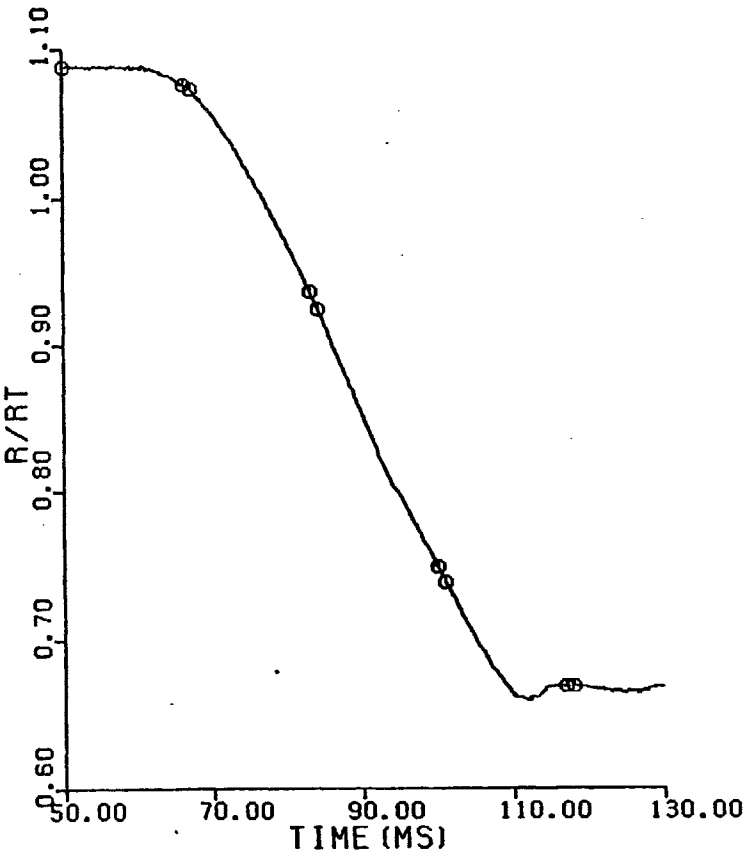

FIG. 2-4 Blade Position v.s. Time During the Traverse

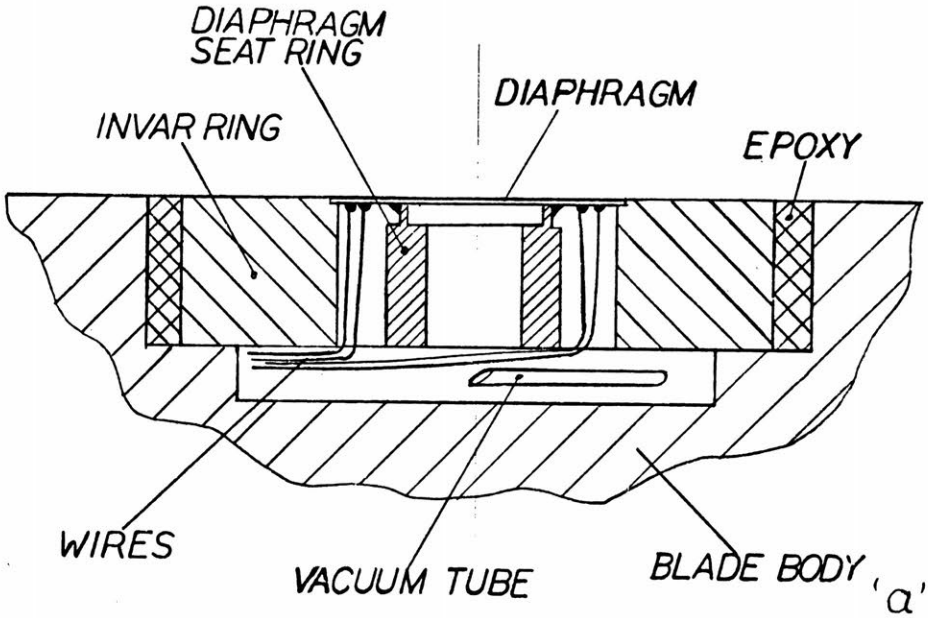

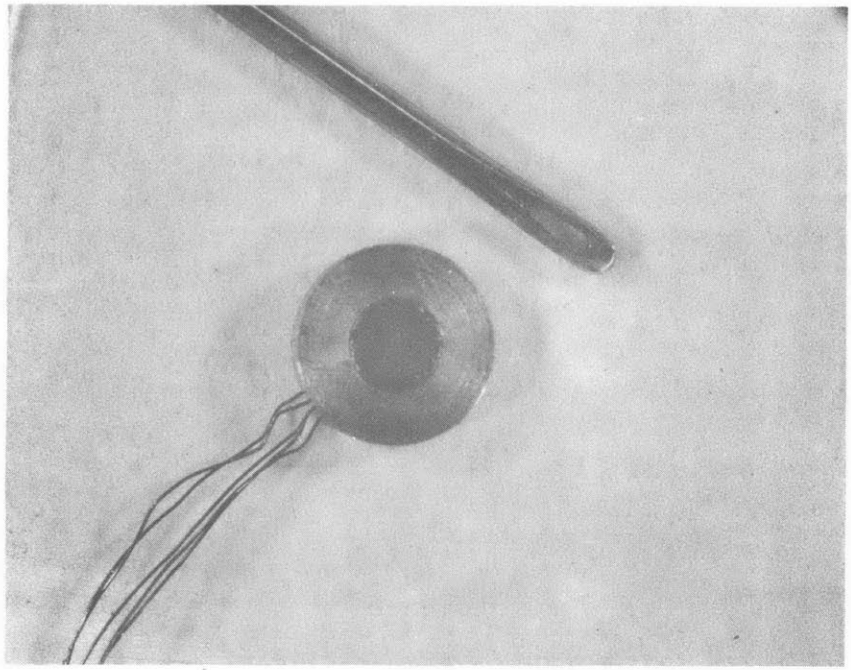

'b'

FIG. 2-5 Miniature Pressure Transducer Assembly; a. Sectional View ; b. Completed Unit

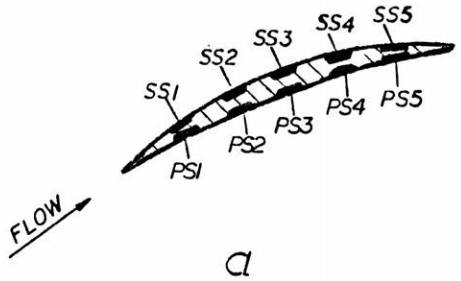

a

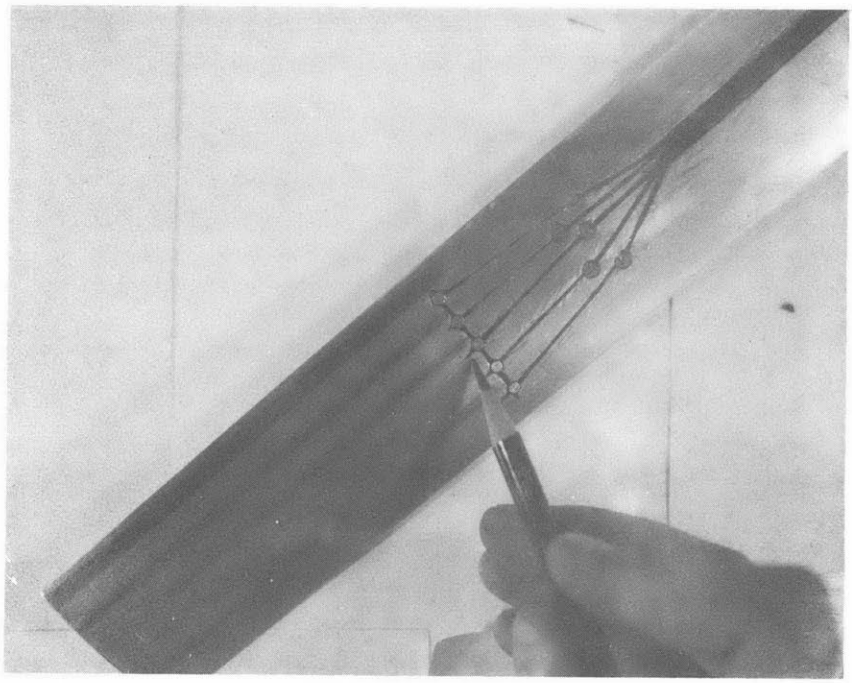

b

FIG. 2-6 Instrumented Traversing Blade; a. Blade Cross-section at Instrumented radii; b. Suction Surface

(transducers covered)

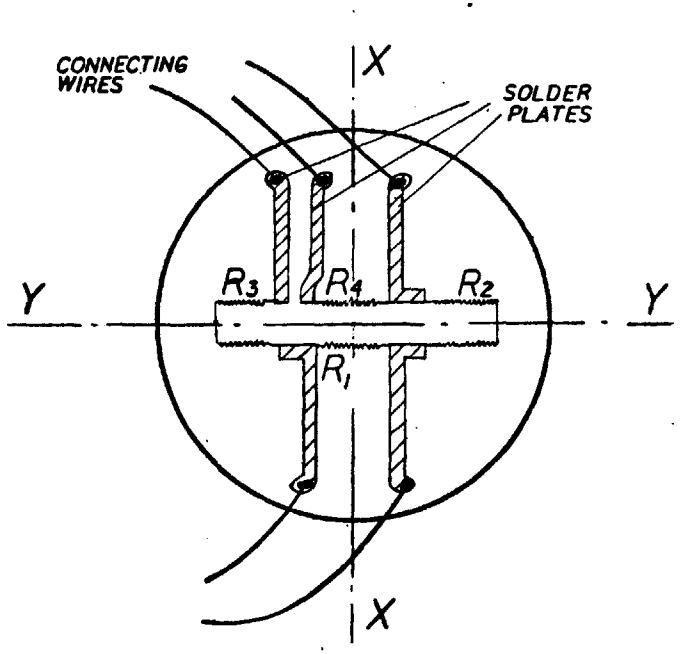

FIG. 2-7 The Configuration of the Bridge Elements on the Transducer's diaphragm

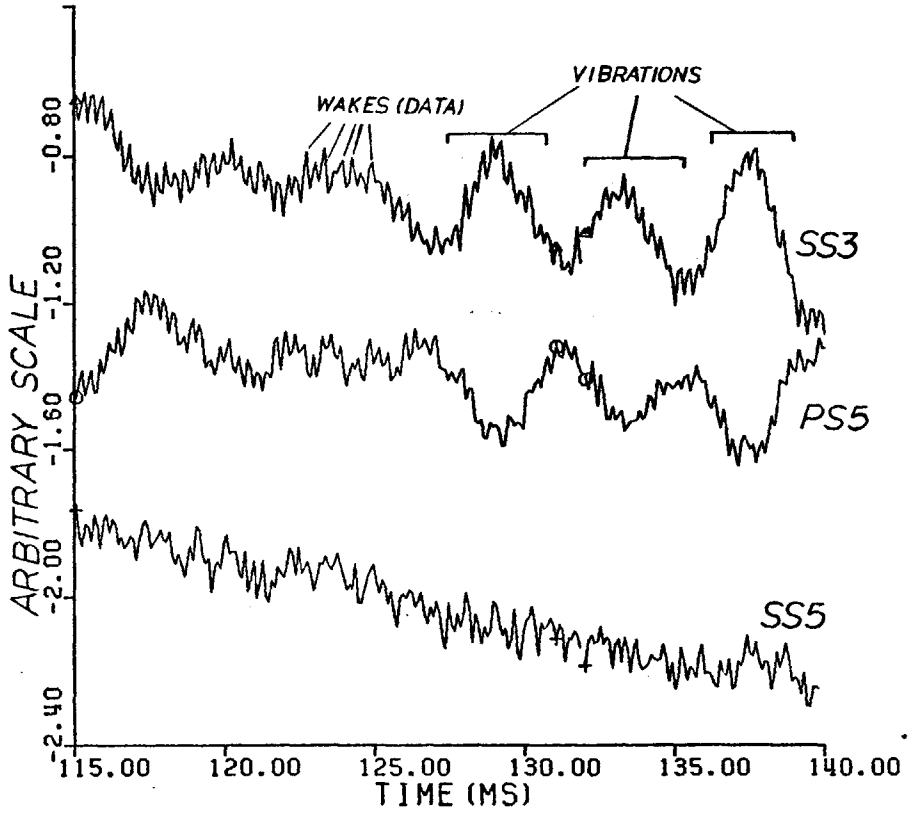

FIG. 2-8 Output Signal from Diaphragms Located at Different Chordwise Locations on the Blade

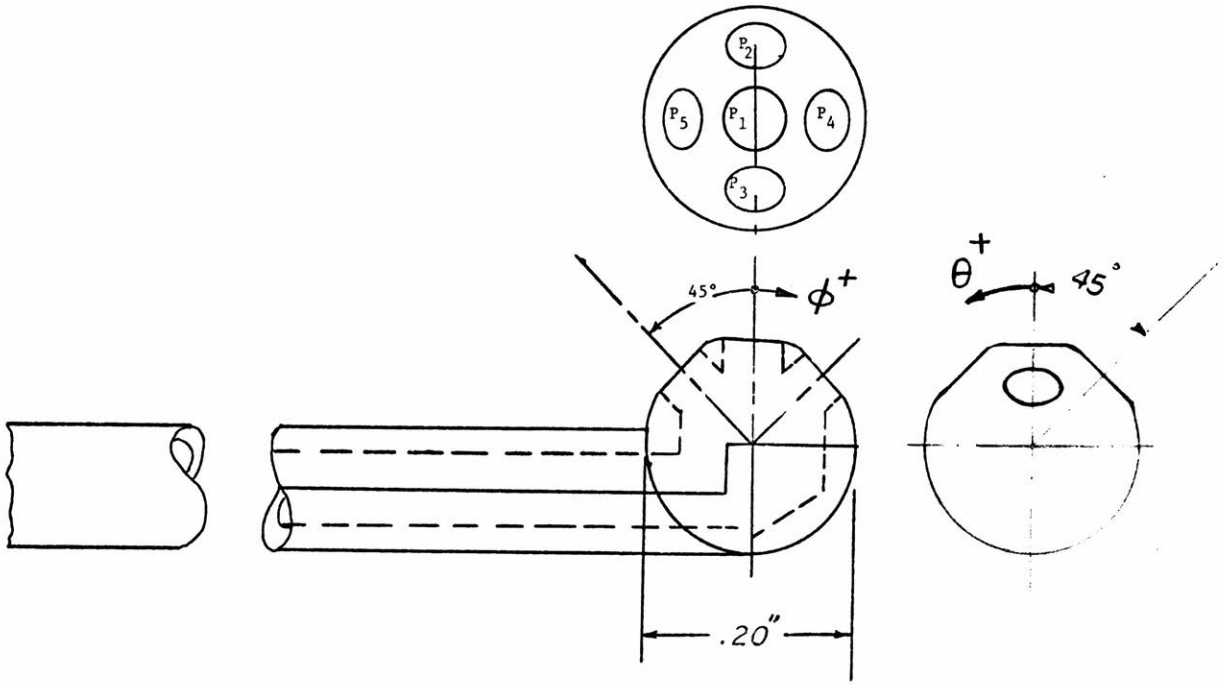

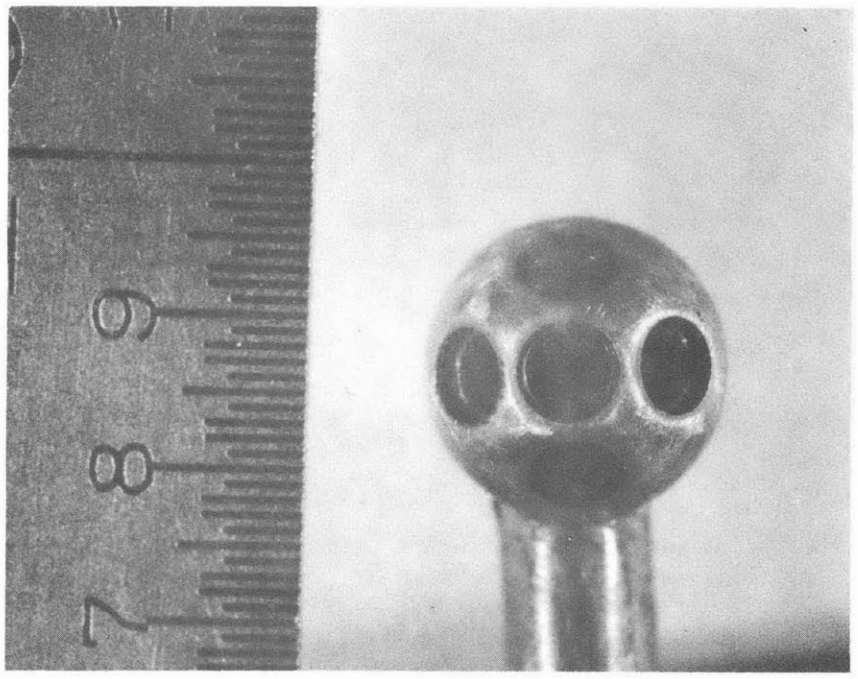

FIG. 2-9 The 5-Way Probe

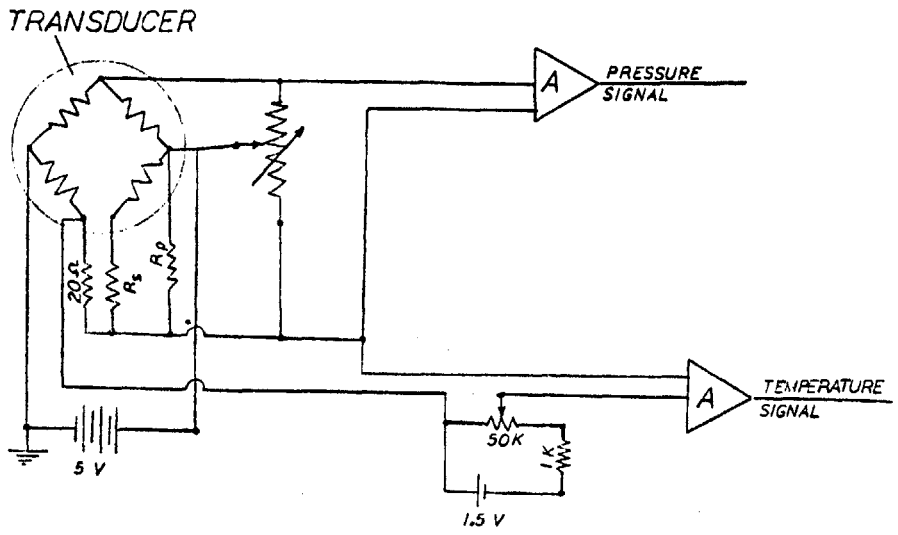

FIG. 2-10 Electrical Layout for Probe's Transducers

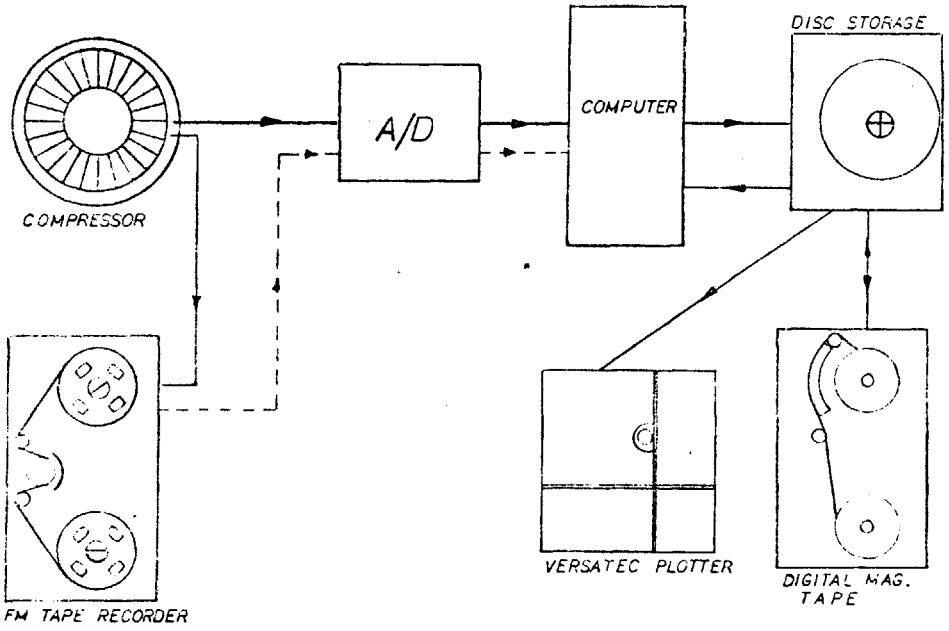

FIG. 2-11 Data Storage Setup

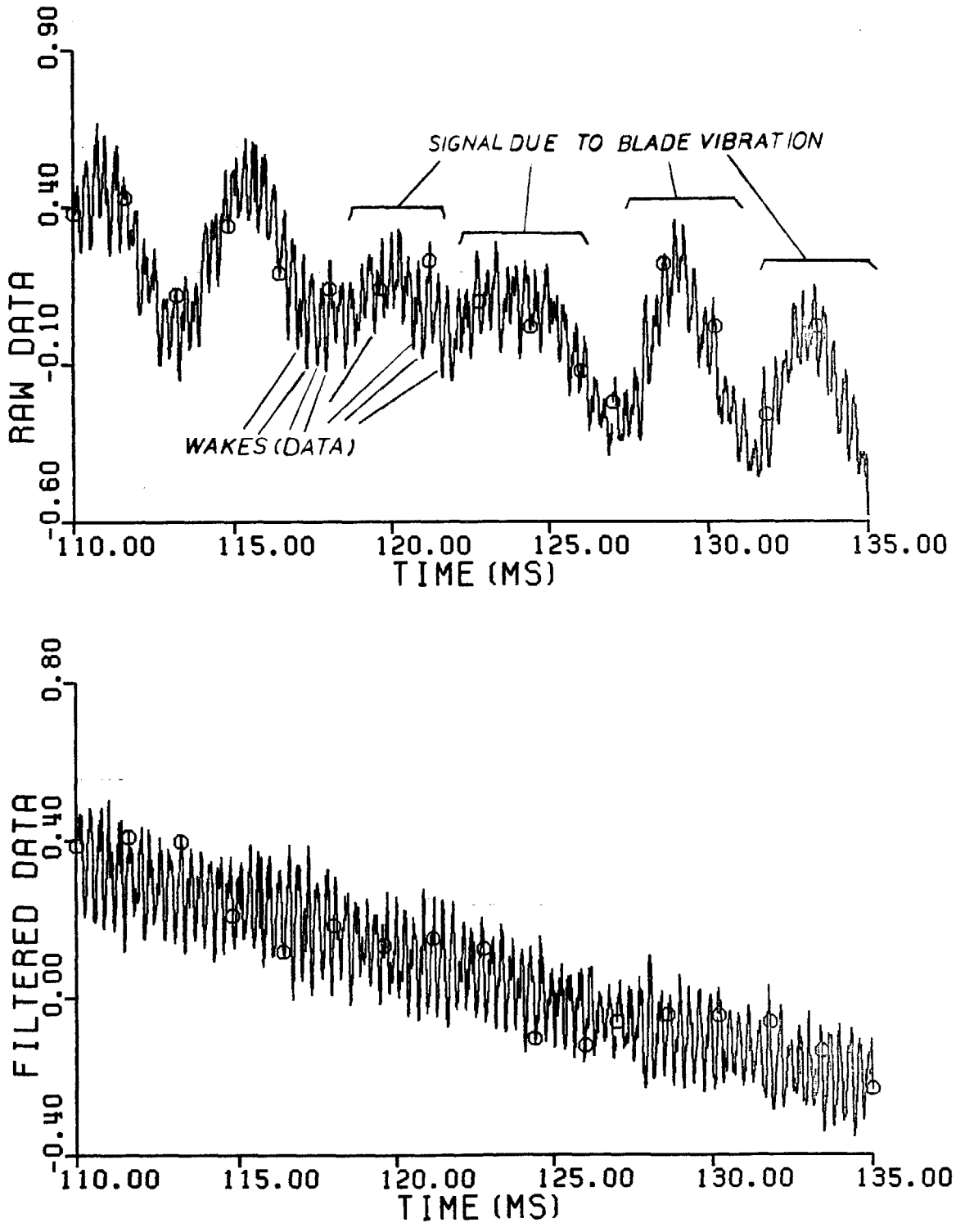

FIG. 3-1 Comparison between Raw Data and the Data Digitally Bandpass Filtered

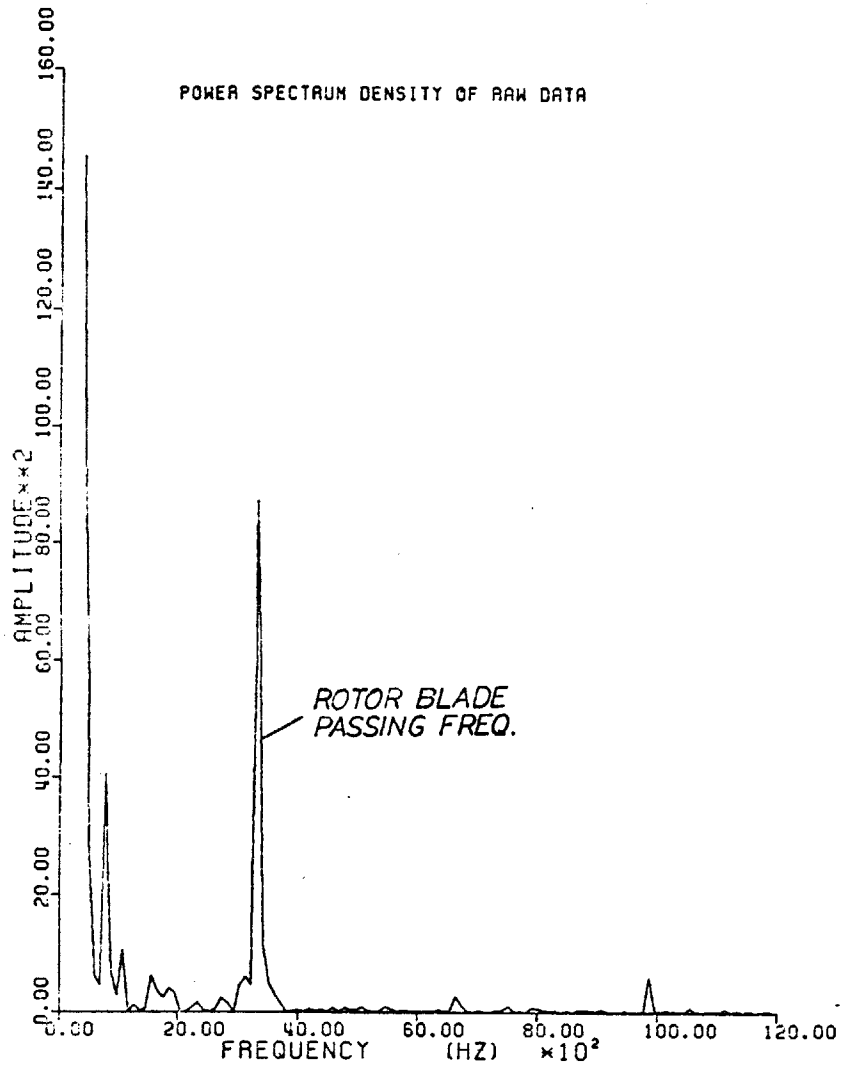

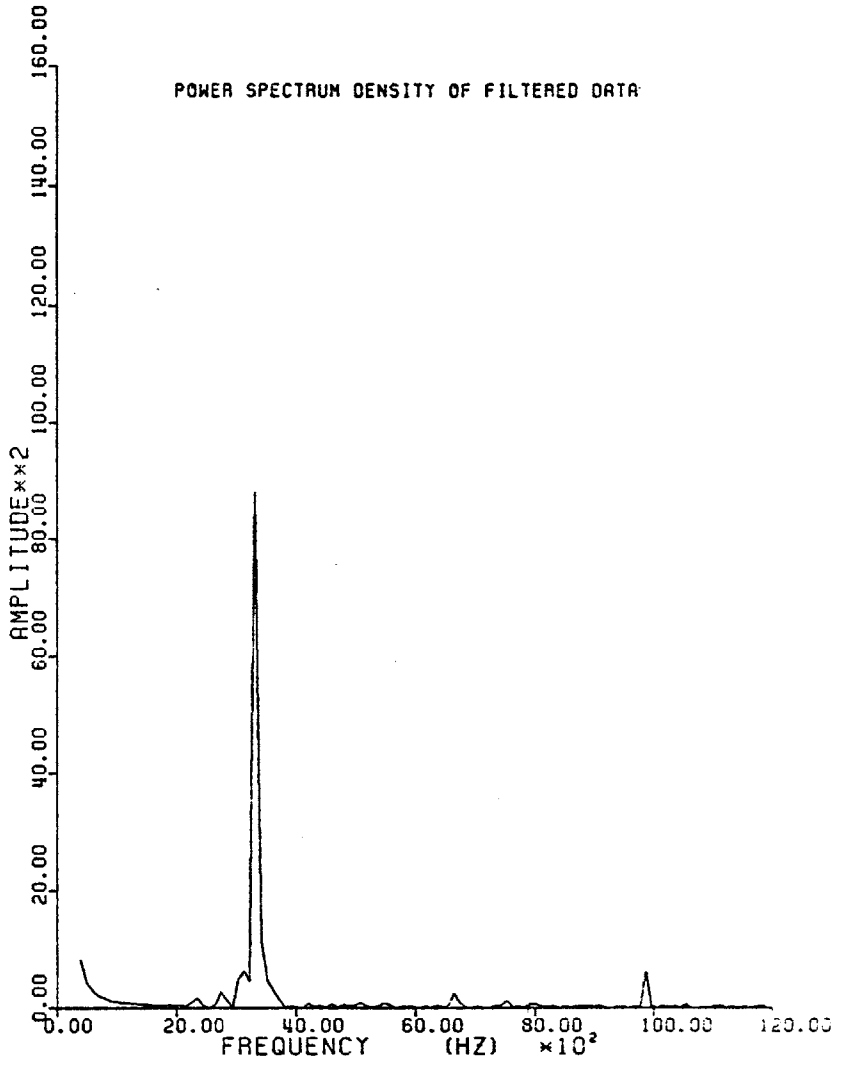

FIG. 3-2 Frequency Spectrum of Raw and Filtered Data

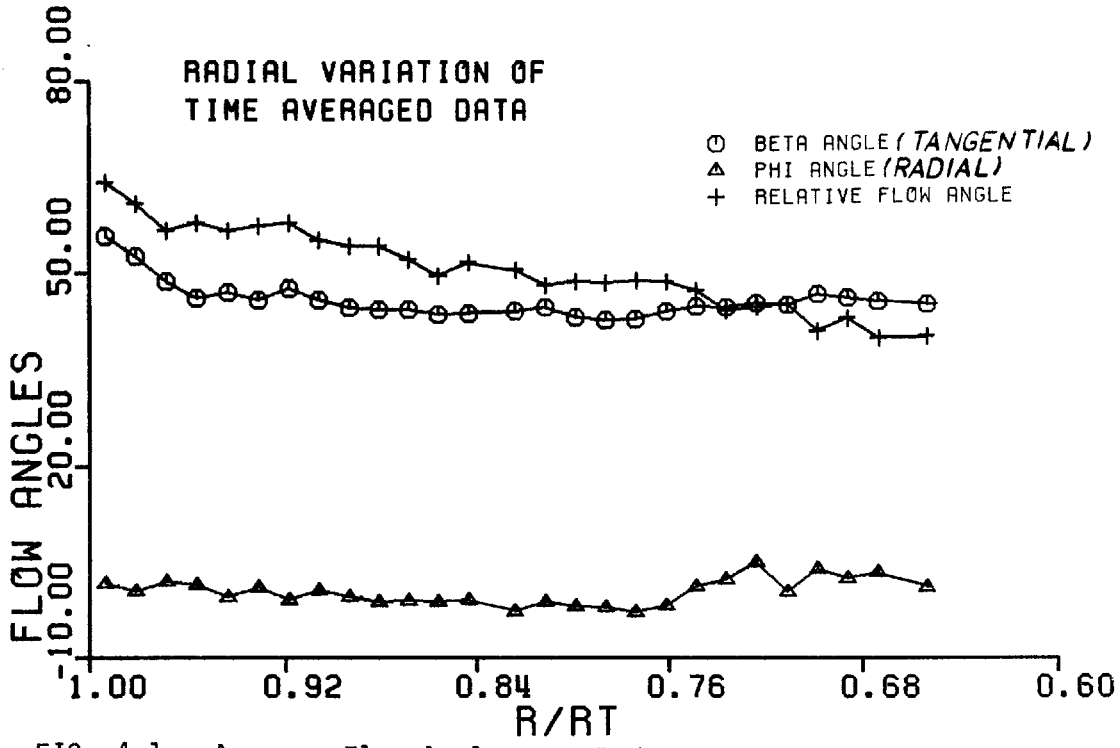

FIG. 4-1a Average Flow Angles vs. Radius Behind the Rotor

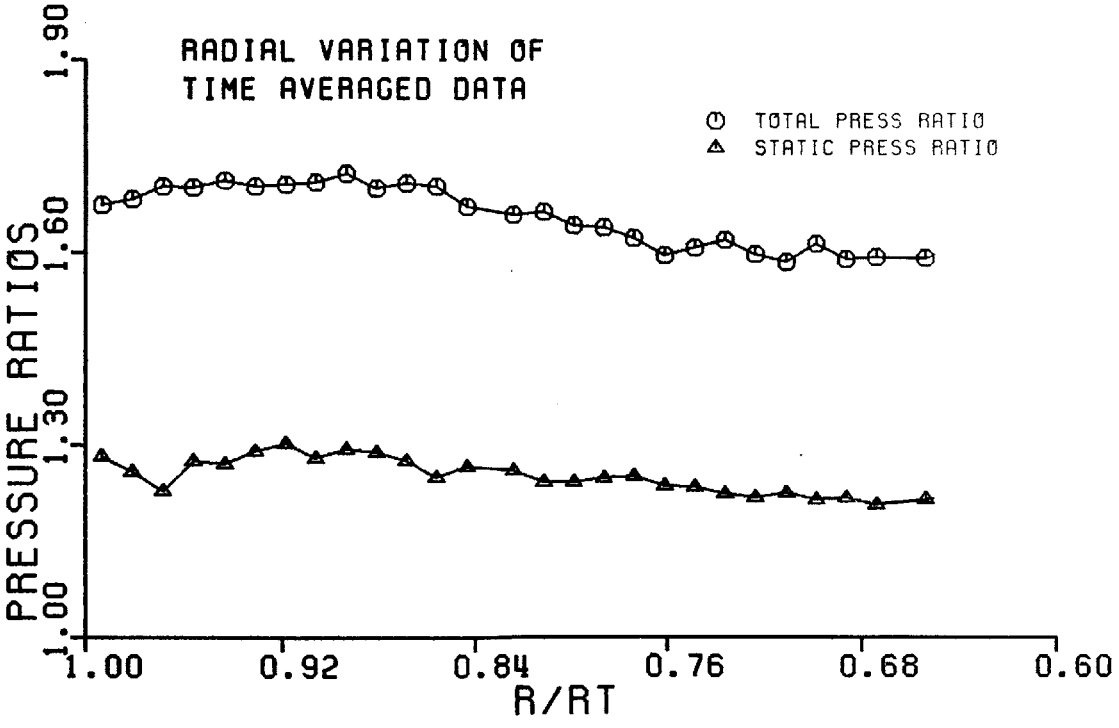

FIG. 4-1b Average Pressure Ratios vs. Radius behind the Rotor

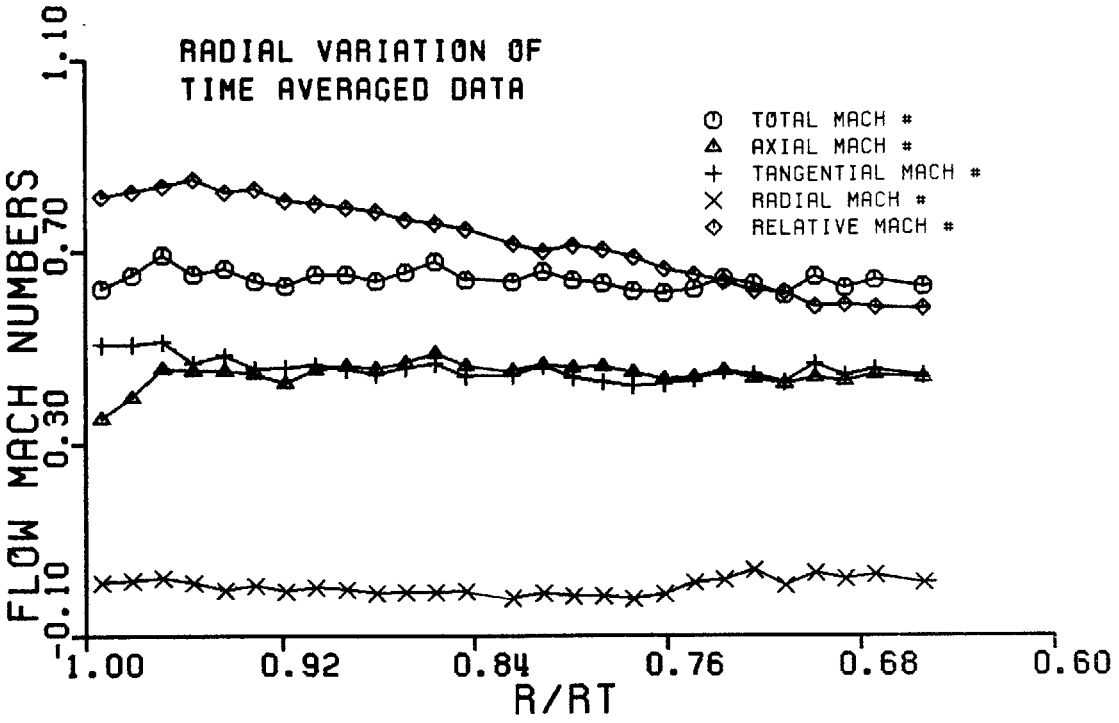

FIG. 4-2a Average Flow Mach Numbers vs. Radius behind the Rotor

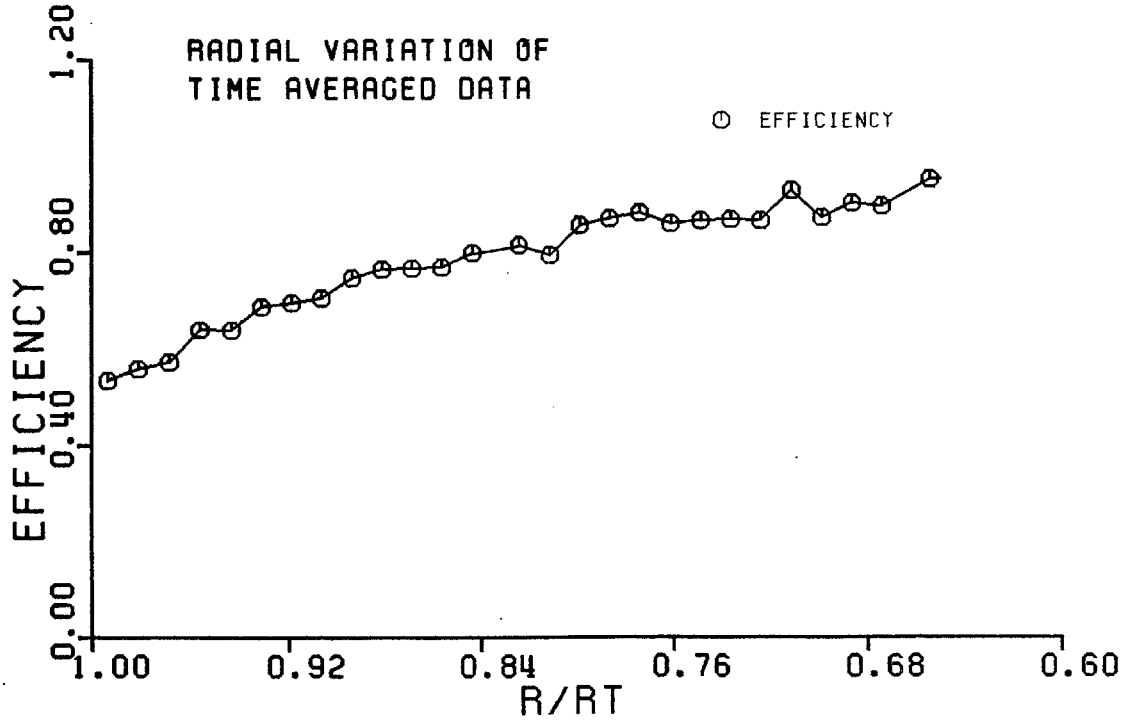

FIG. 4-2b Average Efficiency vs. Radius behind the Rotor

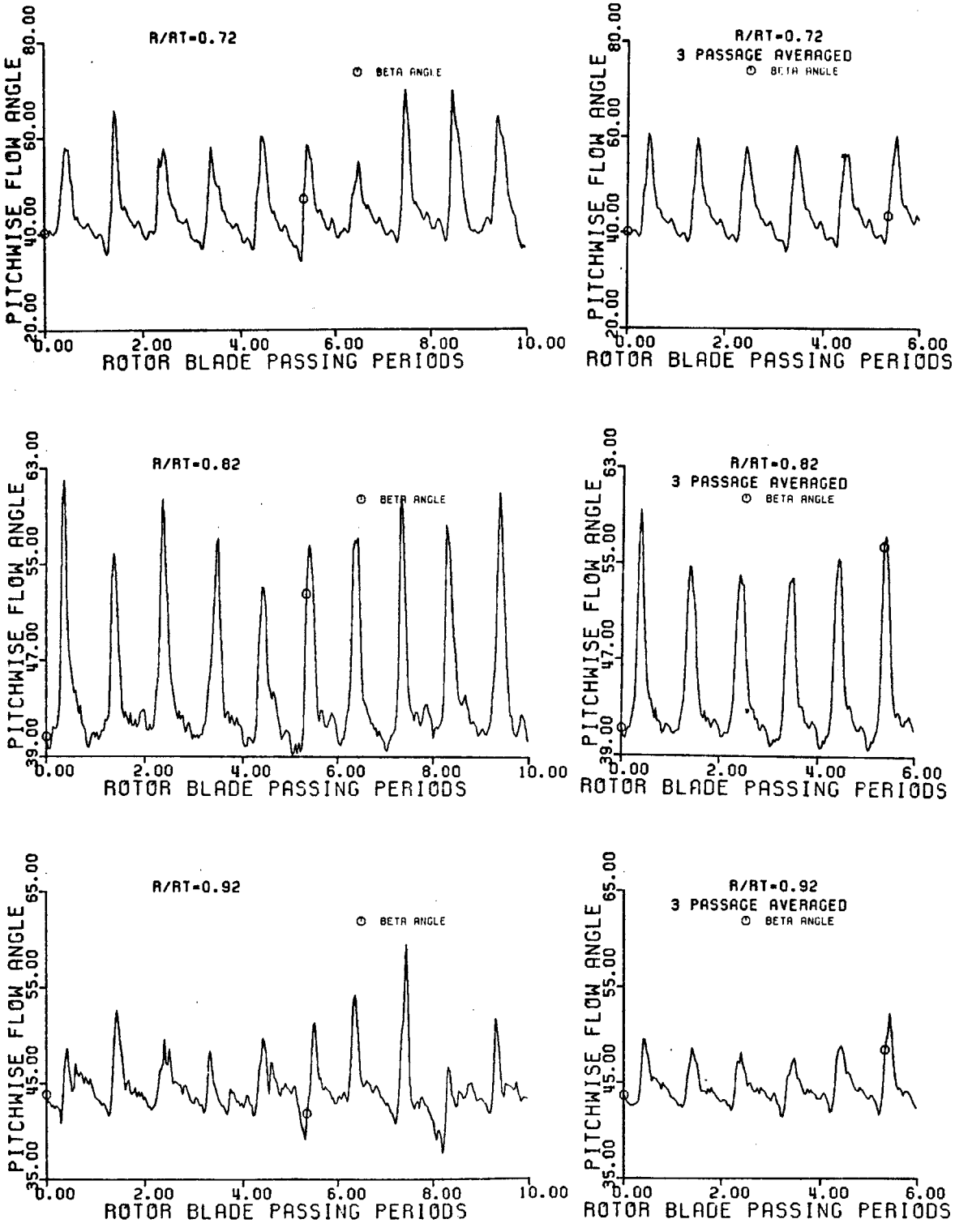

FIG. 4-3 Tangential (Pitchwise) Flow Angle behind the Rotor vs. Time for Different Radius Ratios

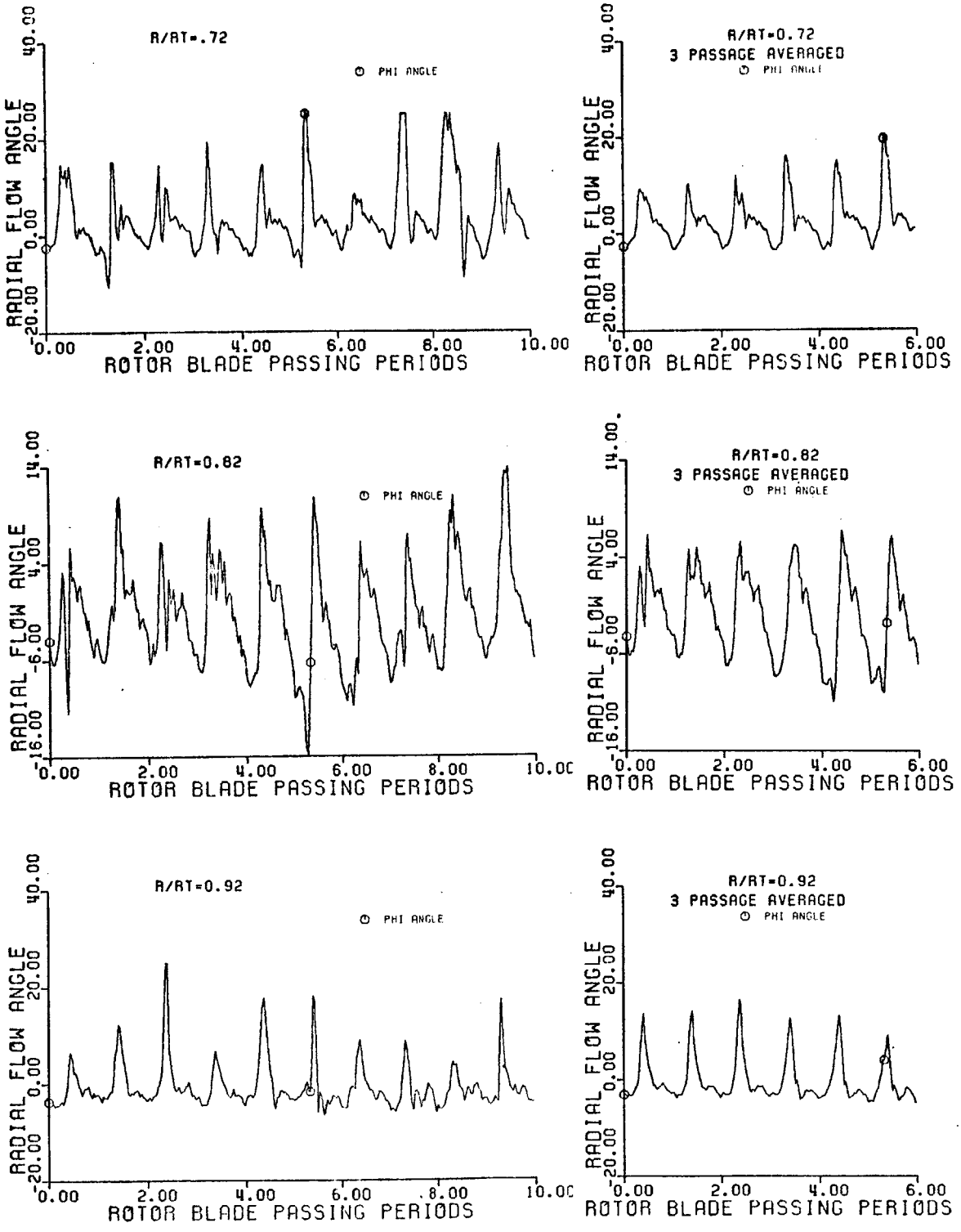

FIG. 4-4 Radial Flow Angle behind the Rotor vs. Time for Different Radius Ratios

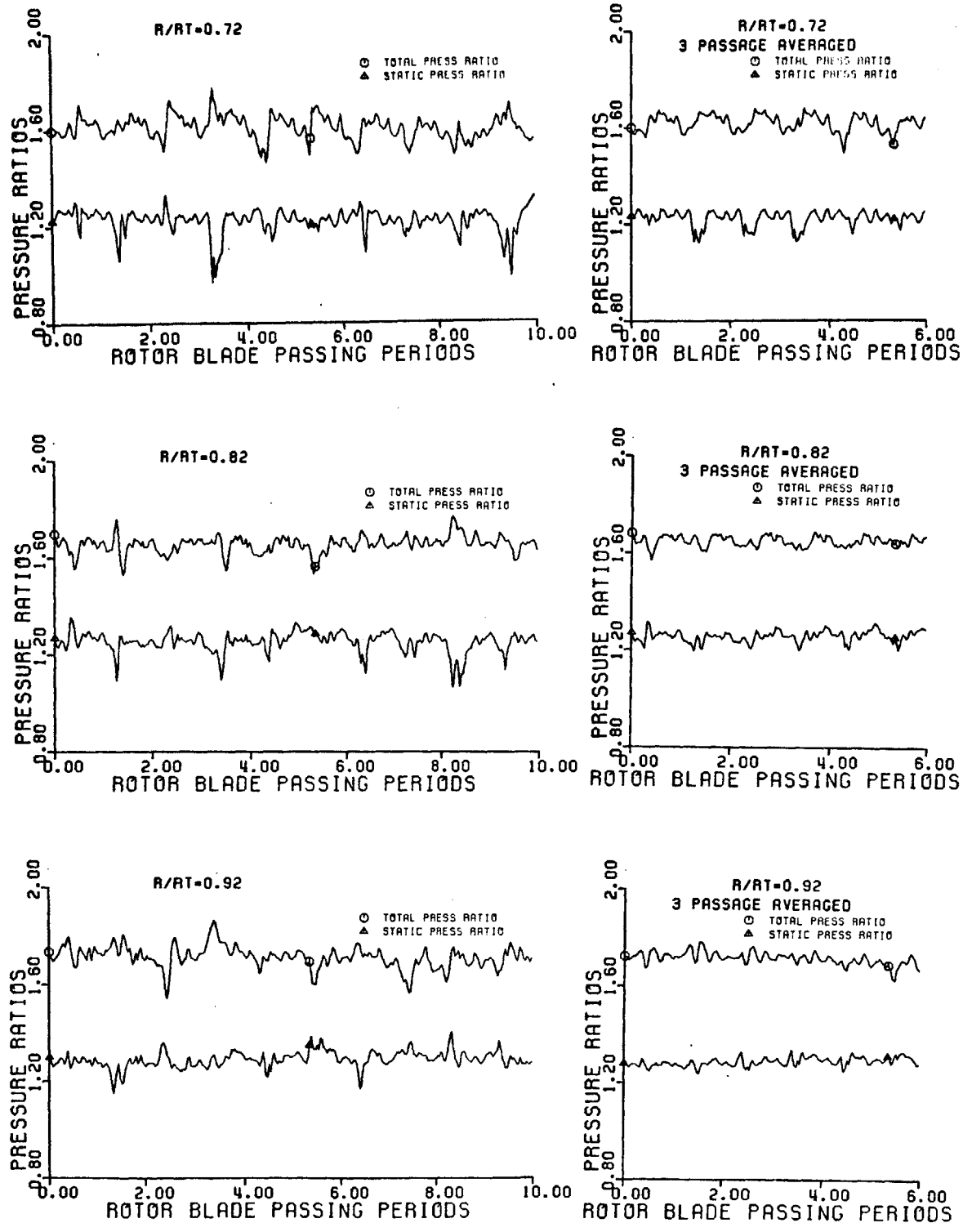

FIG. 4-5 Pressure Ratios behind the Rotor vs. Time for Different Radius Ratios

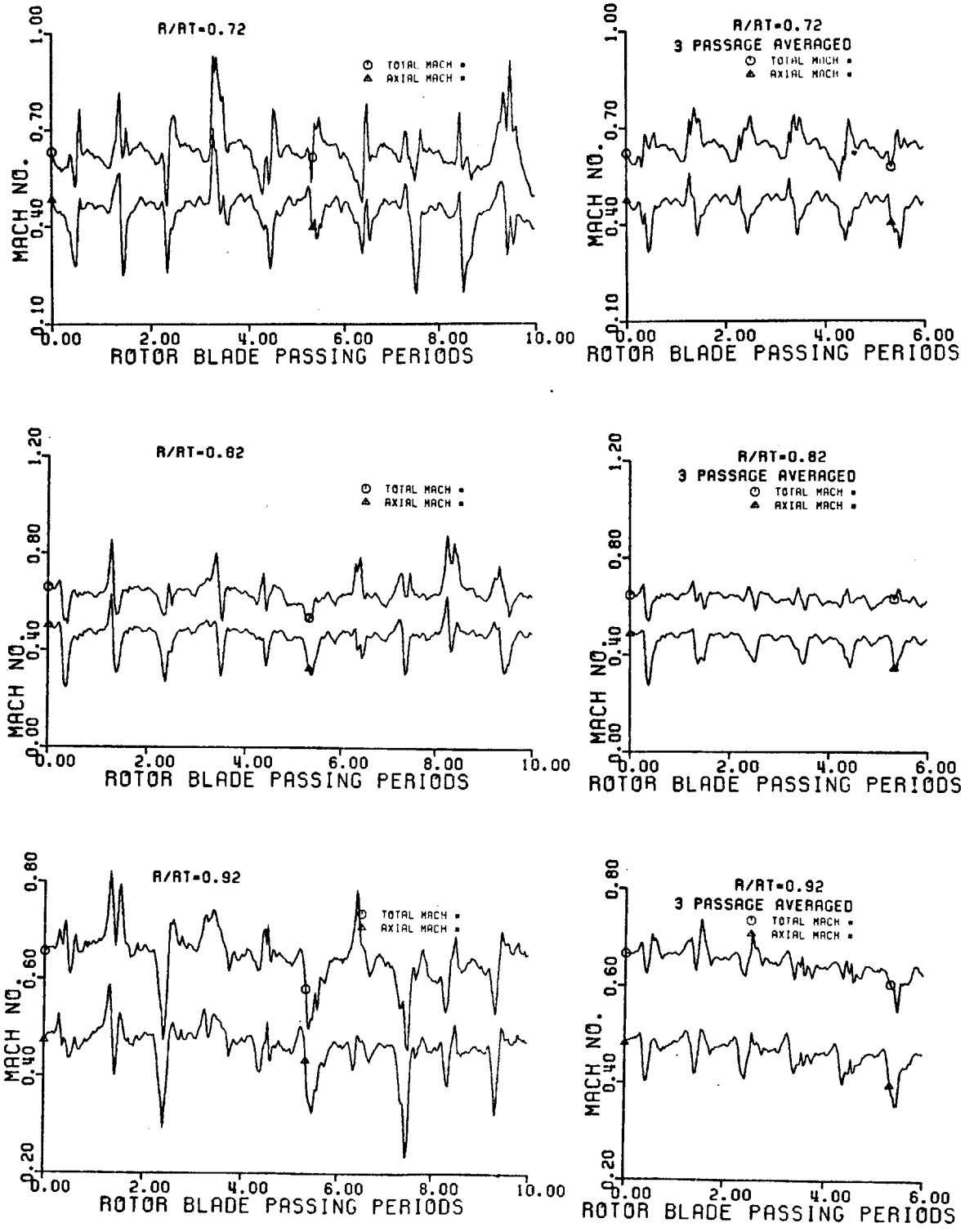

FIG. 4-6 Total and Axial Mach Numbers behind the Rotor vs. Time for Different Radius Ratios

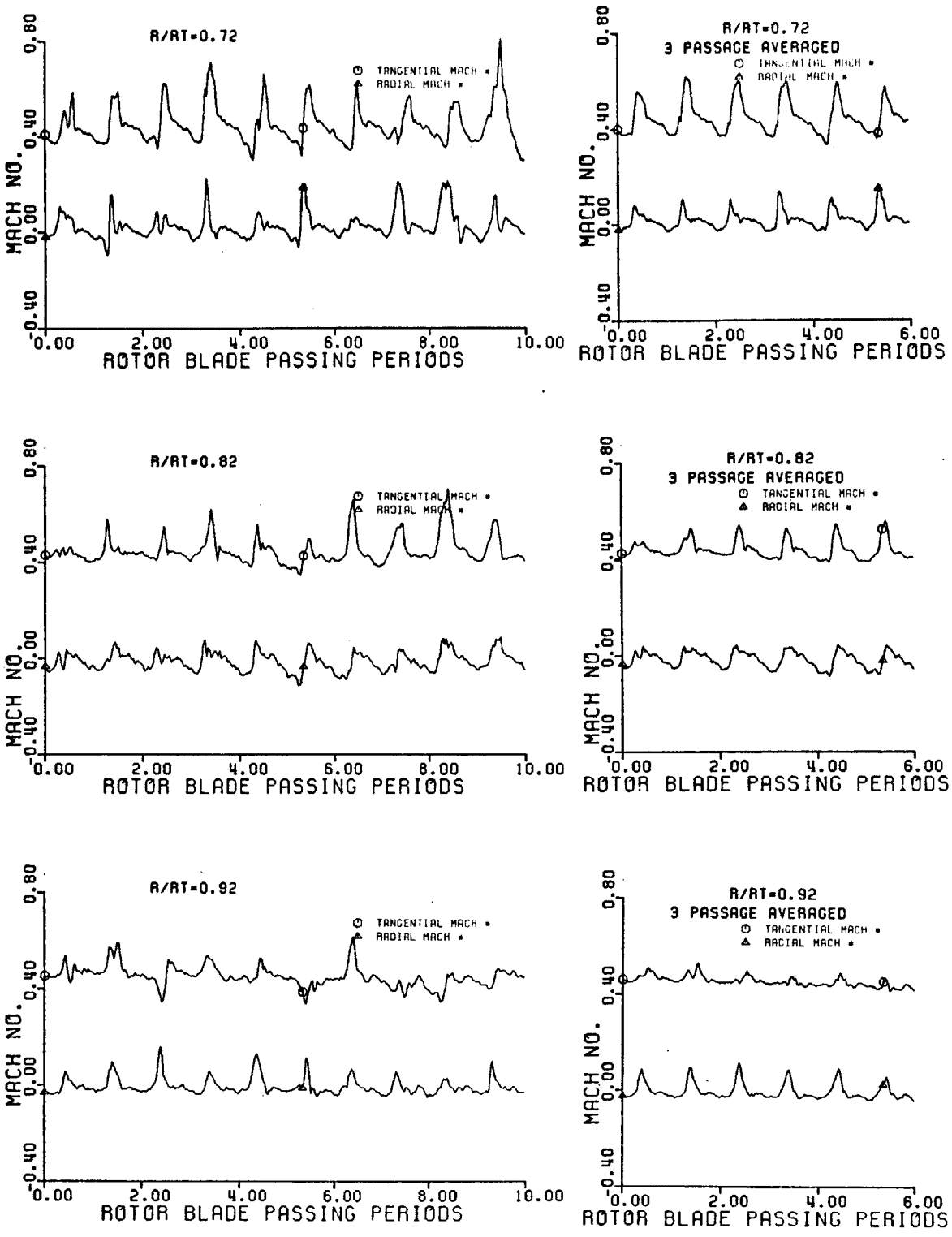

FIG. 4-7 Tangential and Radial Mach Numbers behind the Rotor vs. Time for Different Radius Ratios

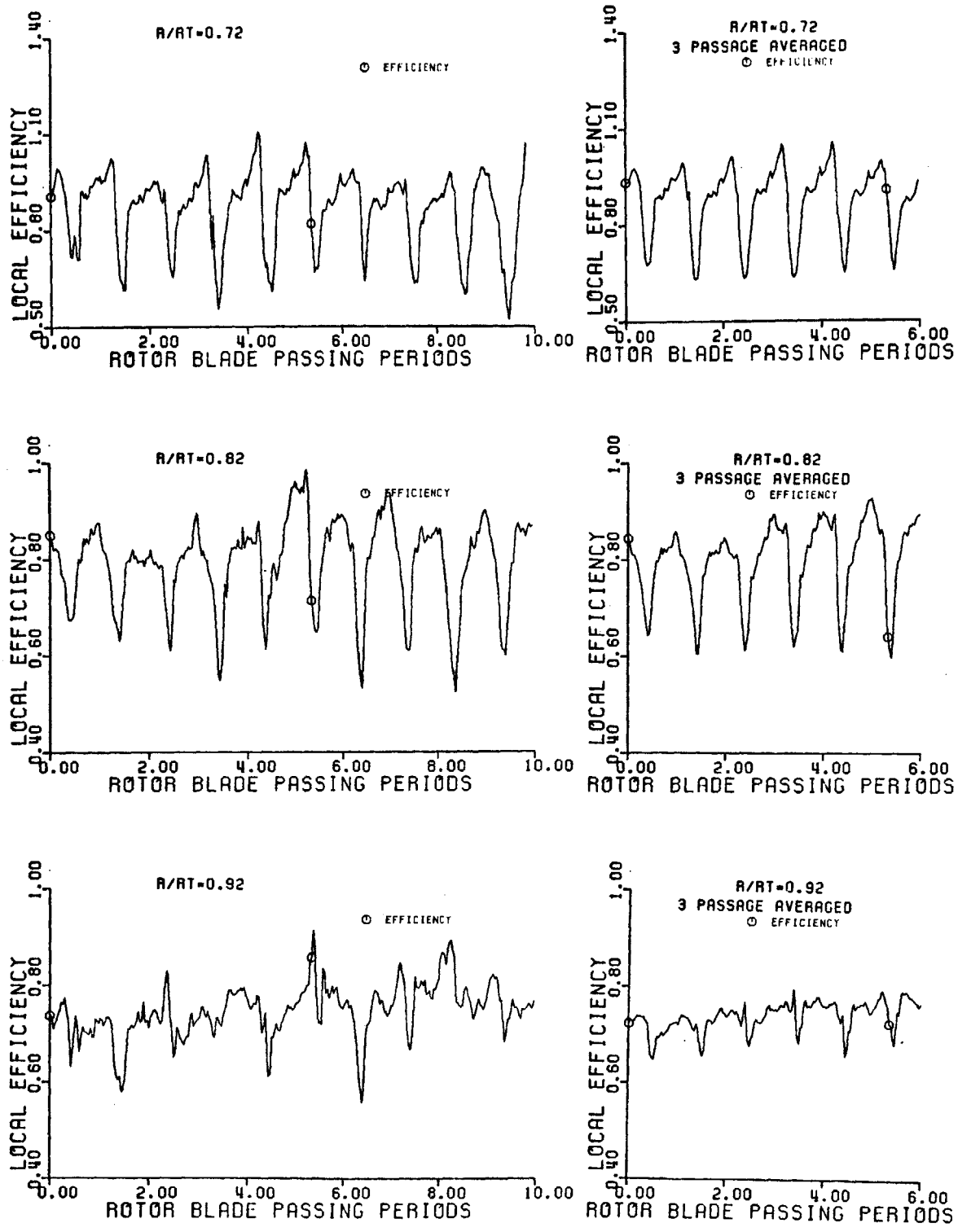

FIG. 4-8 Local Efficiency behind the Rotor vs. Time for Different Radius Ratios

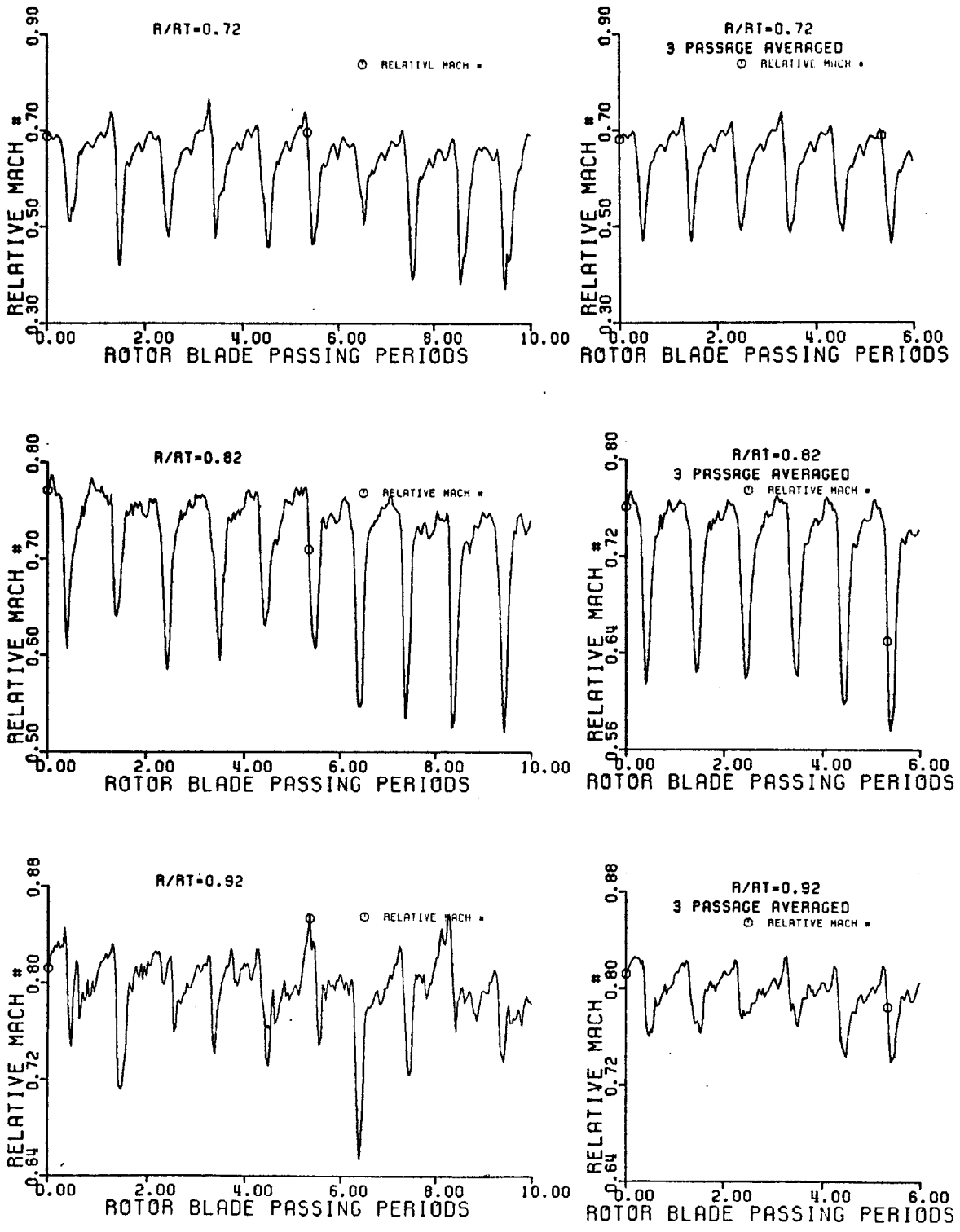

FIG. 4-9 Relative Flow Mach Number behind the Rotor vs. Time for Different Radius Ratios

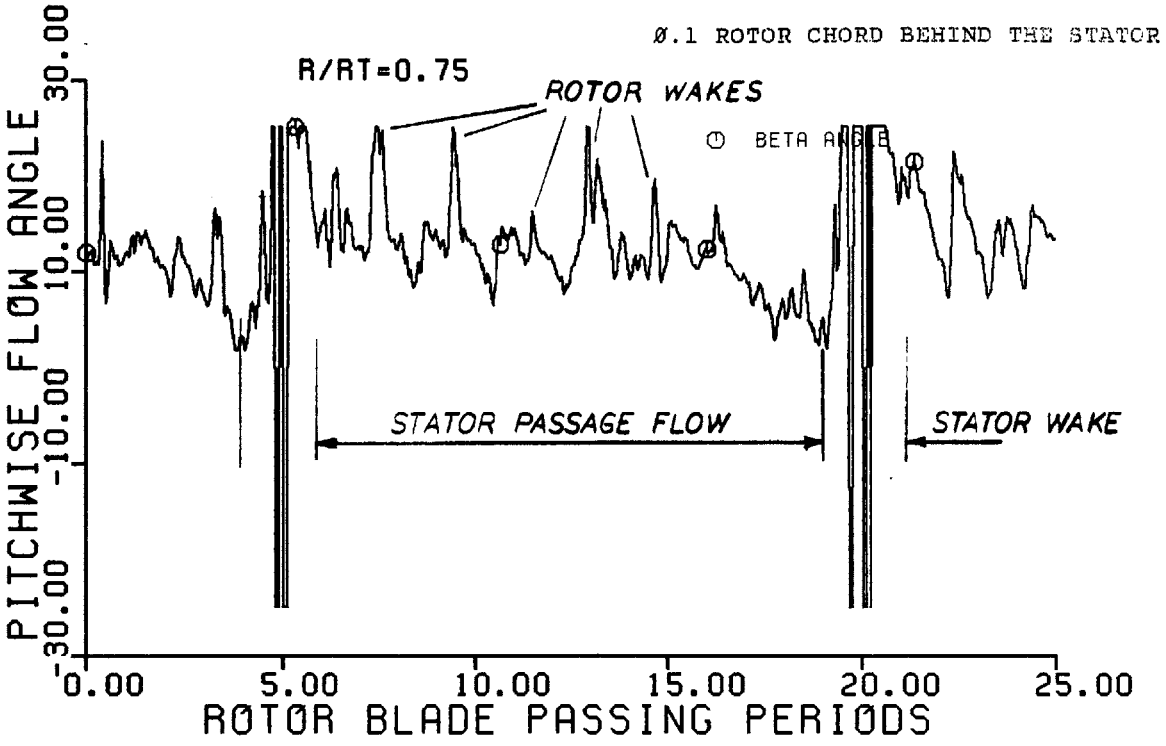

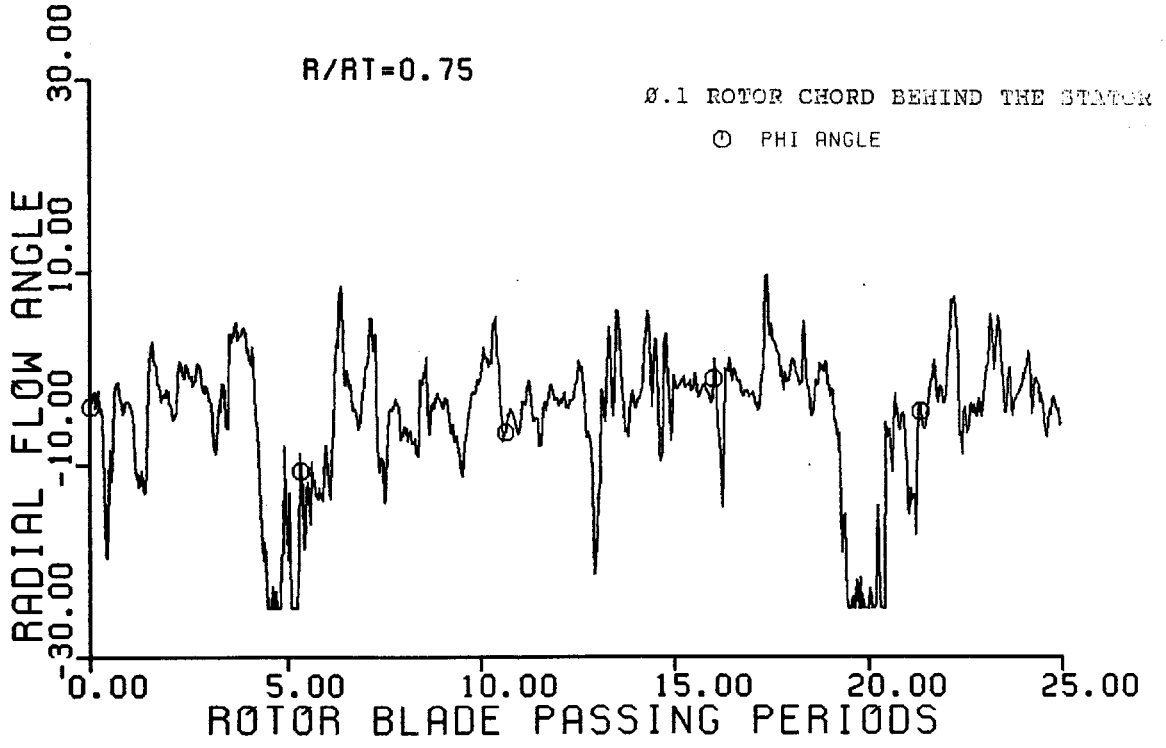

FIG. 4-10 Flow Angles behind the Stator, $R/R_T = 0.75$

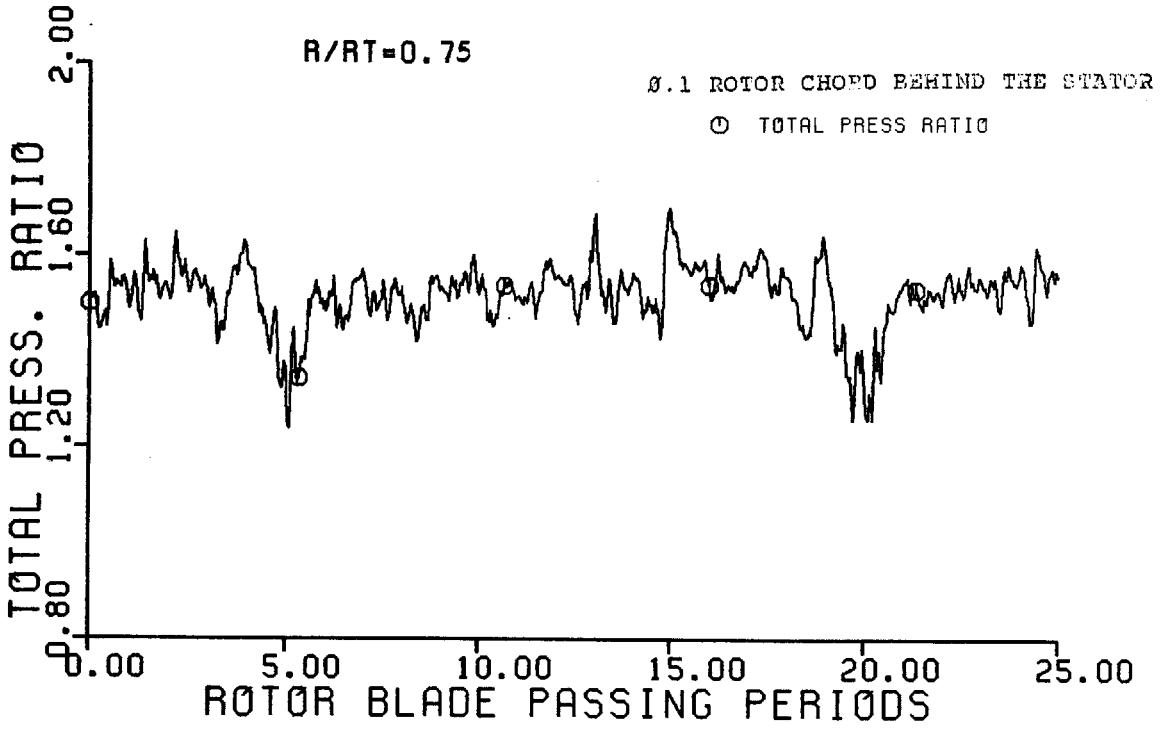

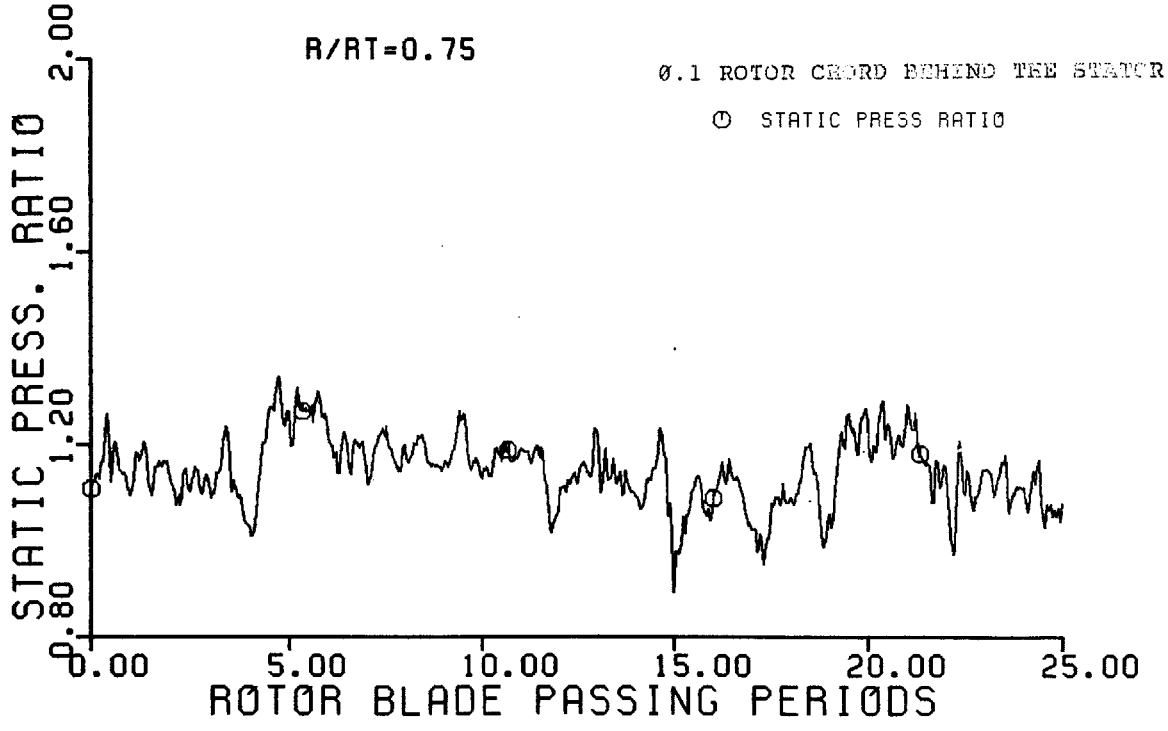

FIG. 4-11 Pressure Ratios behind the Stator, $R/R_T = 0.75$

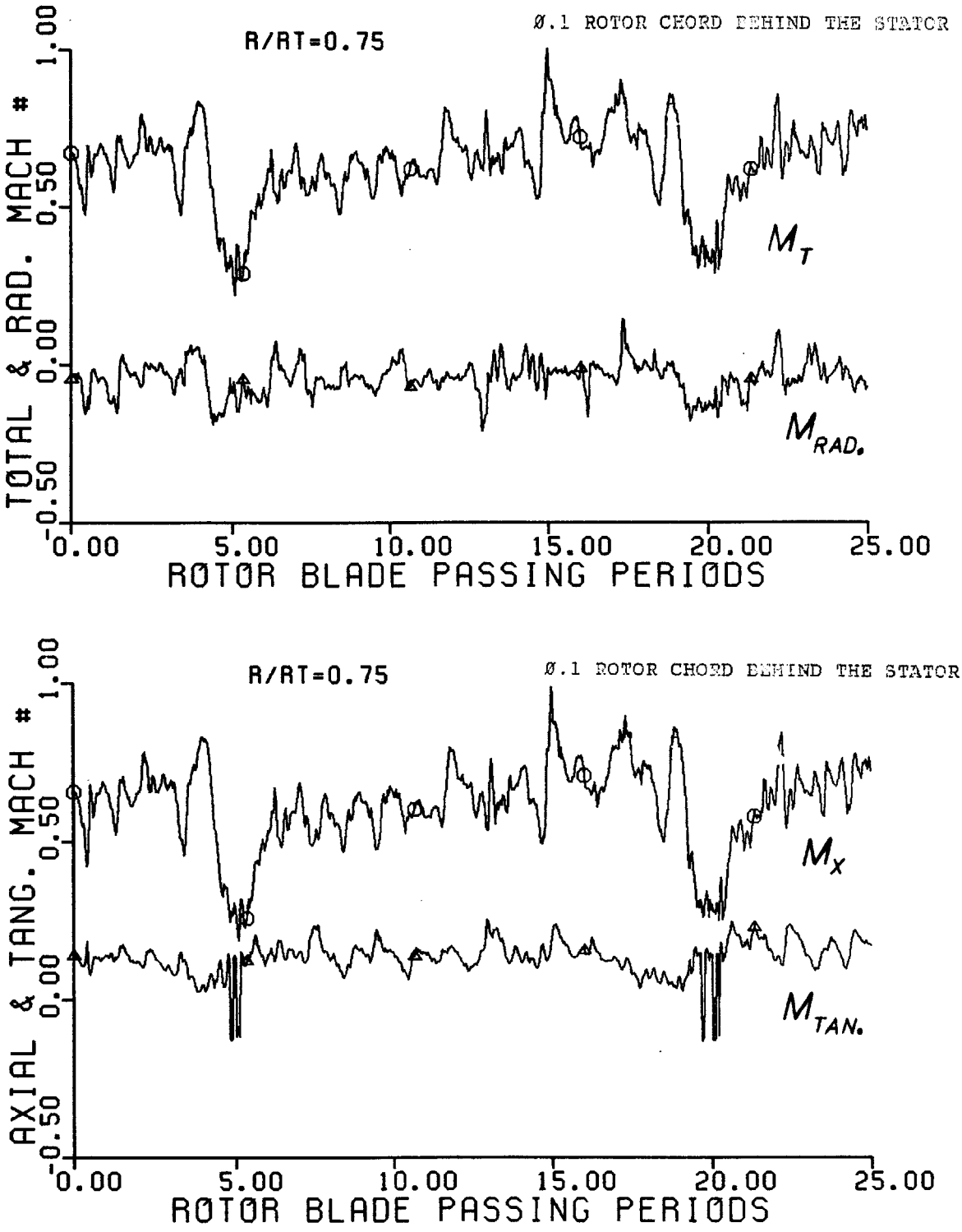

FIG. 4-12 Flow Mach Numbers behind the Stator, $R/R_T = 0.75$

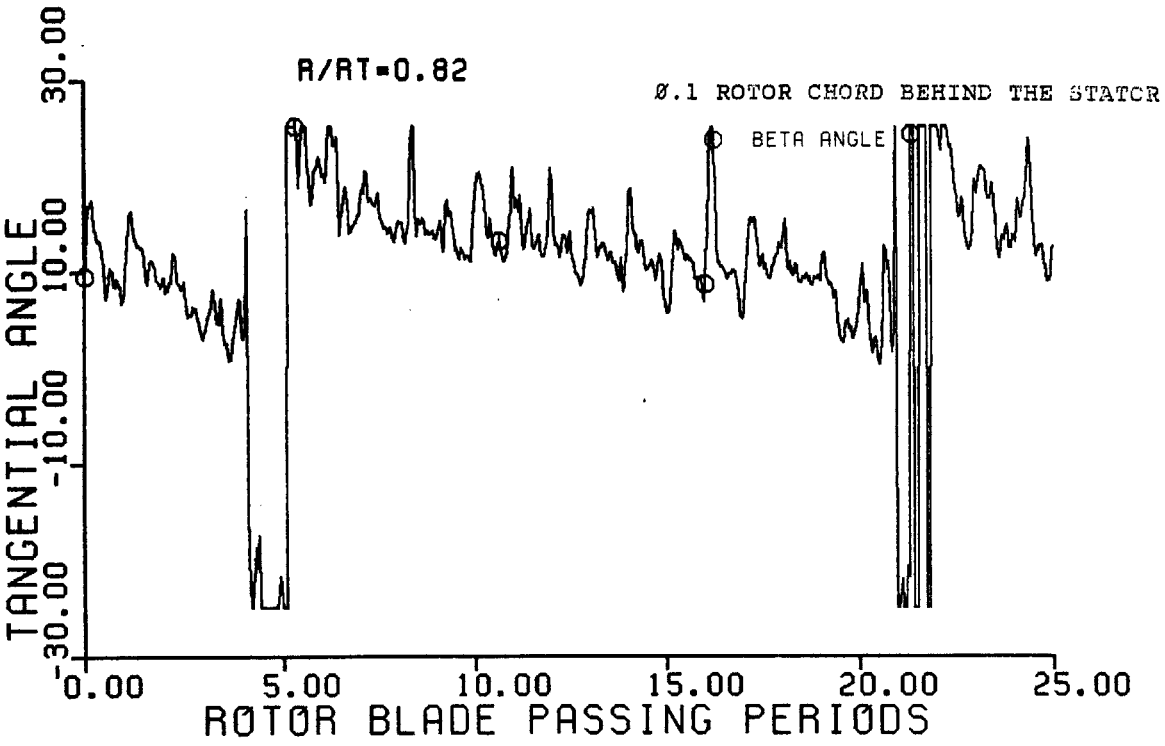

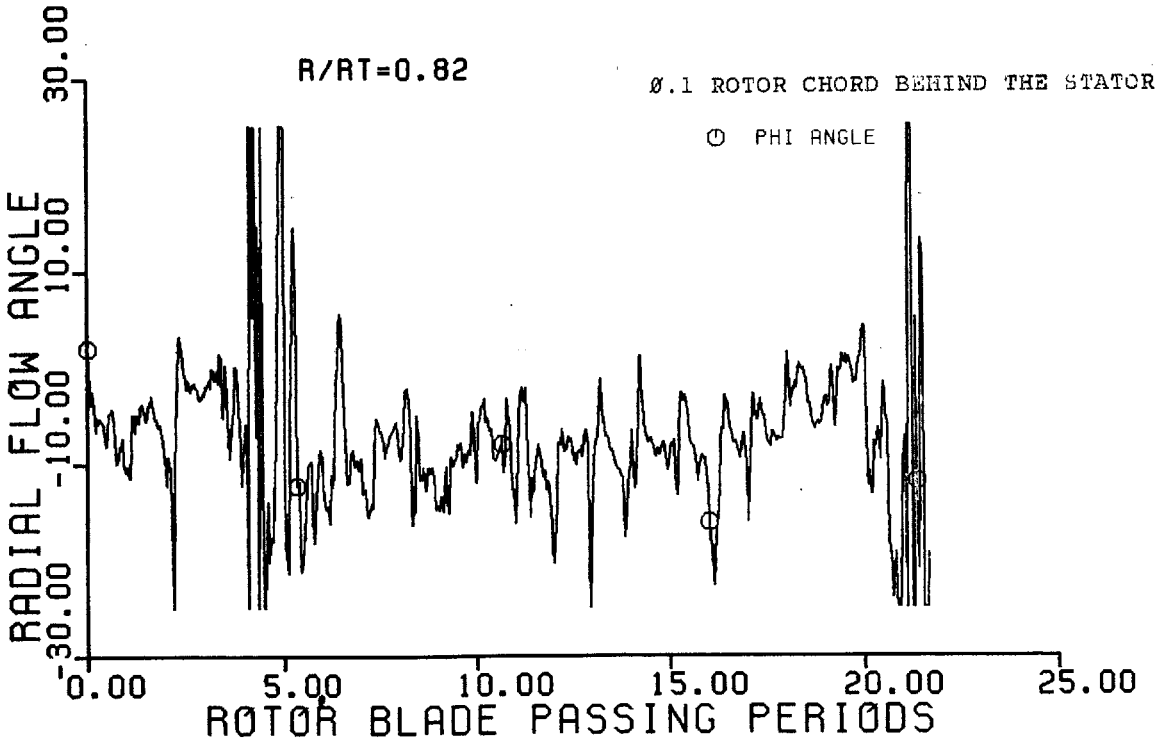

FIG. 4-13 Flow Angles behind the Stator, $R/R_T = 0.82$

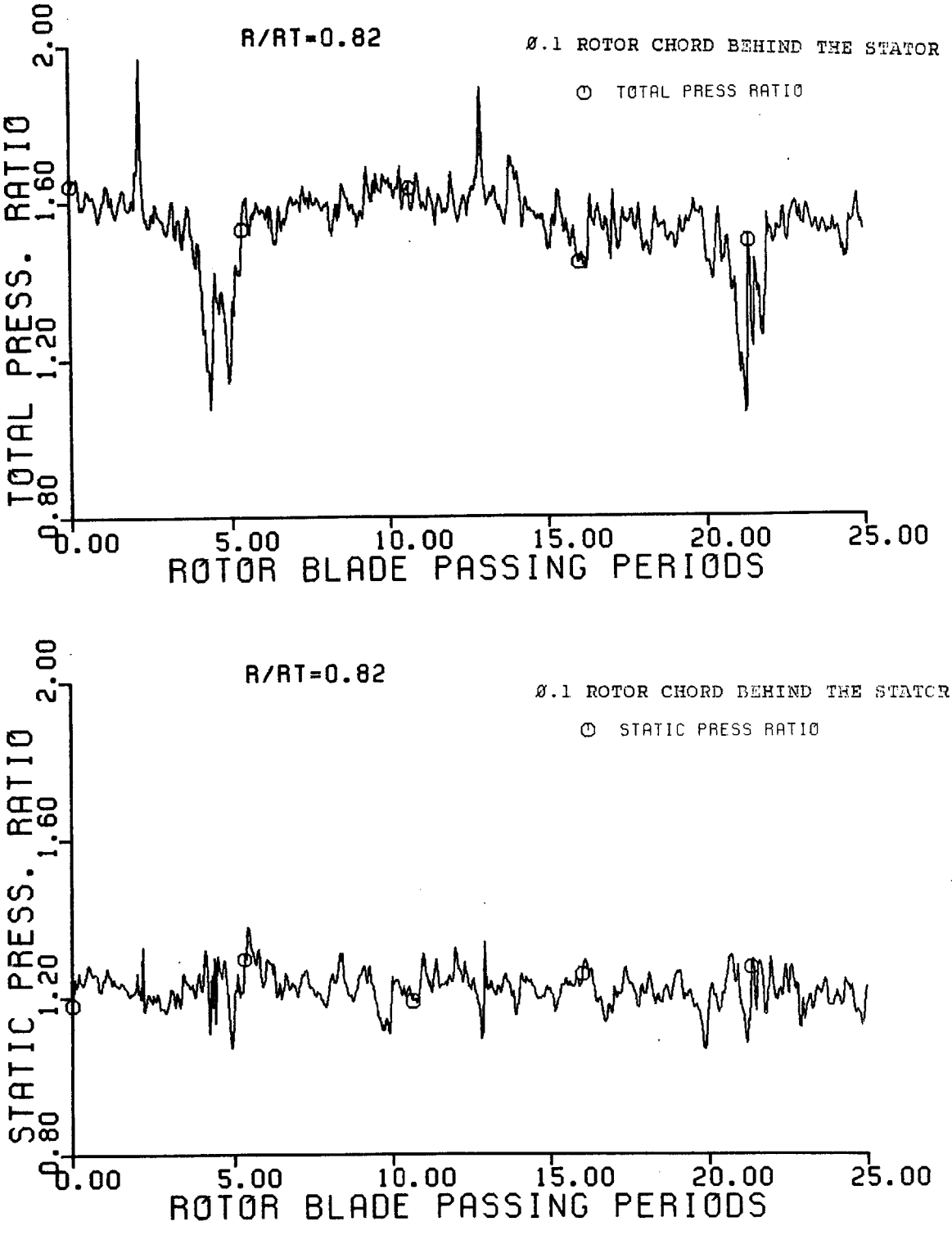

FIG. 4-14 Pressure Ratios behind the Stator, $R/R_T = 0.82$

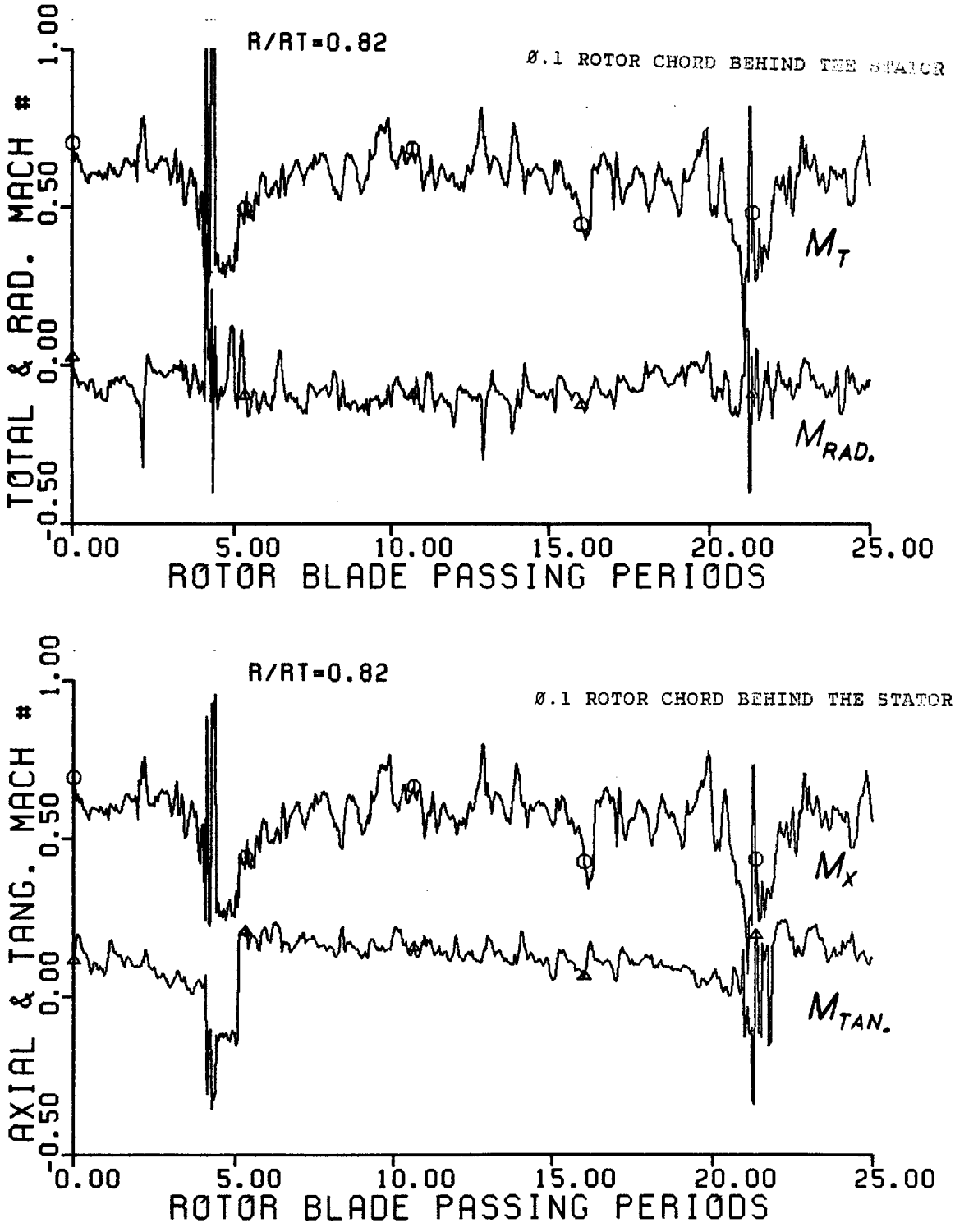

FIG. 4-15 Flow Mach Numbers behind the Stator, $R/R_T = 0.82$

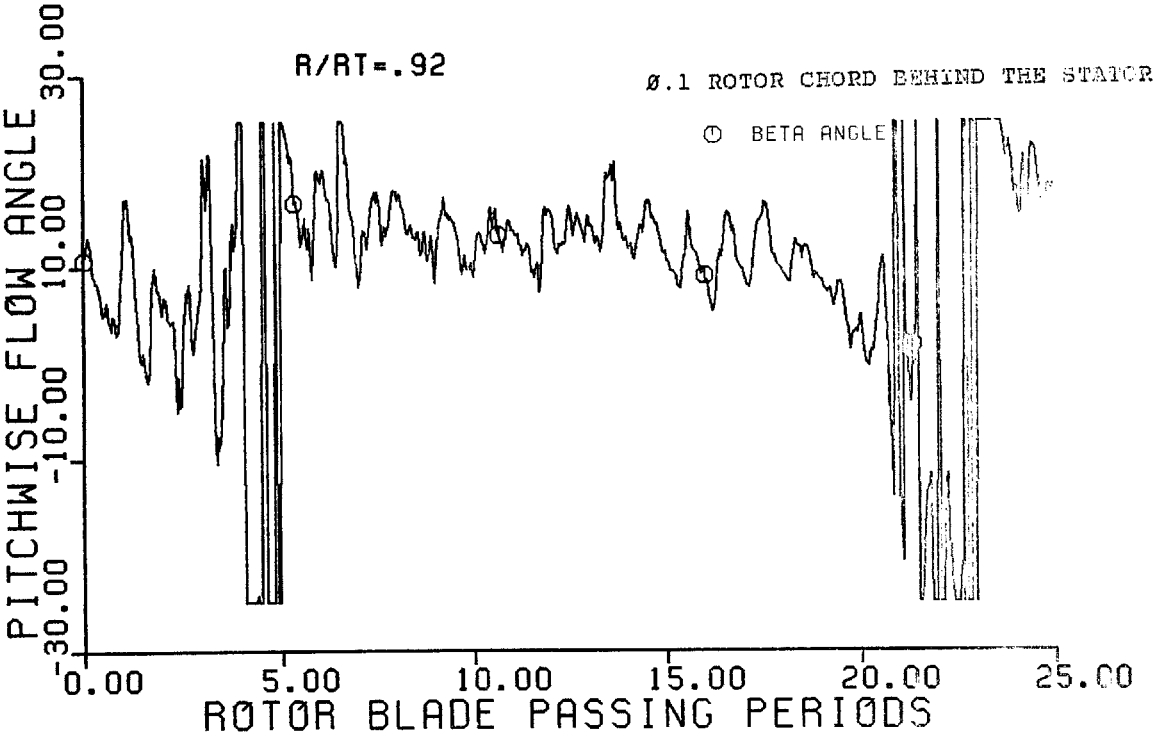

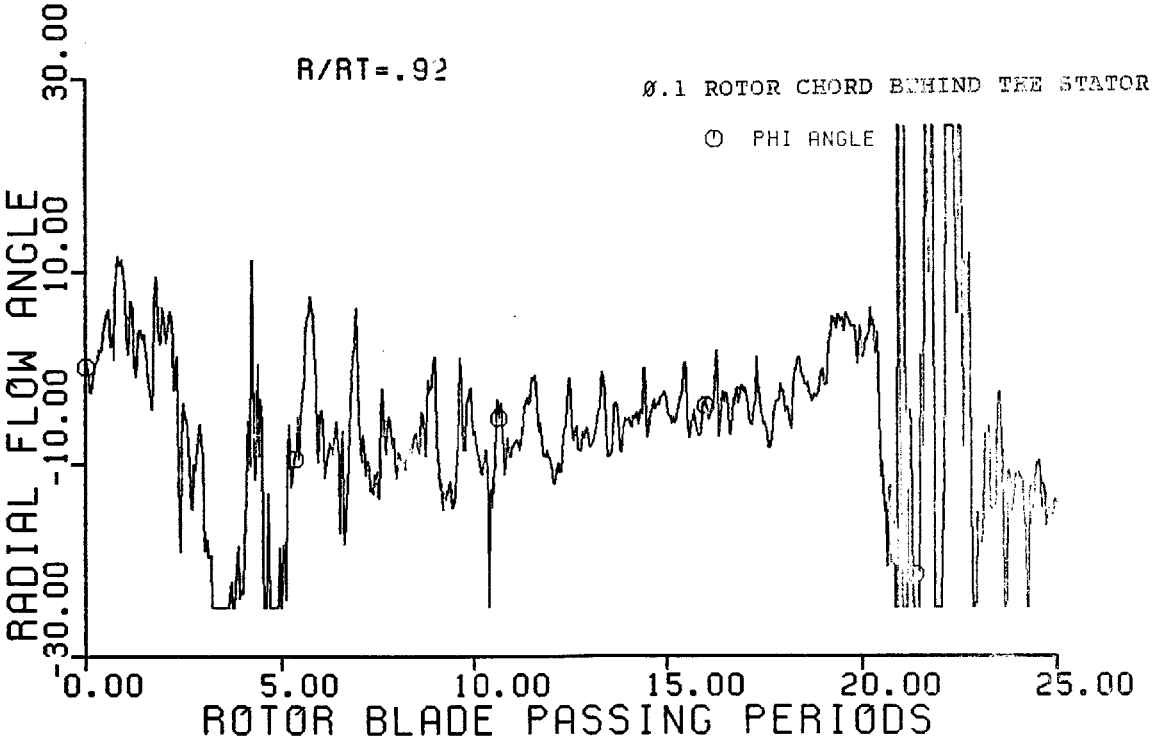

FIG. 4-16 Flow Angles behind the Stator, $R/R_T = 0.92$

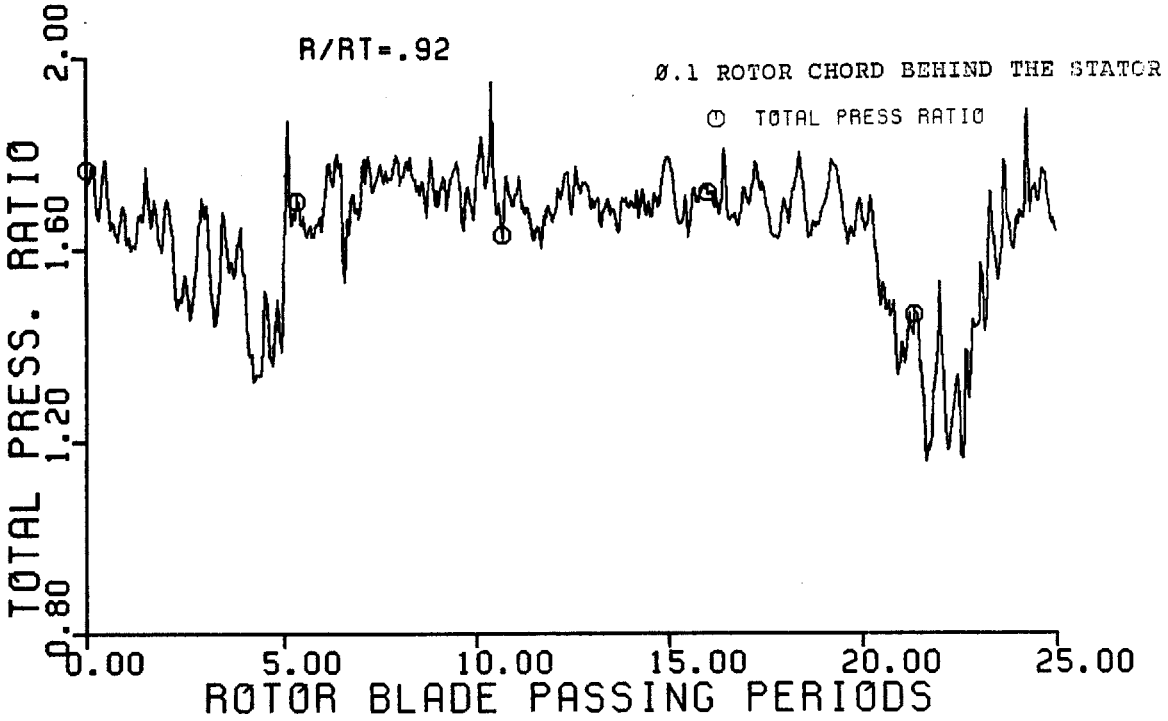

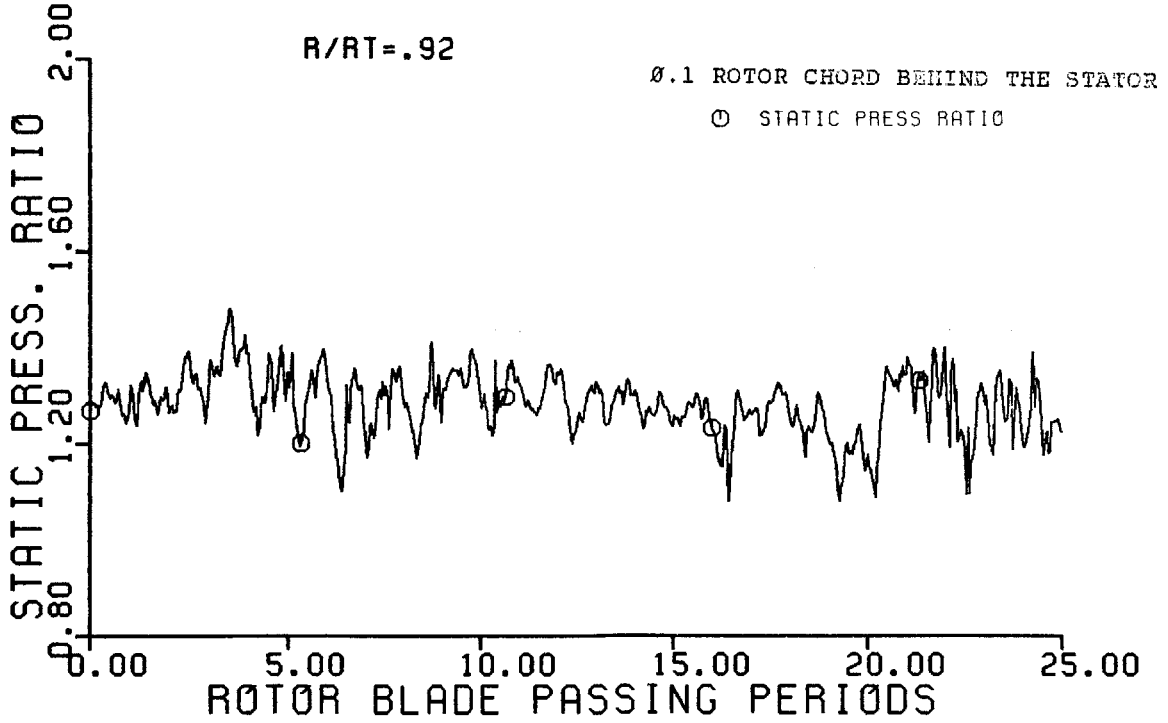

FIG. 4-17 Pressure Ratios behind the Stator, $R/R_T = 0.92$

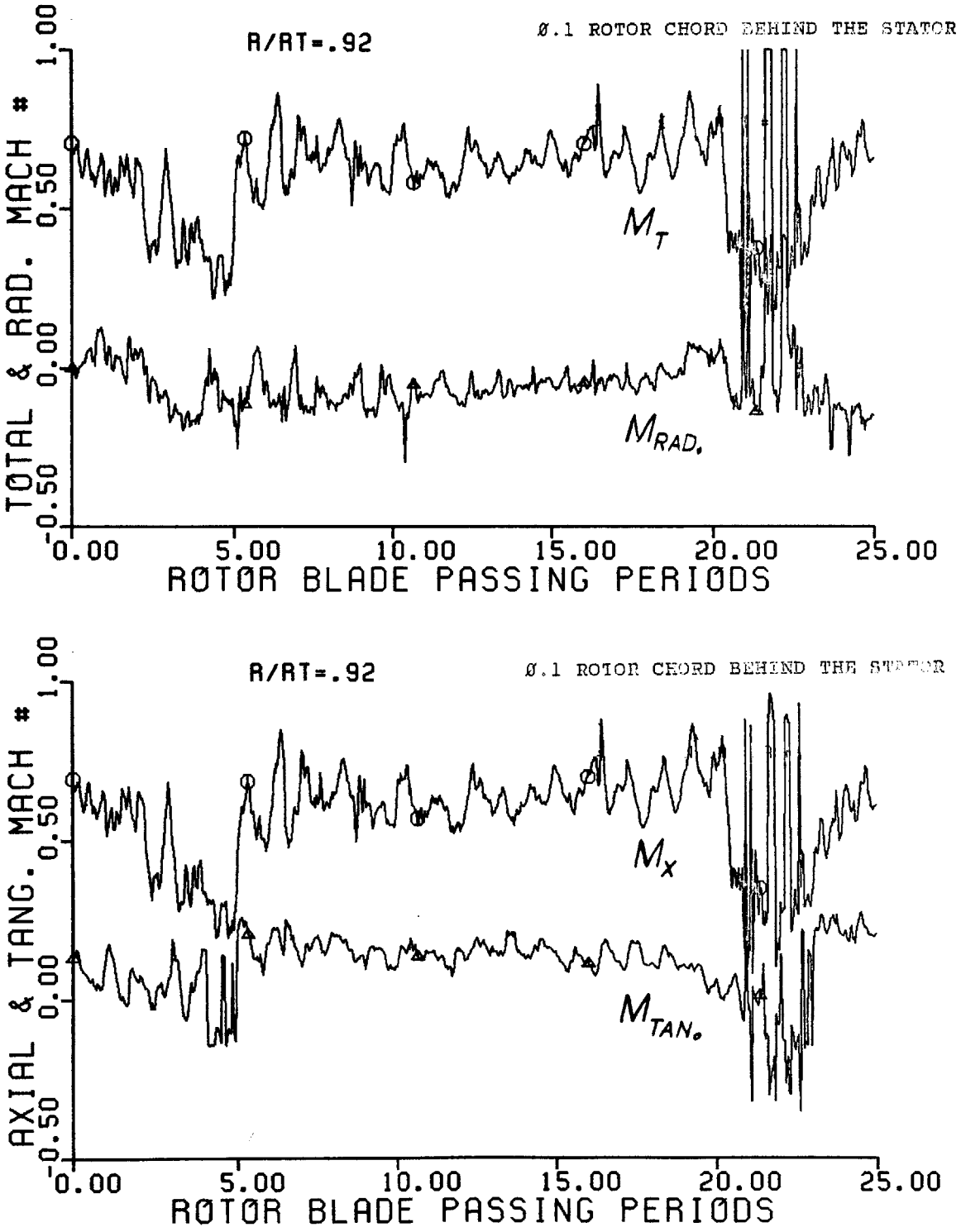

FIG. 4-18 Flow Mach Numbers behind the Stator, $R/R_T = 0.92$

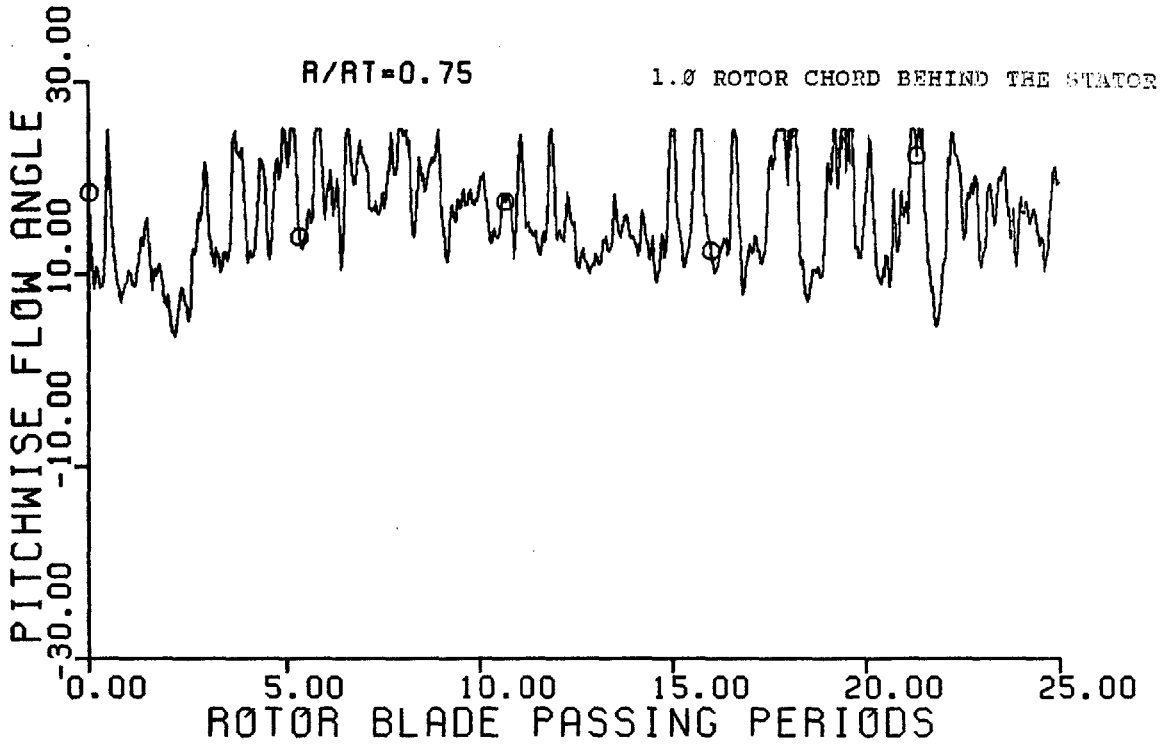

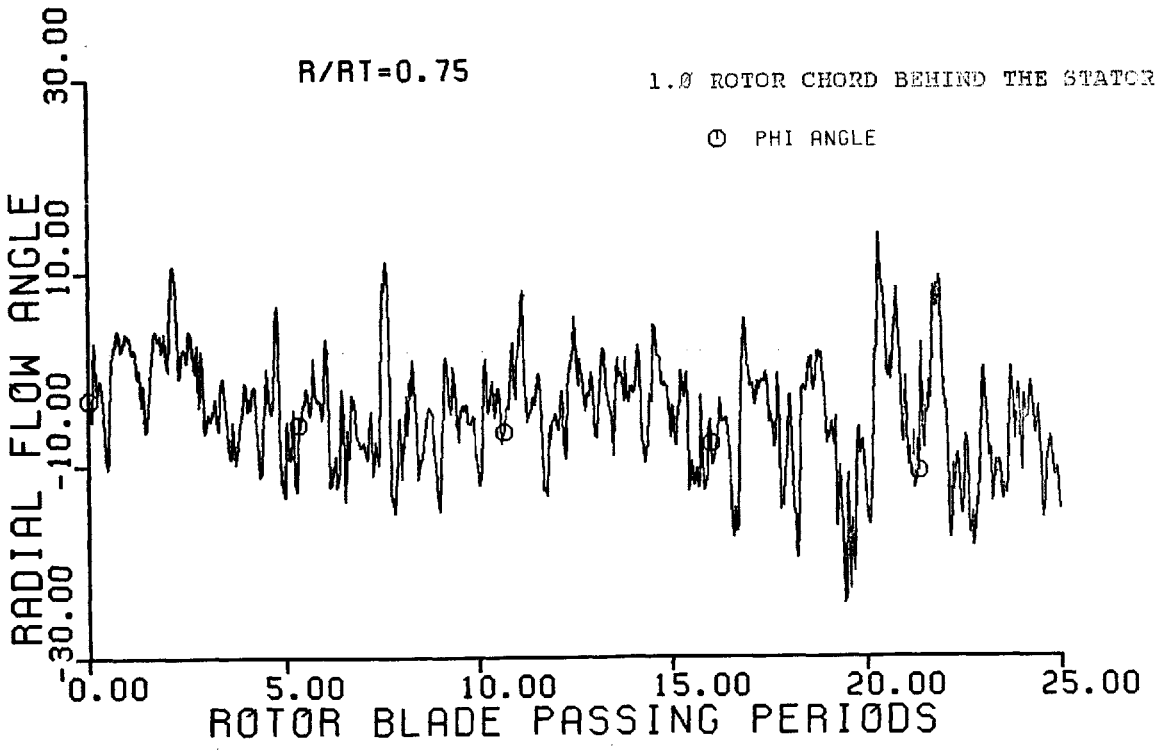

FIG. 4-19 Tangential and Radial Flow Angles 1.0 Rotor Chord Downstream of the Stator, R/RT = 0.75

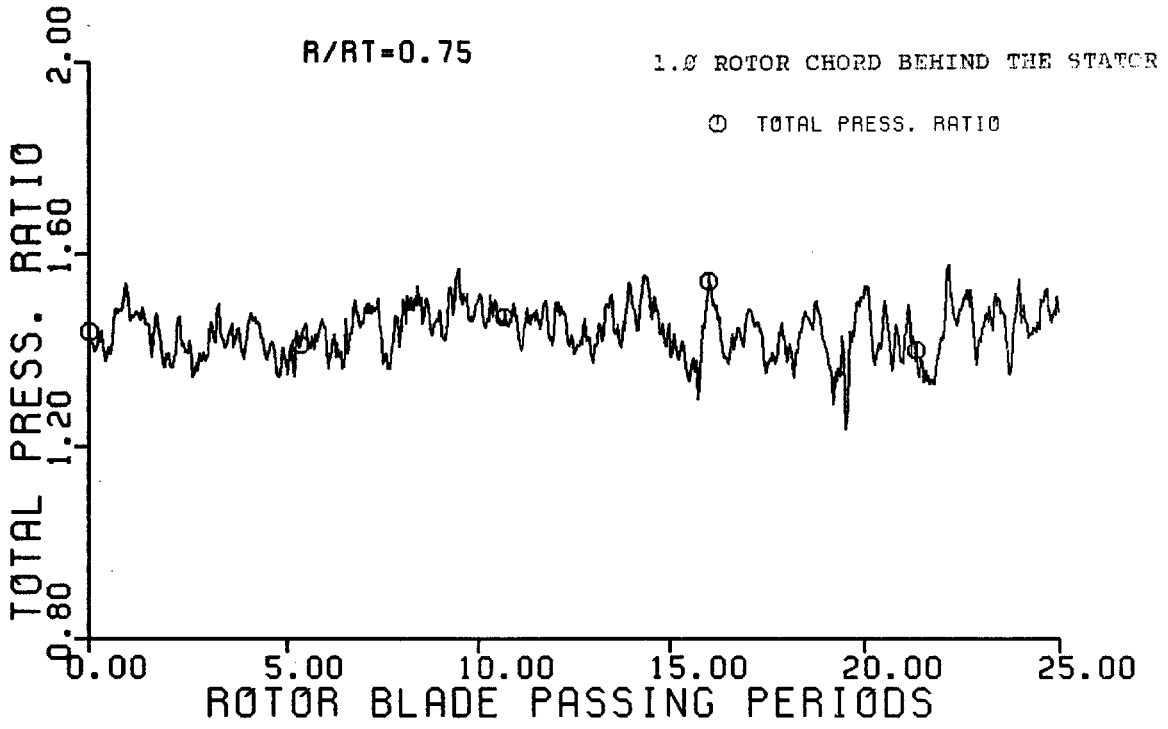

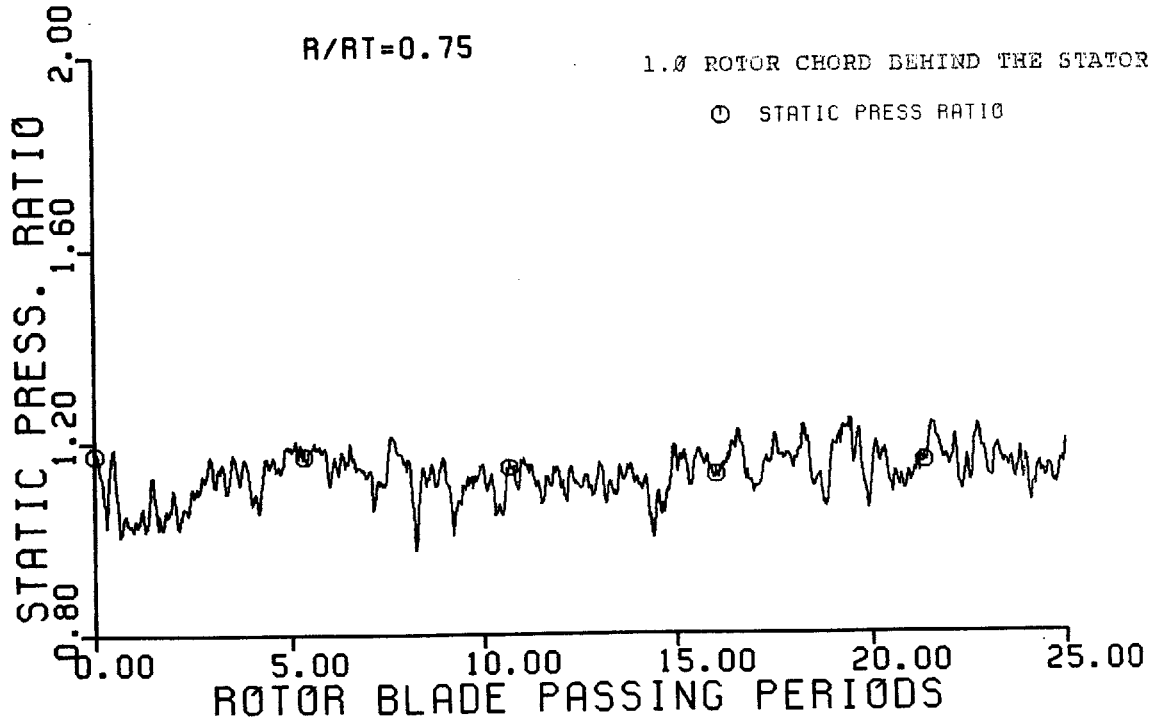

FIG. 4-20 Total and Static Pressure Ratios 1.0 Rotor Chord Downstream of the Stator, R/R = 0.75

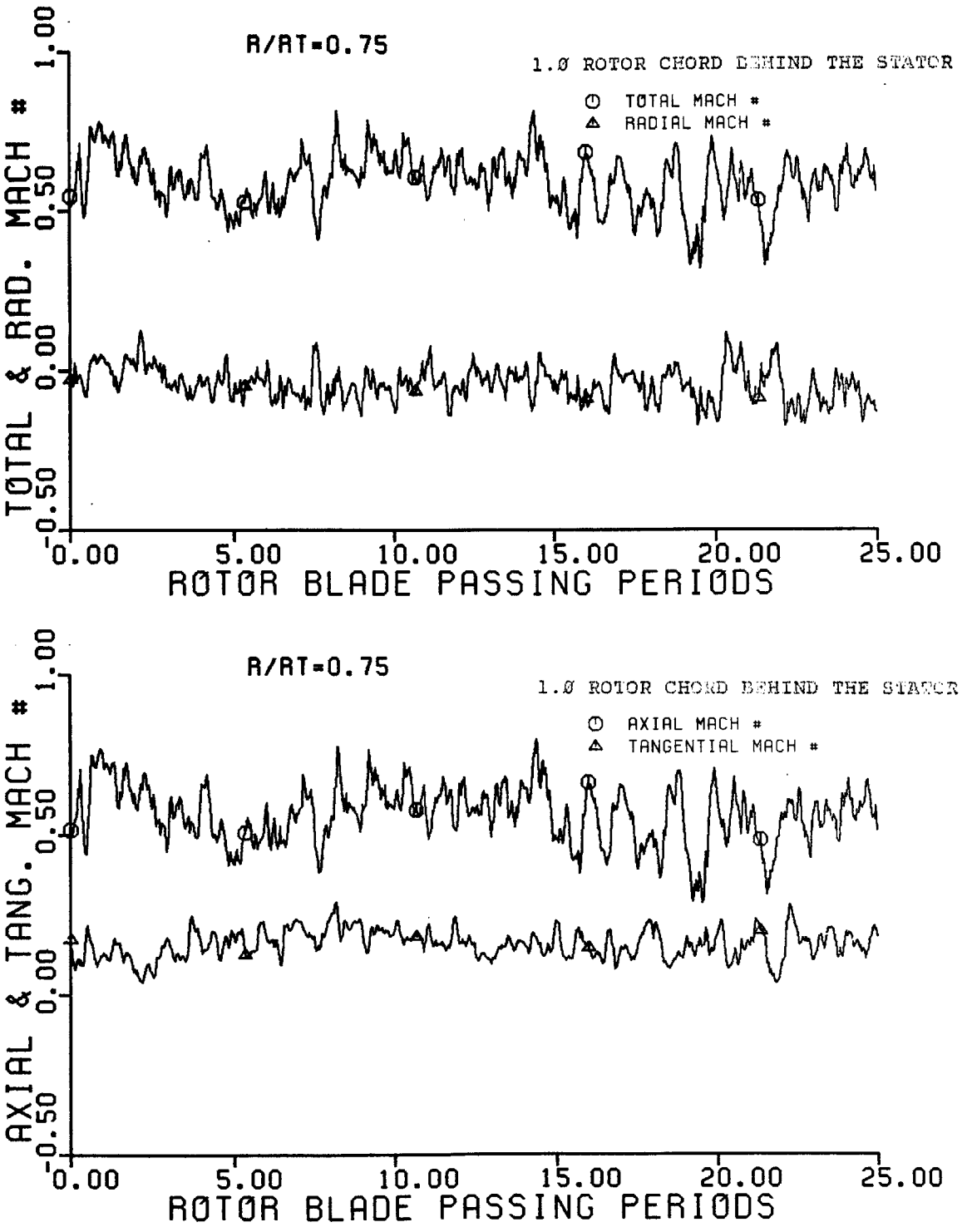

FIG. 4-21 Flow Mach Numbers 1.0 Rotor Chord Downstream of the Stator, $R/R_T = 0.75$

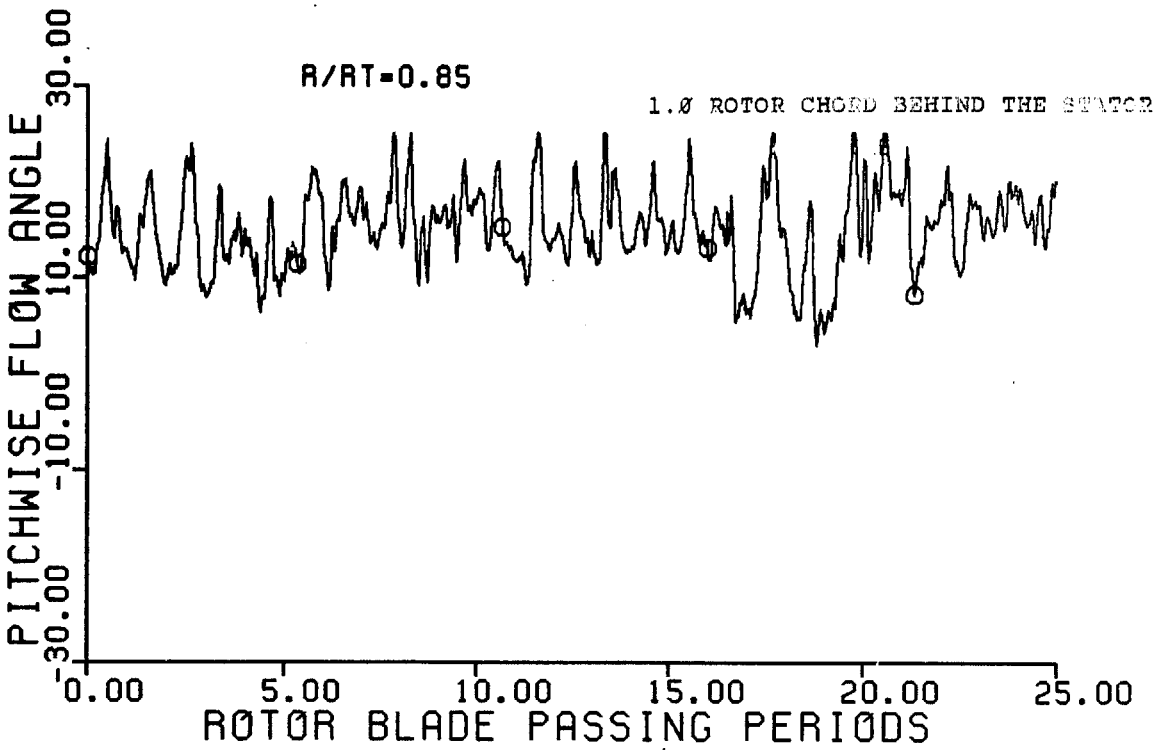

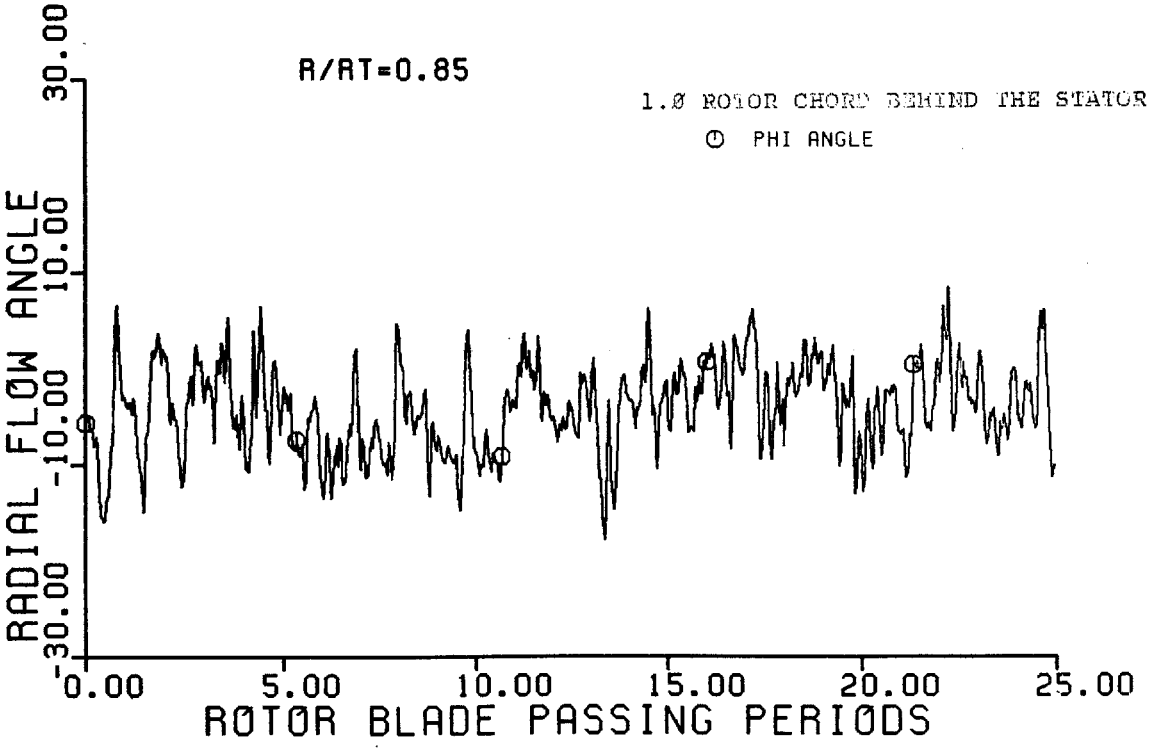

FIG. 4-22 Tangential and Radial Flow Angles 1.0 Rotor Chord Downstream of the Stator, $R/R_T = 0.85$

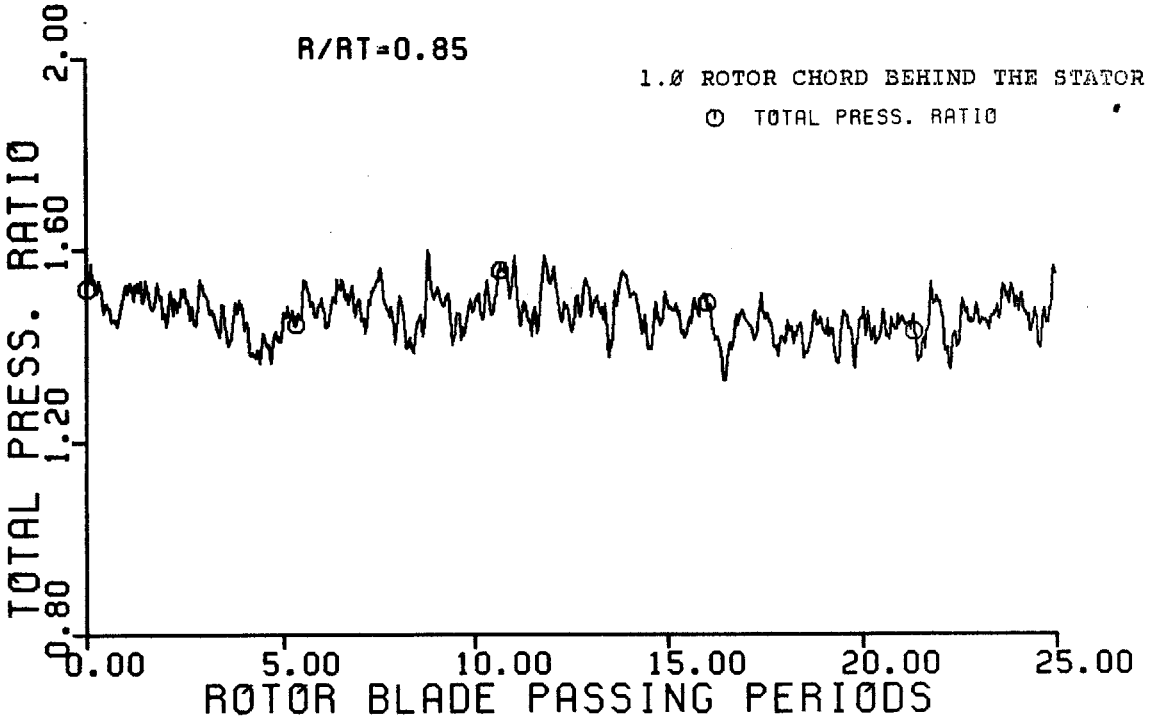

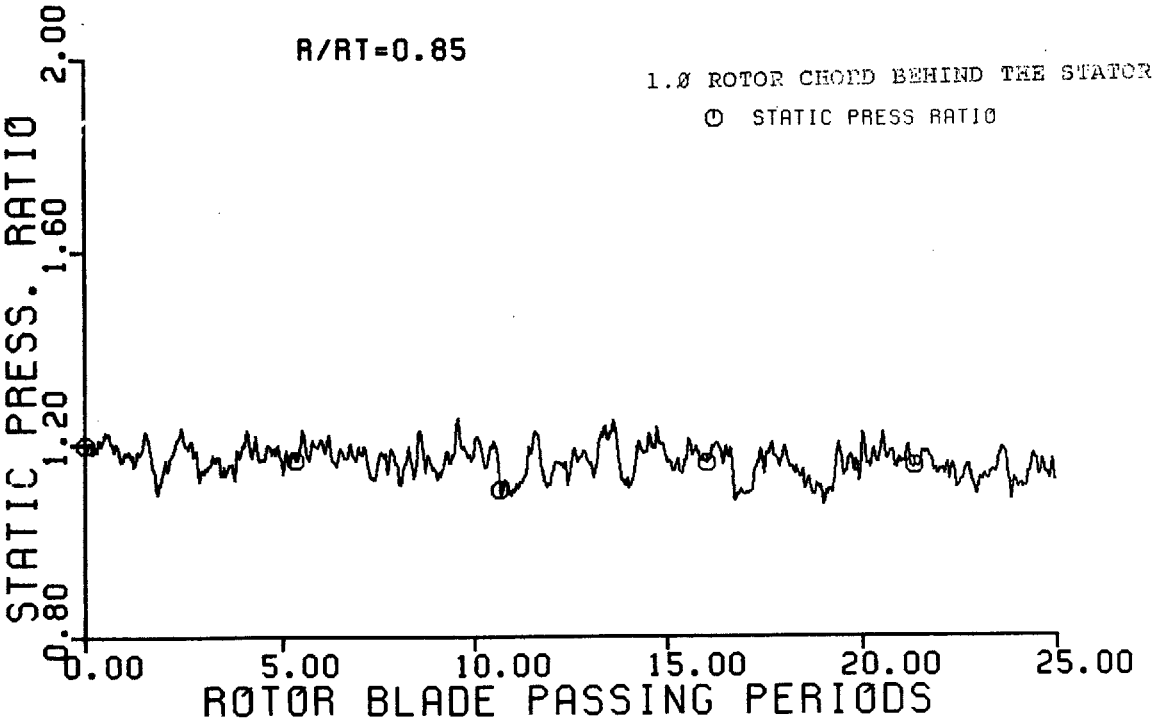

FIG. 4-23 Total and Static Pressure Ratios 1.0 Rotor Chord Downstream of the Stator, R/R = 0.85

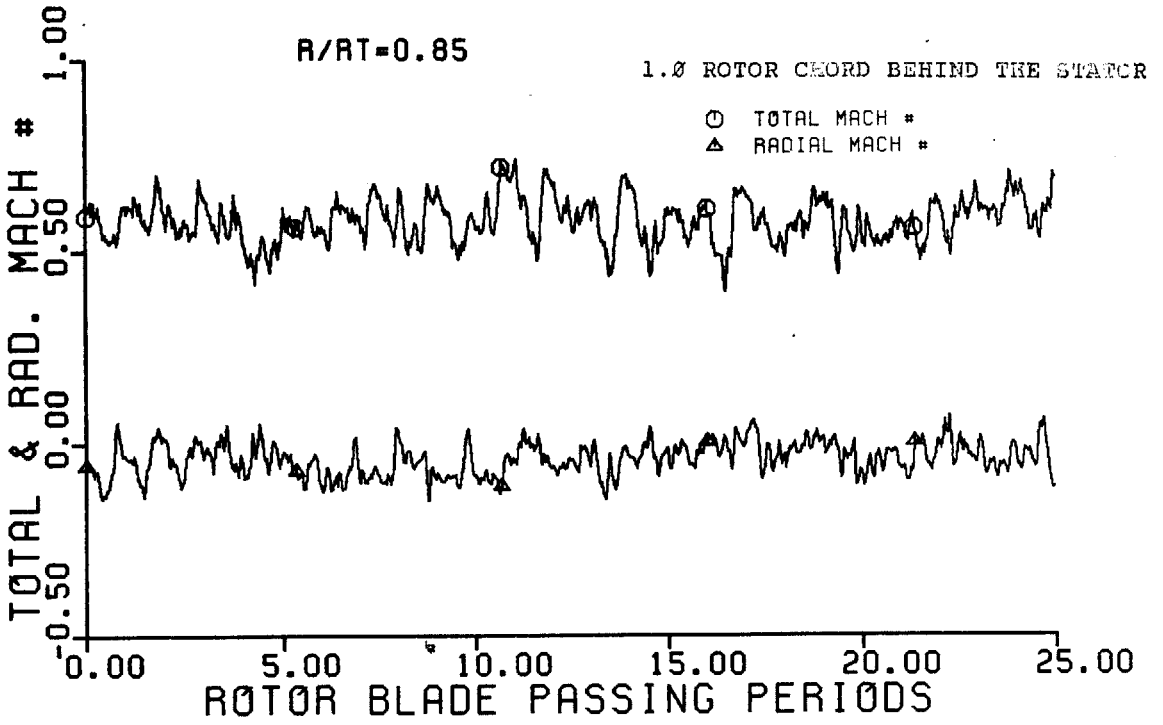

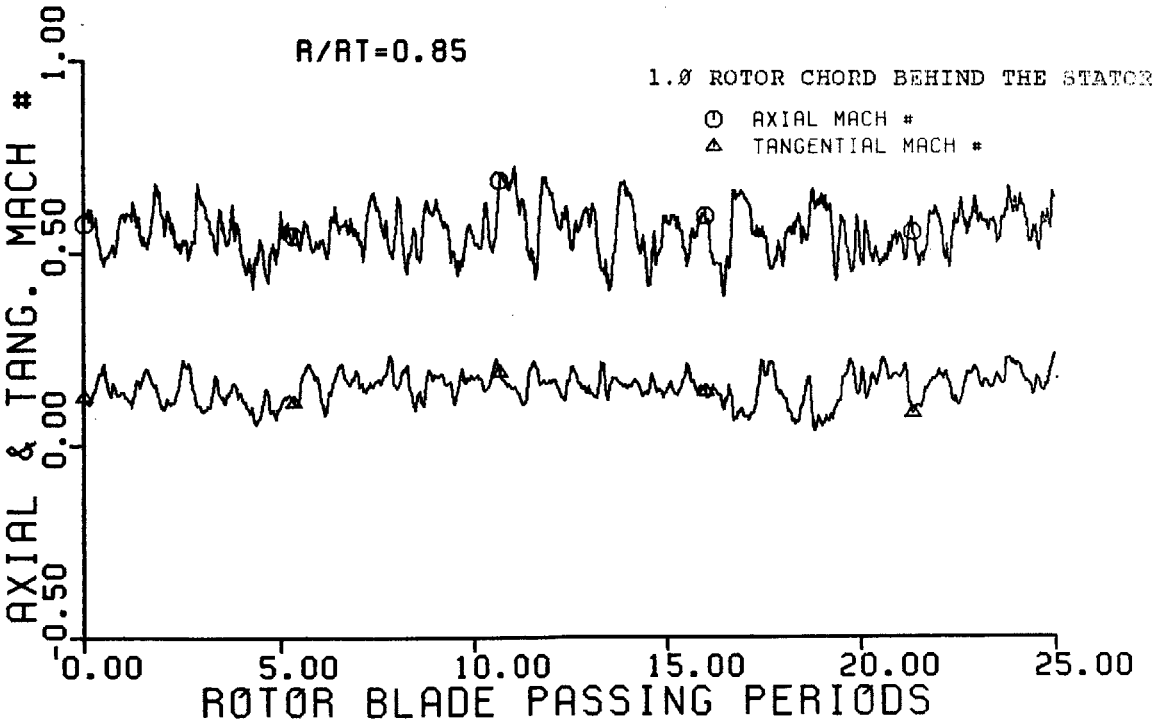

FIG. 4-24 Flow Mach Numbers 1.0 Rotor Chord Downstream of the Stator, $R/R_T = 0.85$

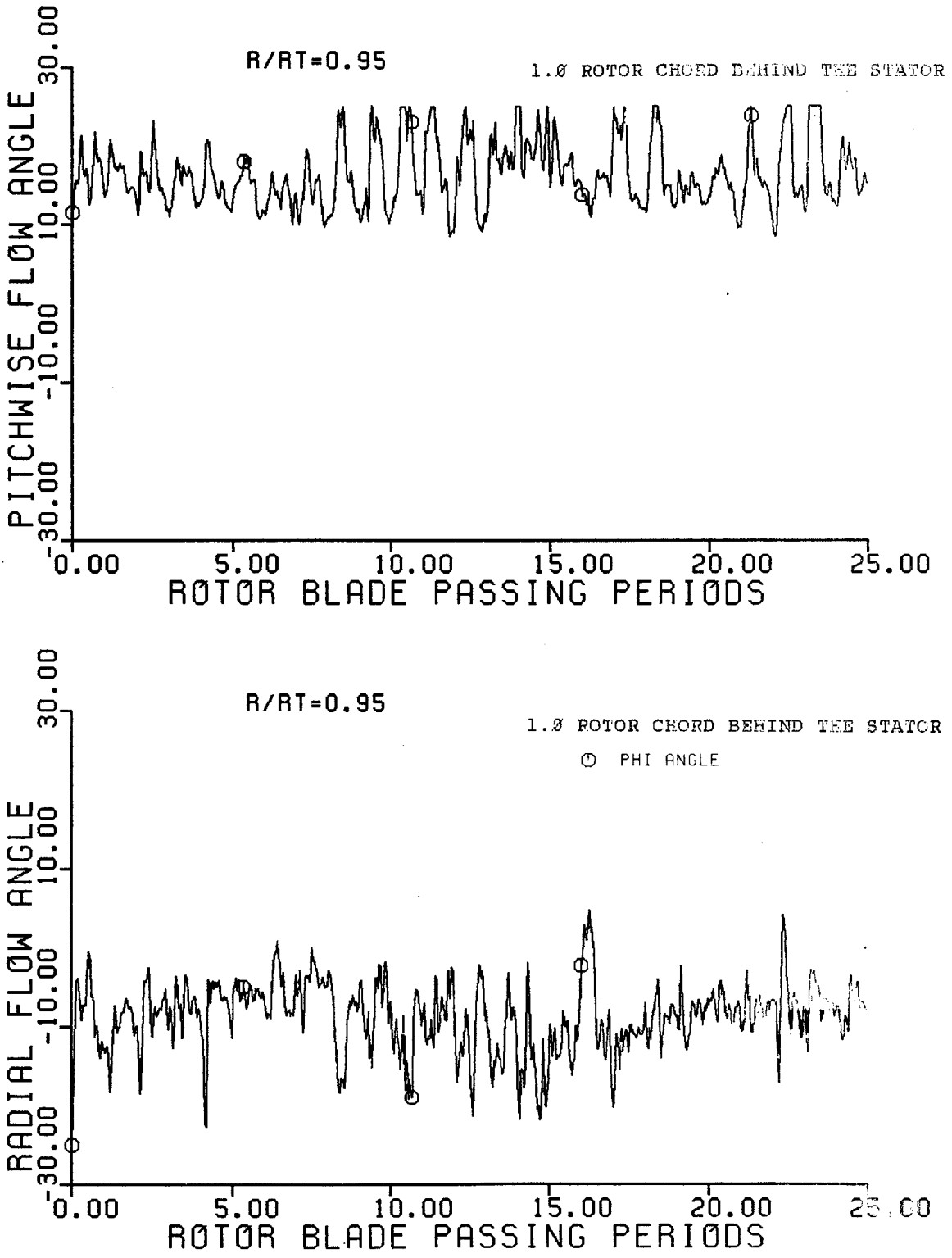

FIG. 4-25 Tangential and Radial Flow Angles 1.0 Rotor Chord Downstream of the Stator, $R/R_T = 0.95$

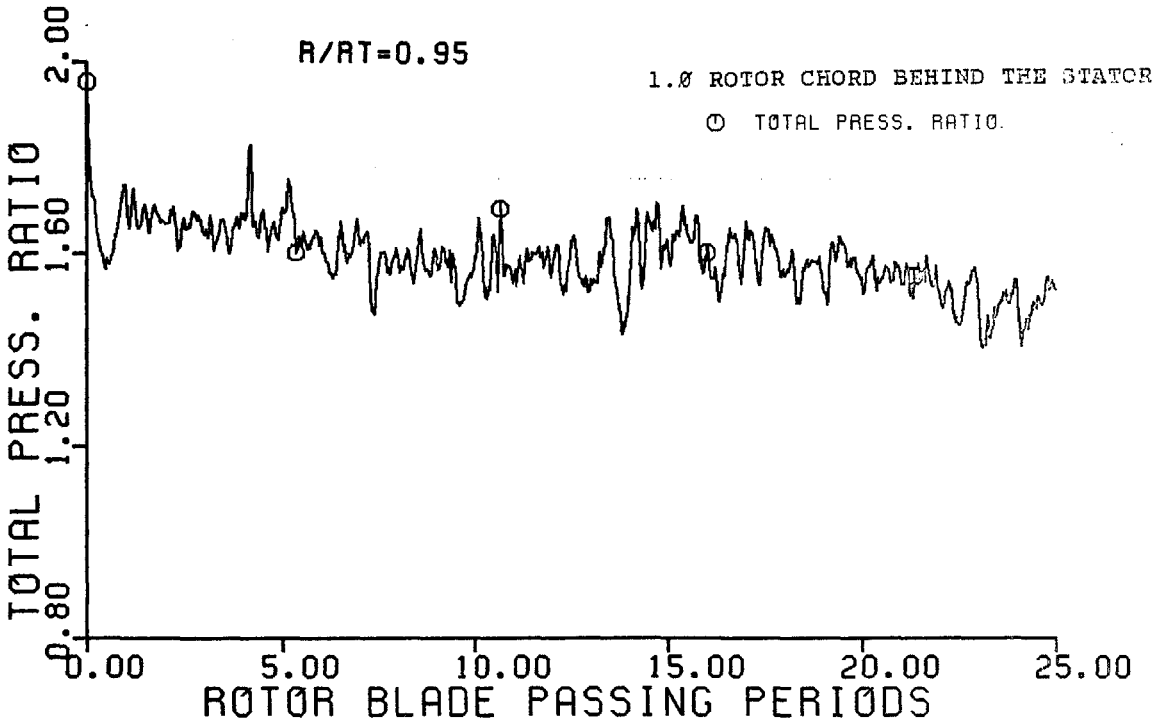

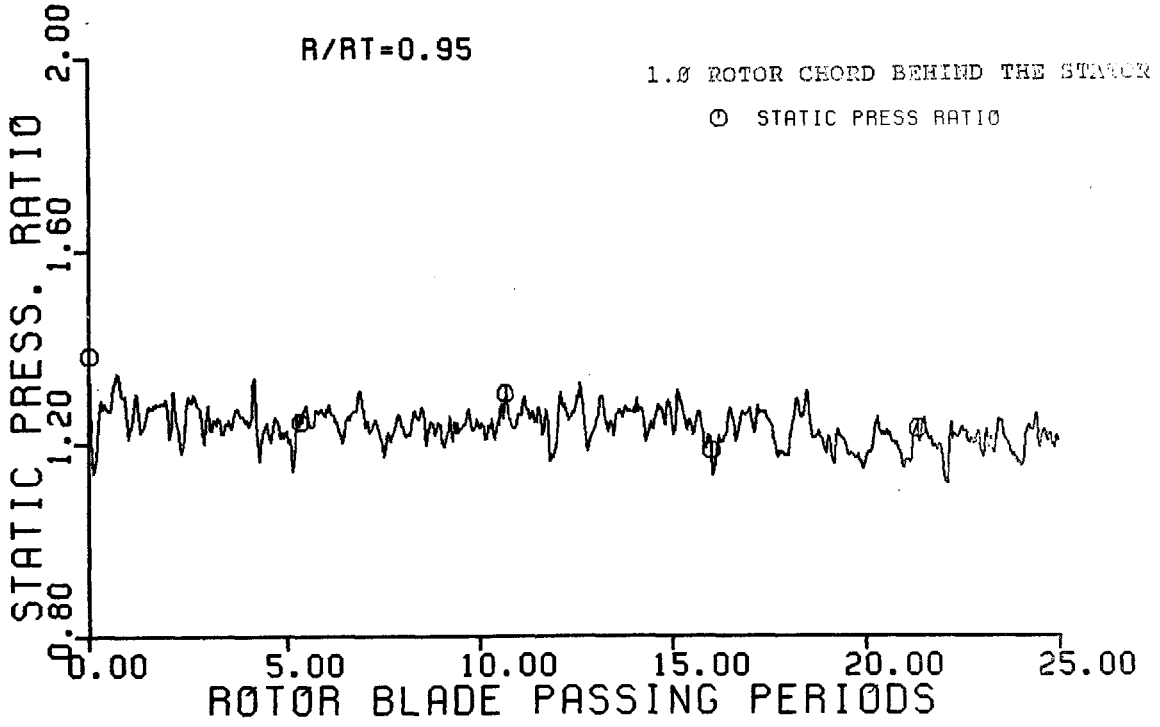

FIG. 4-26 Total and Static Pressure Ratios 1.0 Rotor Chord Downstream of the Stator, R/R = 0.95

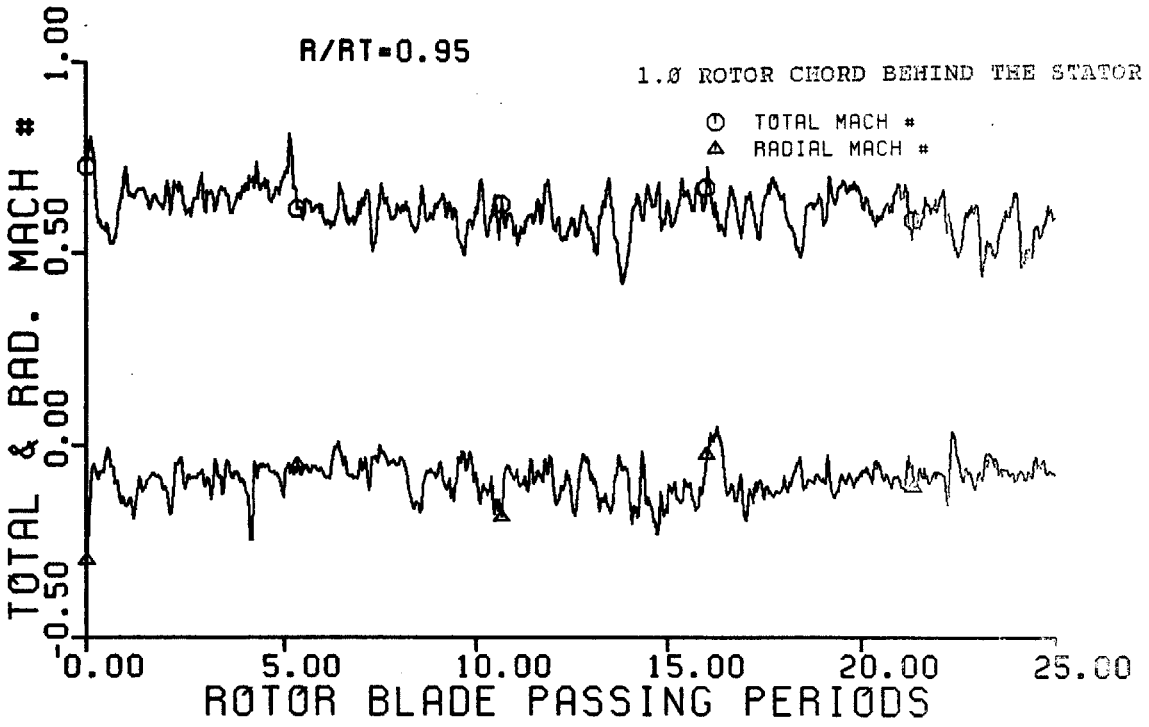

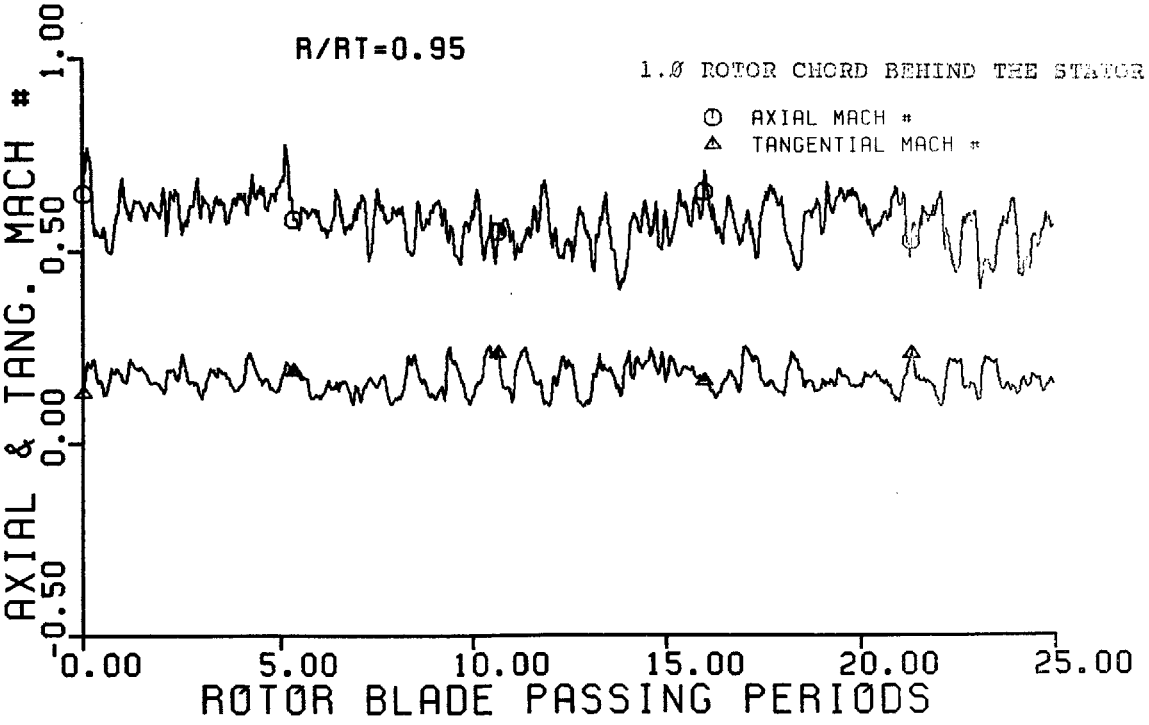

FIG. 4-27 Flow Mach Numbers 1.0 Rotor Chord Downstream of the Stator, $R/R_T = 0.95$

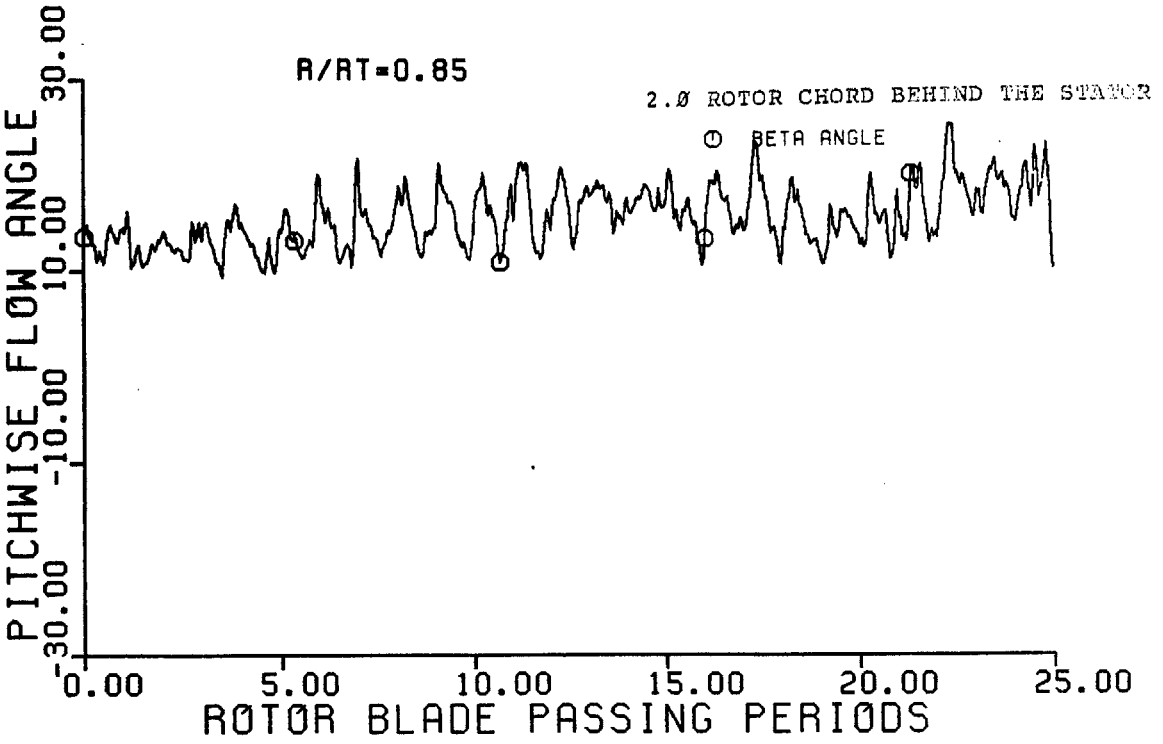

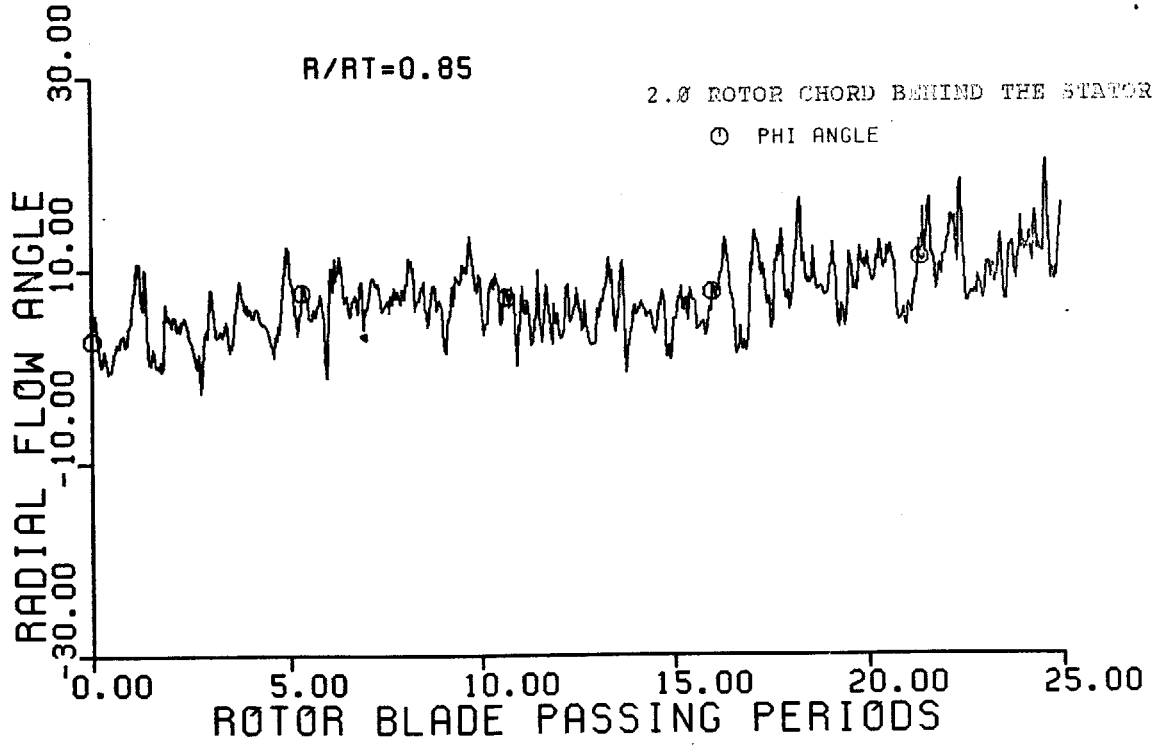

FIG. 4-28 Tangential & Radial Flow Angles
2.0 Rotor Chords Downstream of the
Stator, R/R_T = 0.85

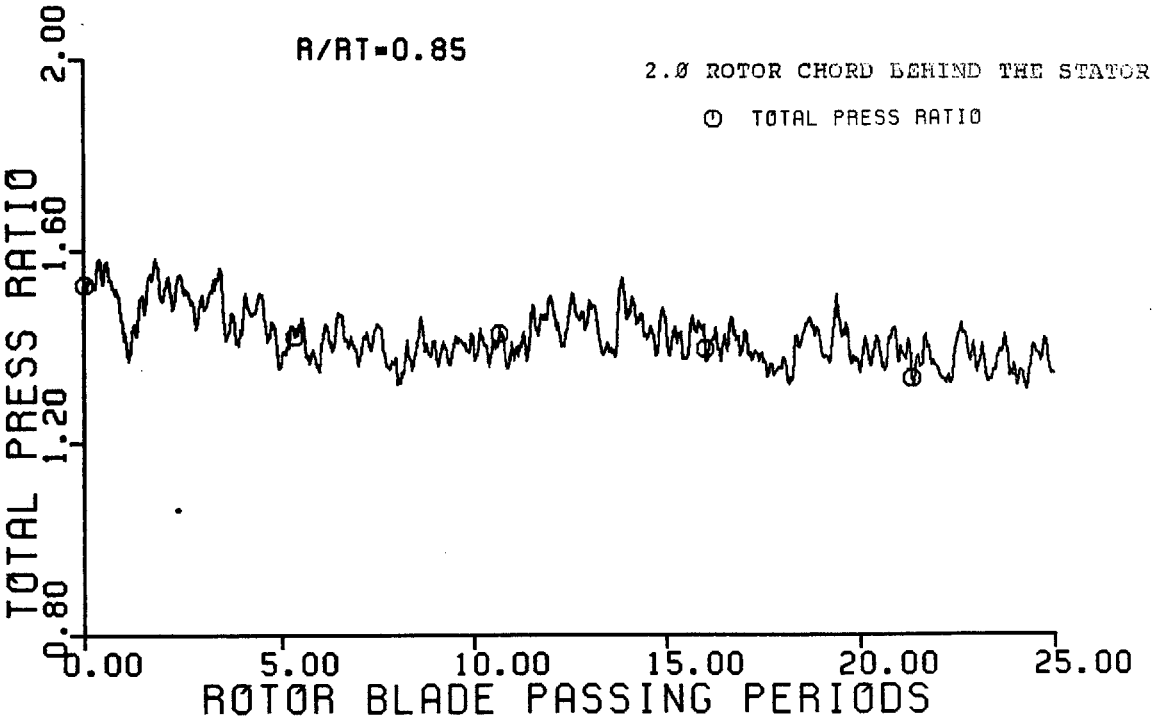

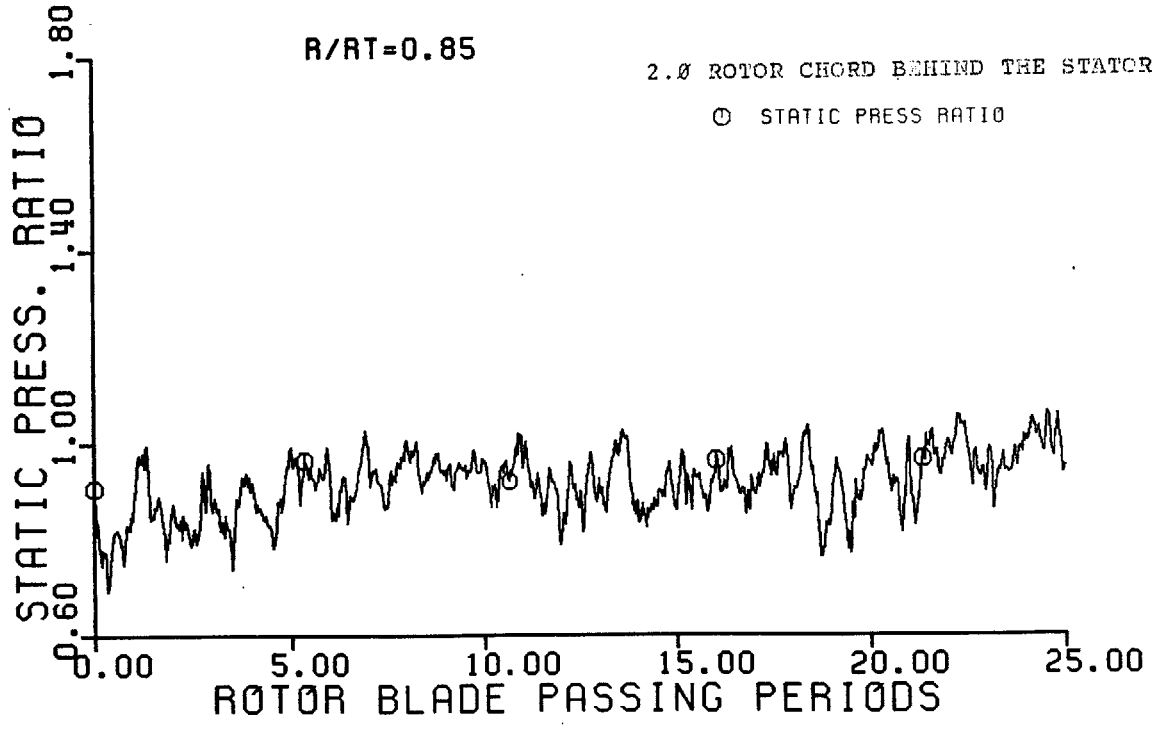

FIG. 4-29 Total & Static Pressure Ratios 2.0 Rotor Chords Downstream of the Stator, R/R_T = 0.85

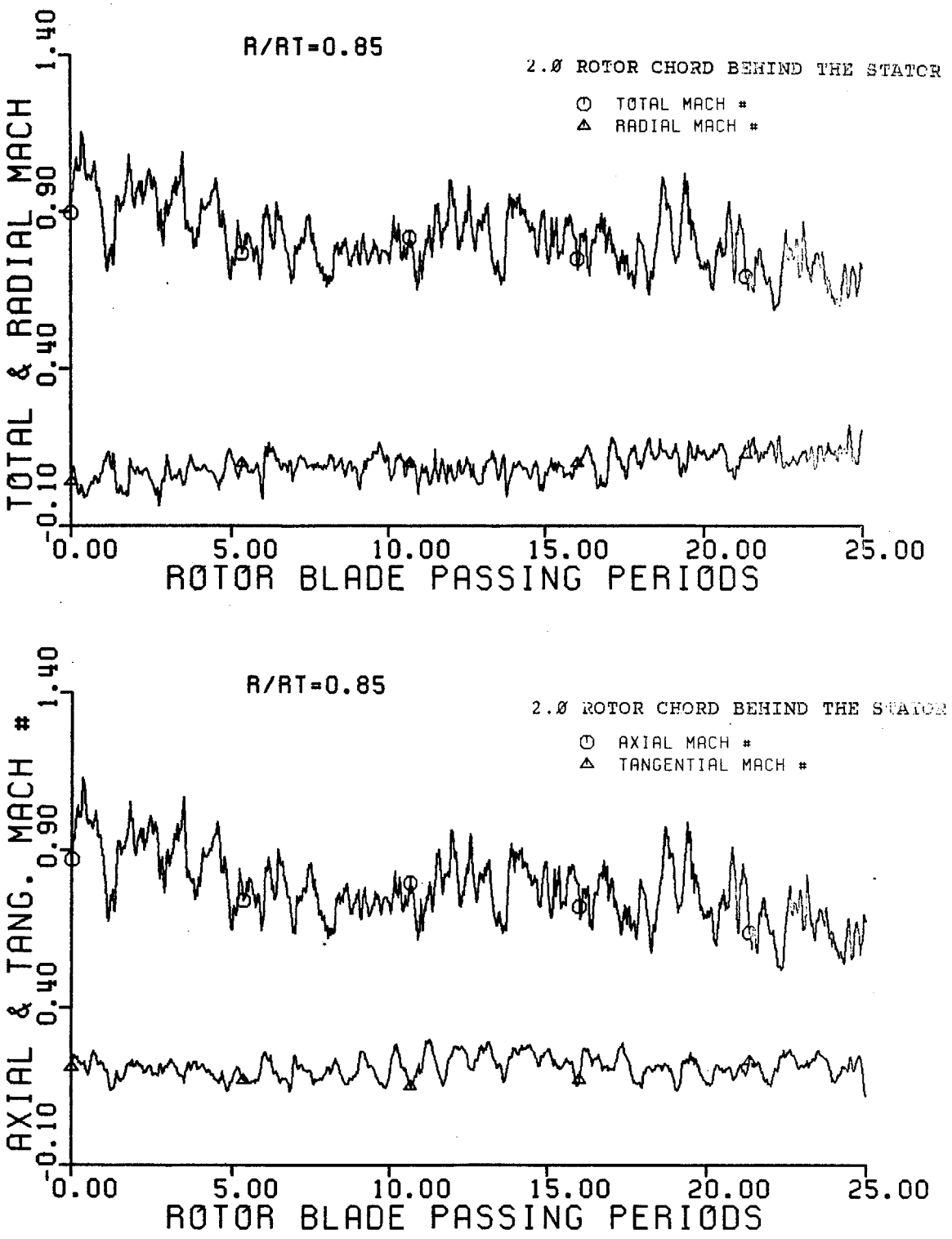

FIG. 4-30 Flow Mach Numbers 2.0 Rotor Chords Downstream of the Stator, $R/R_T = 0.85$

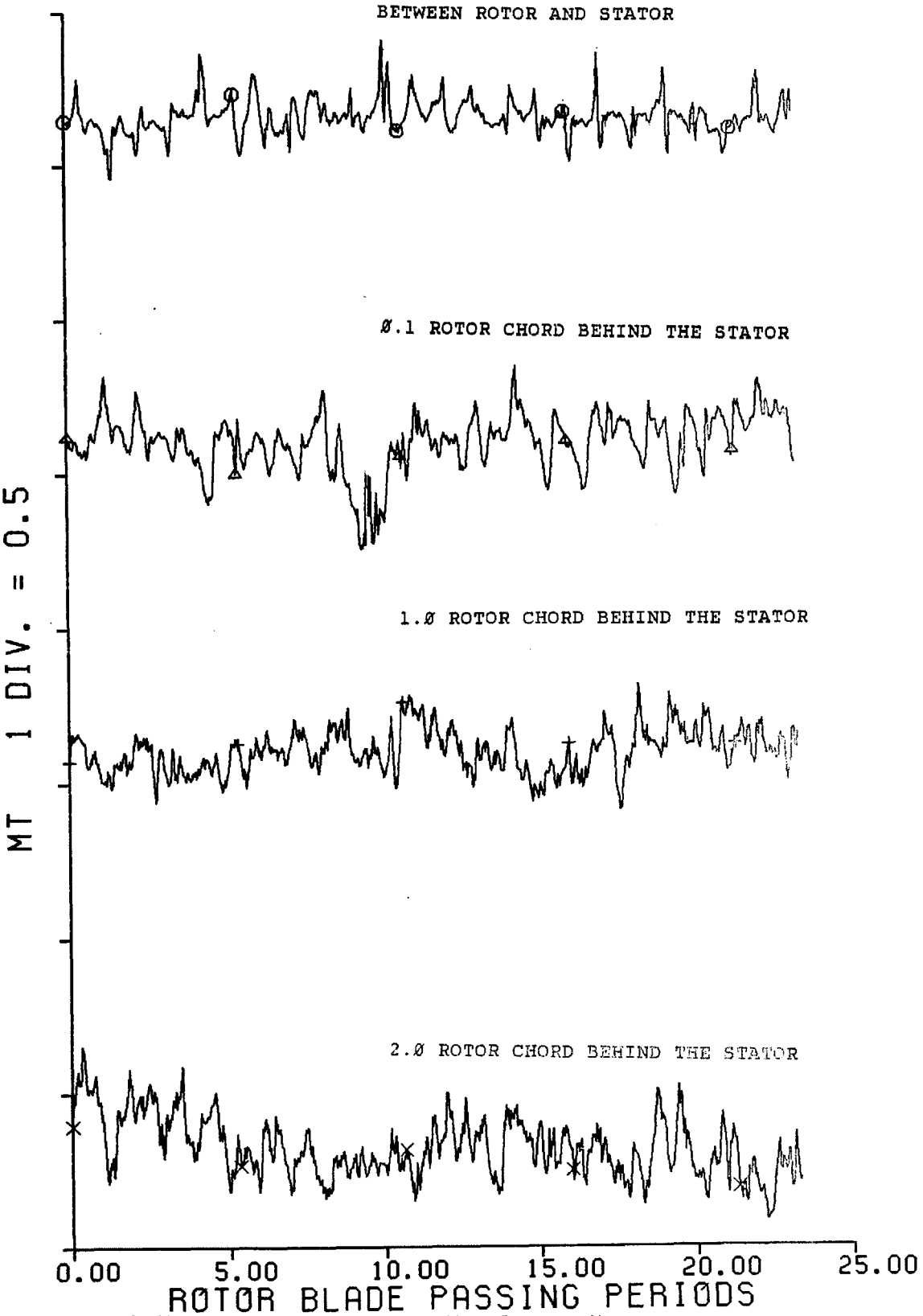

FIG. 4-31 Comparison Between Total Mach No. as Measured at Different Axial Locations in the Stage, $R/R_T = 0.85$

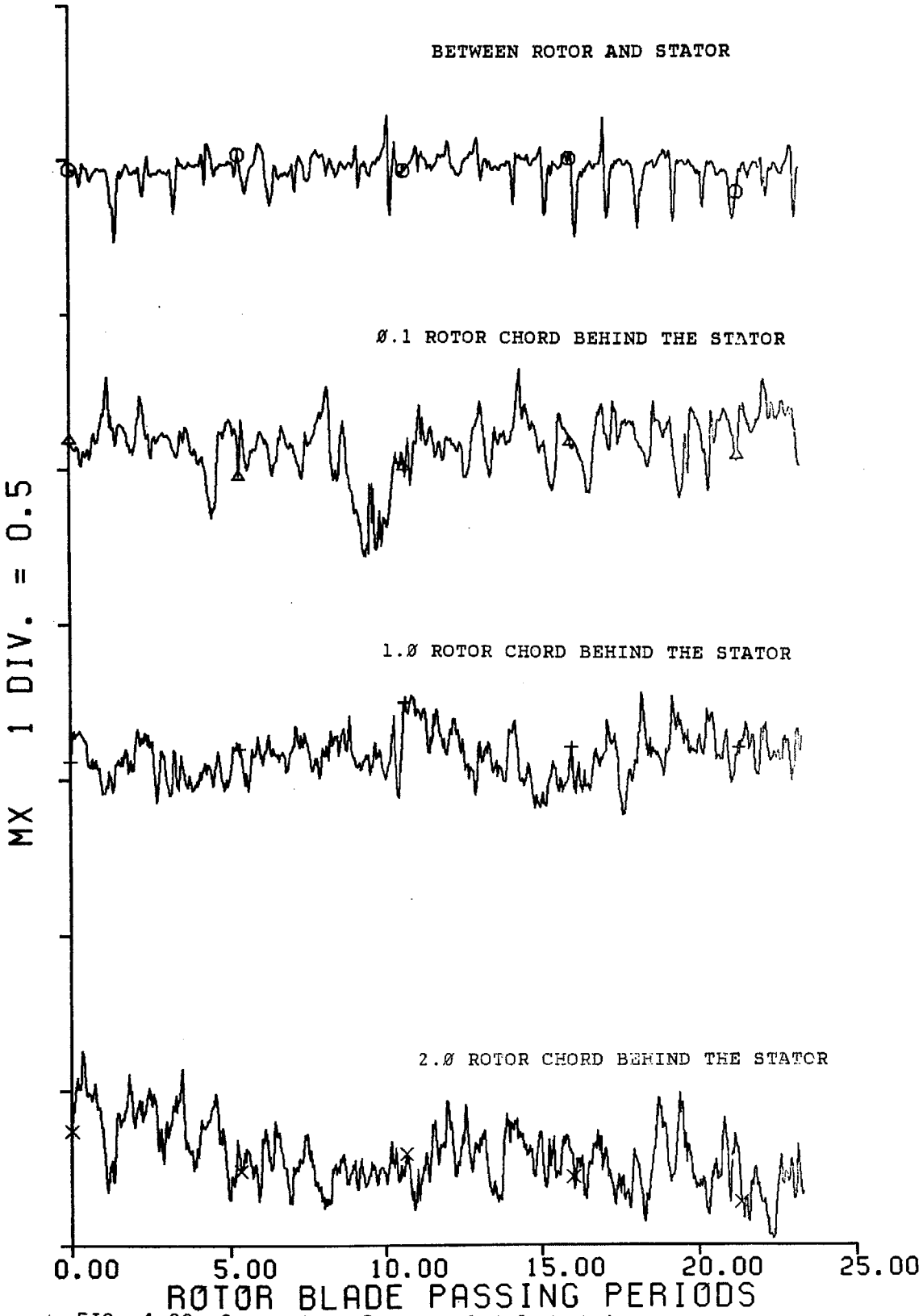

FIG. 4-32 Comparison Between Axial Mach No. as Measured at Different Axial Locations in the Stage, $R/R_T = 0.85$

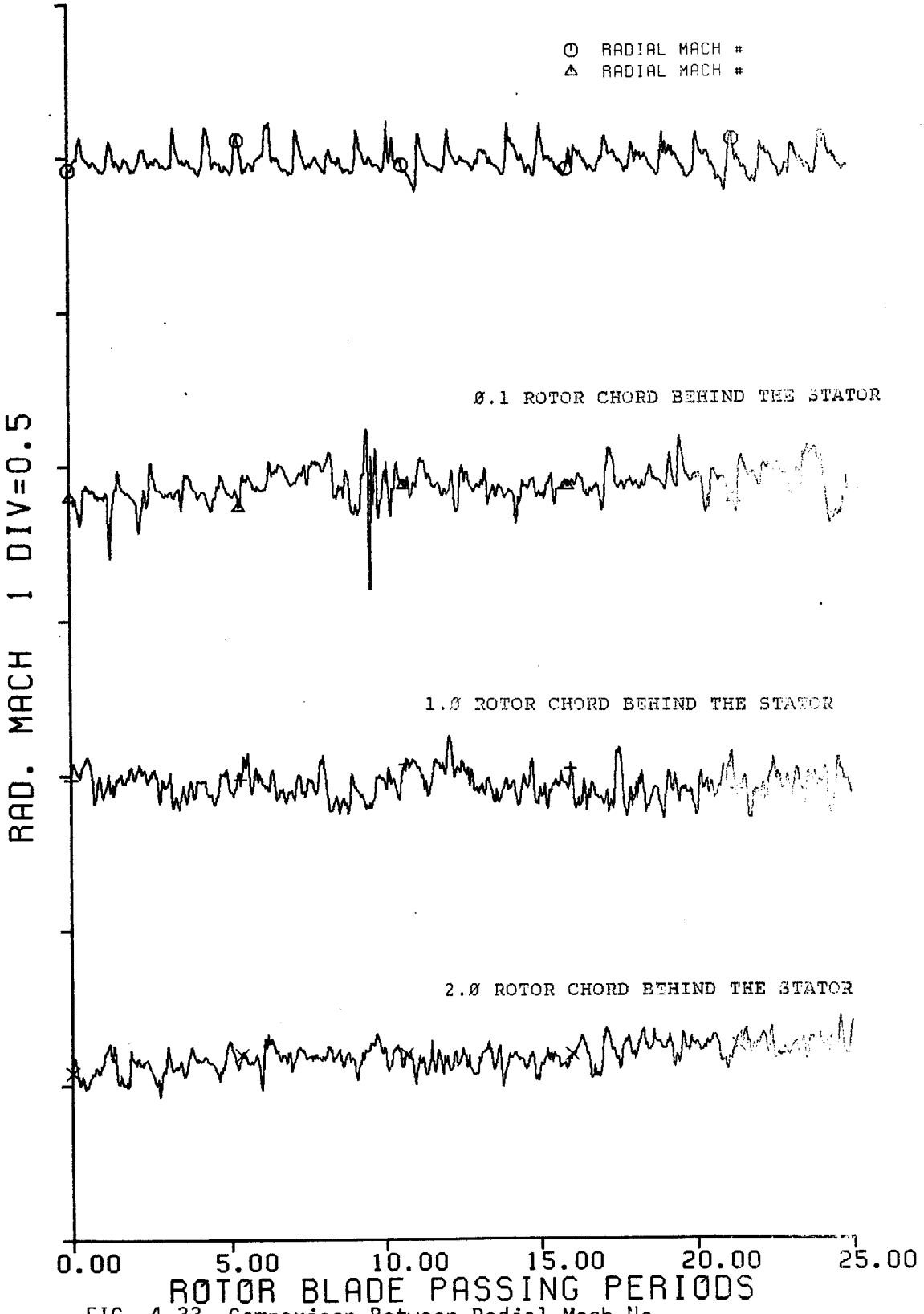

FIG. 4-33 Comparison Between Radial Mach No. as Measured at Different Axial Locations in the Stage, $R/R_T = 0.85$

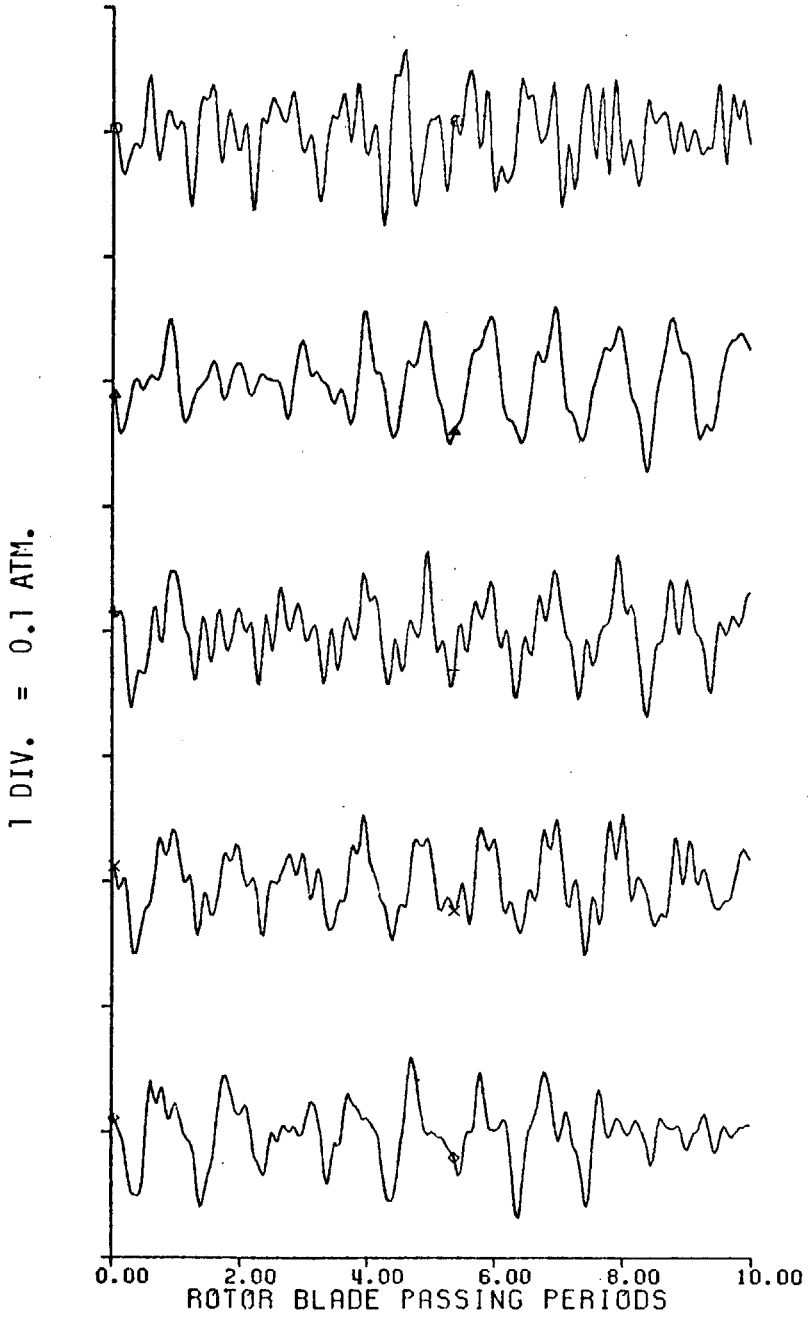

FIG. 4-34a Pressure Fluctuations over the Stator Blade, Pressure Side, $R/R_t = 0.72$

(from top to bottom at 20%, 35%, 50%, 65% and 80% of chord)

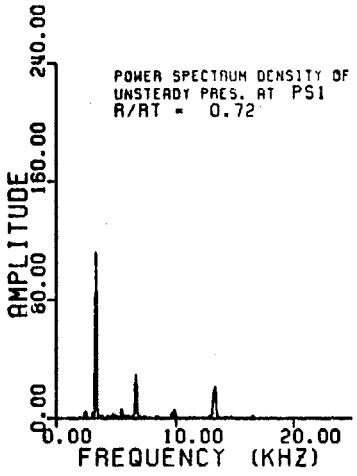

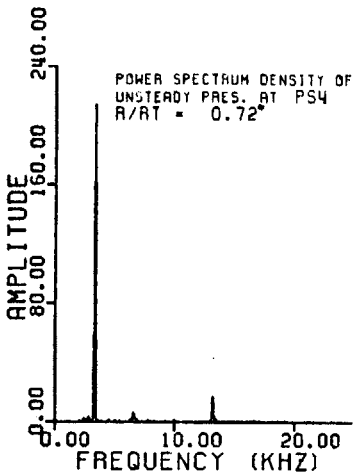

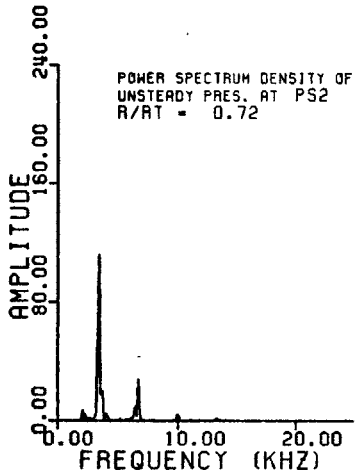

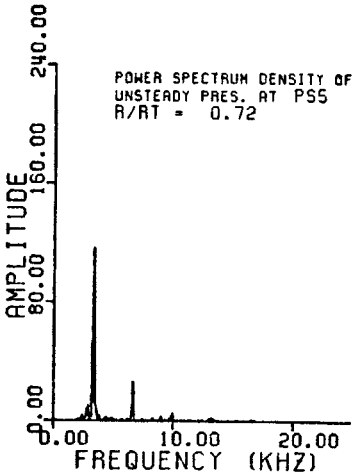

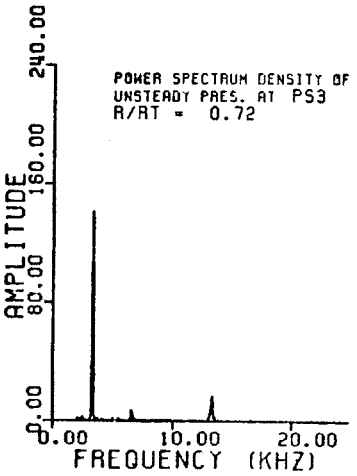

FIG. 4-34b Frequency Spectrum of Pressure Fluctuations over Stator Blade, Pressure Side, $R/R_t = 0.72$

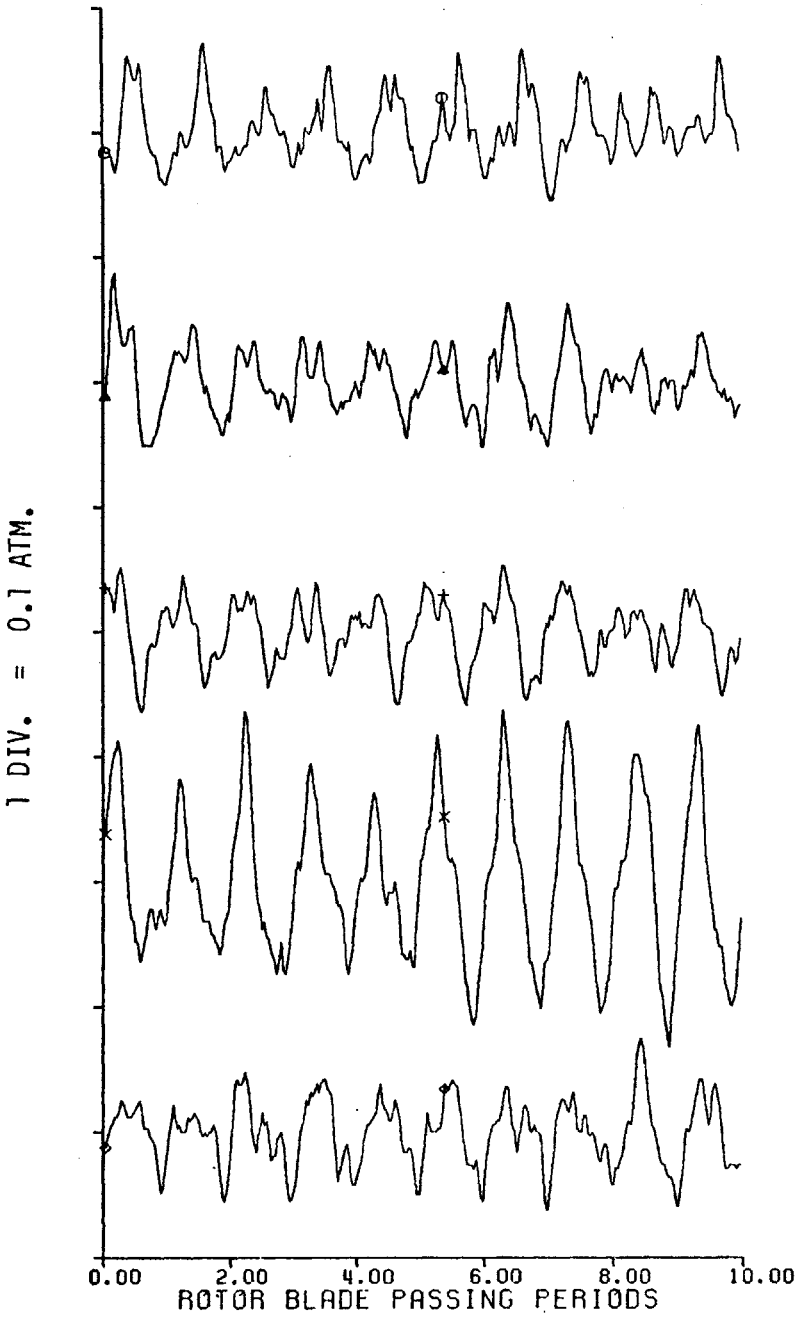

FIG. 4-35a Pressure Fluctuations over the Stator Blade, Suction Side, $R/R_t = 0.72$

(from top to bottom at 20%, 35%, 50%, 65% and 80% of chord)

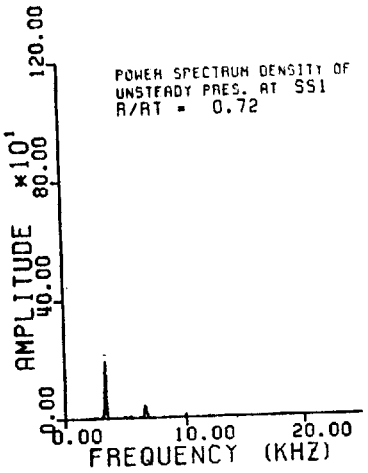

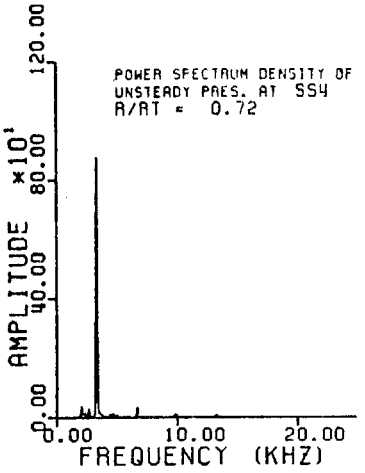

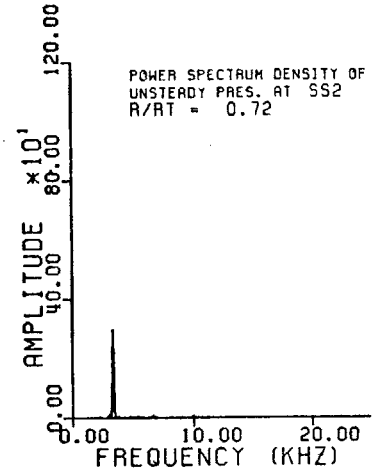

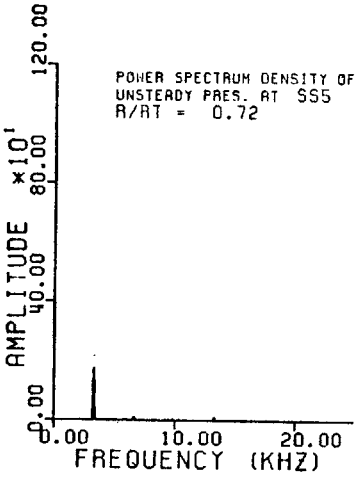

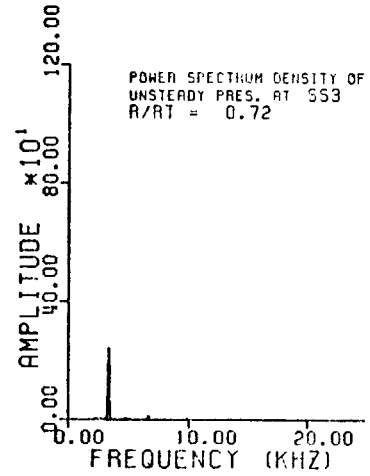

FIG. 4-35b Frequency Spectrum of Pressure Fluctuations over Stator Blade, Suction Side, $R/R_t = 0.72$

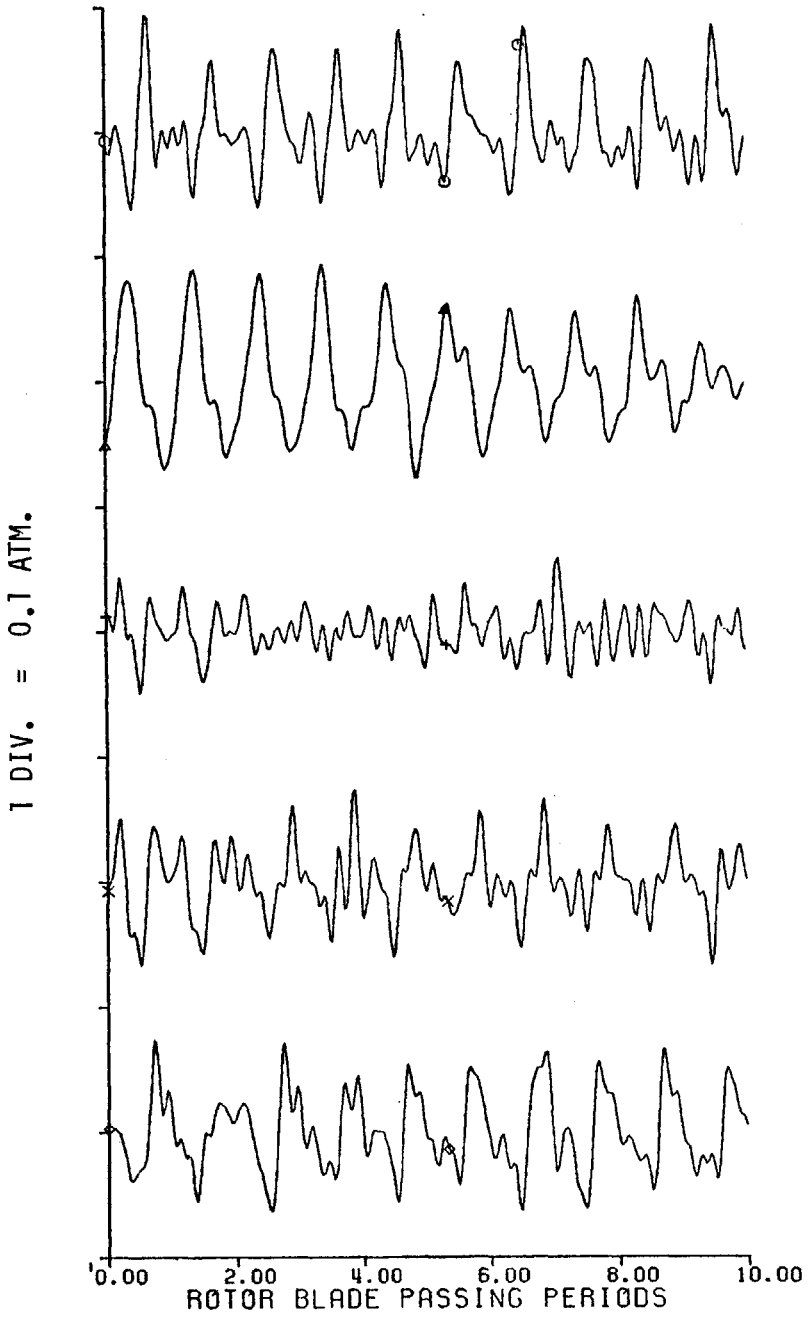

FIG. 4-36a Pressure Fluctuations over the Stator Blade, Pressure Side, $R/R_t = 0.82$

(from top to bottom at 20%, 35%, 50%, 65% and 80% of chord)

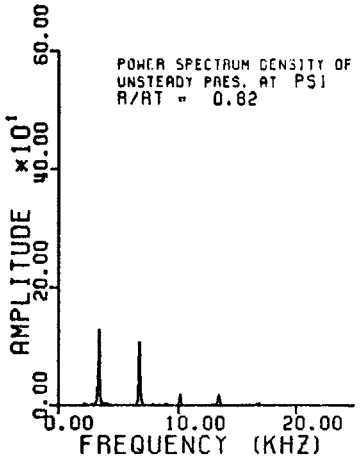

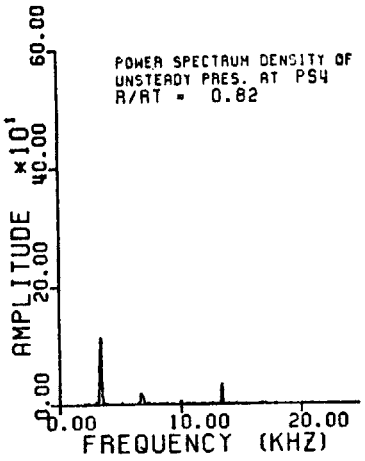

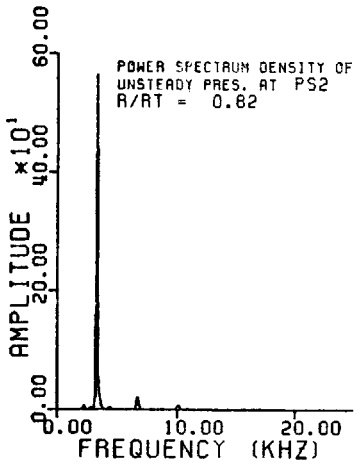

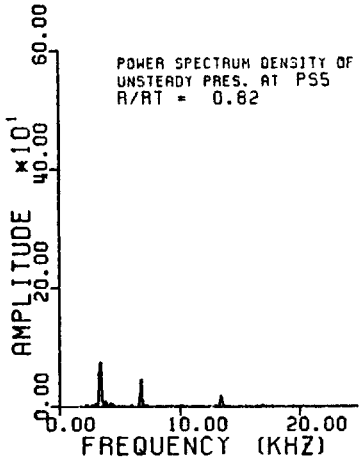

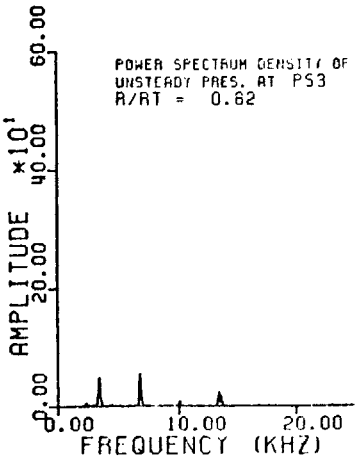

FIG. 4-36b Frequency Spectrum of Pressure Fluctuations over Stator Blade, Pressure Side, $R/R_t = 0.82$

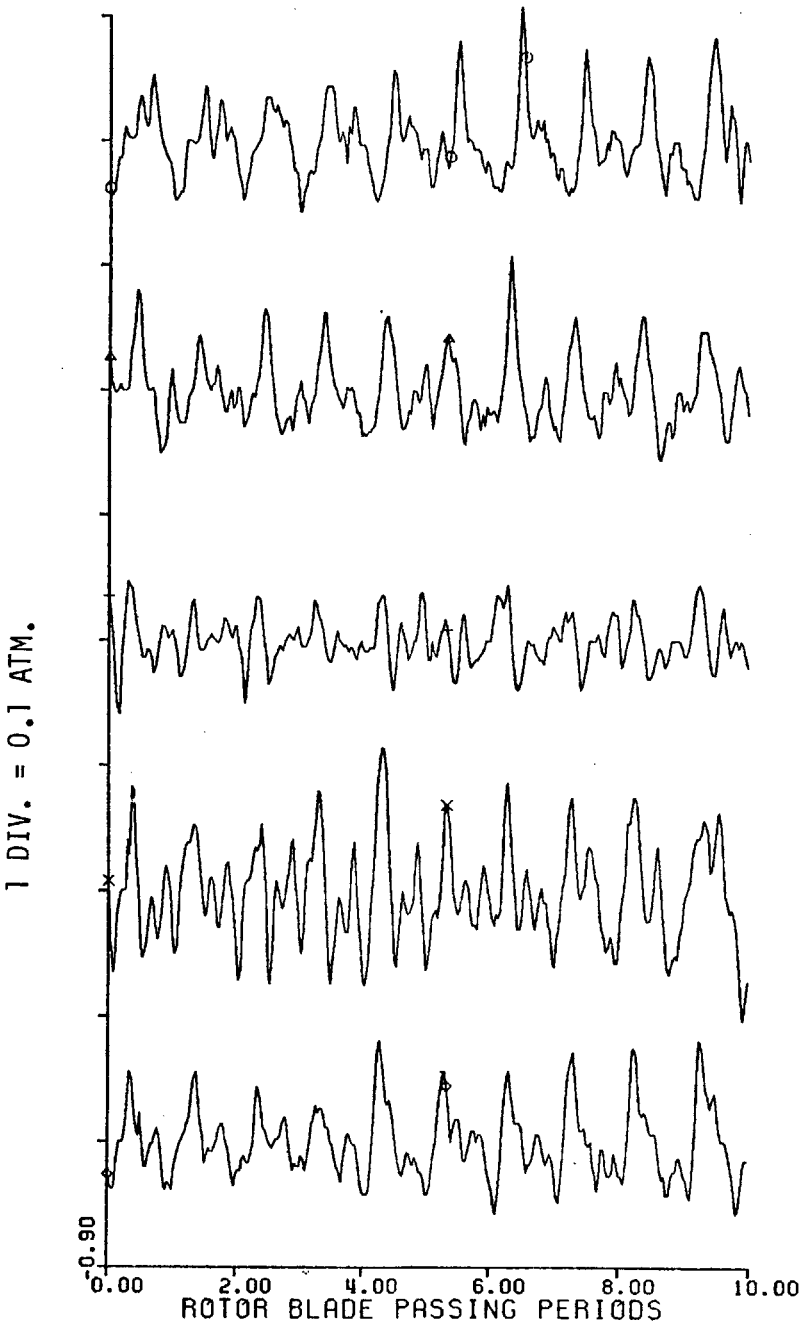

FIG. 4-37a Pressure Fluctuations over the Stator Blade, Suction Side, $R/R_t = 0.82$

(from top to bottom at 20%, 35%, 50%, 65% and 80% of Chord)

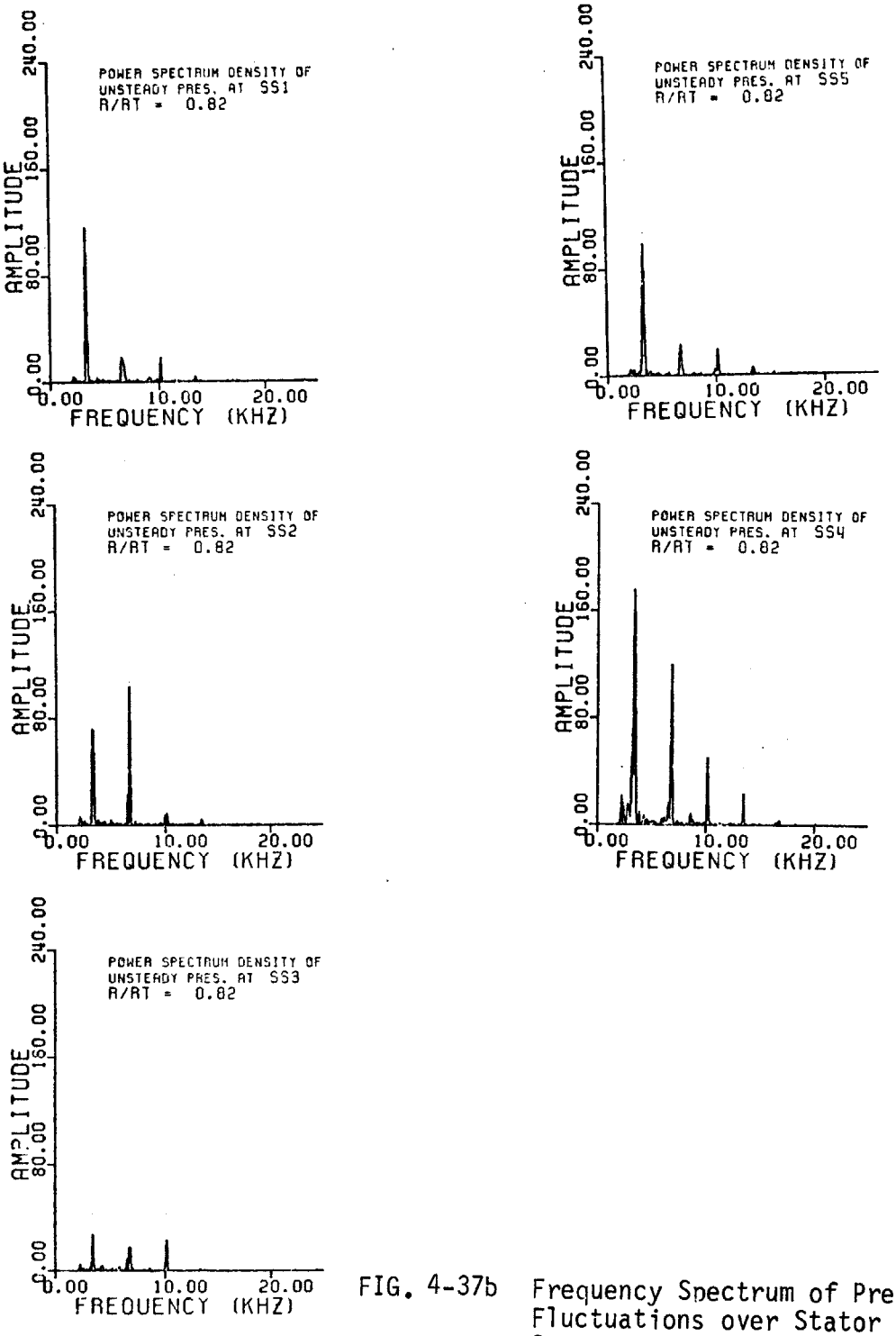

FIG. 4-37b Frequency Spectrum of Pressure Fluctuations over Stator Blade, Suction Side, $R/R_t = 0.82$

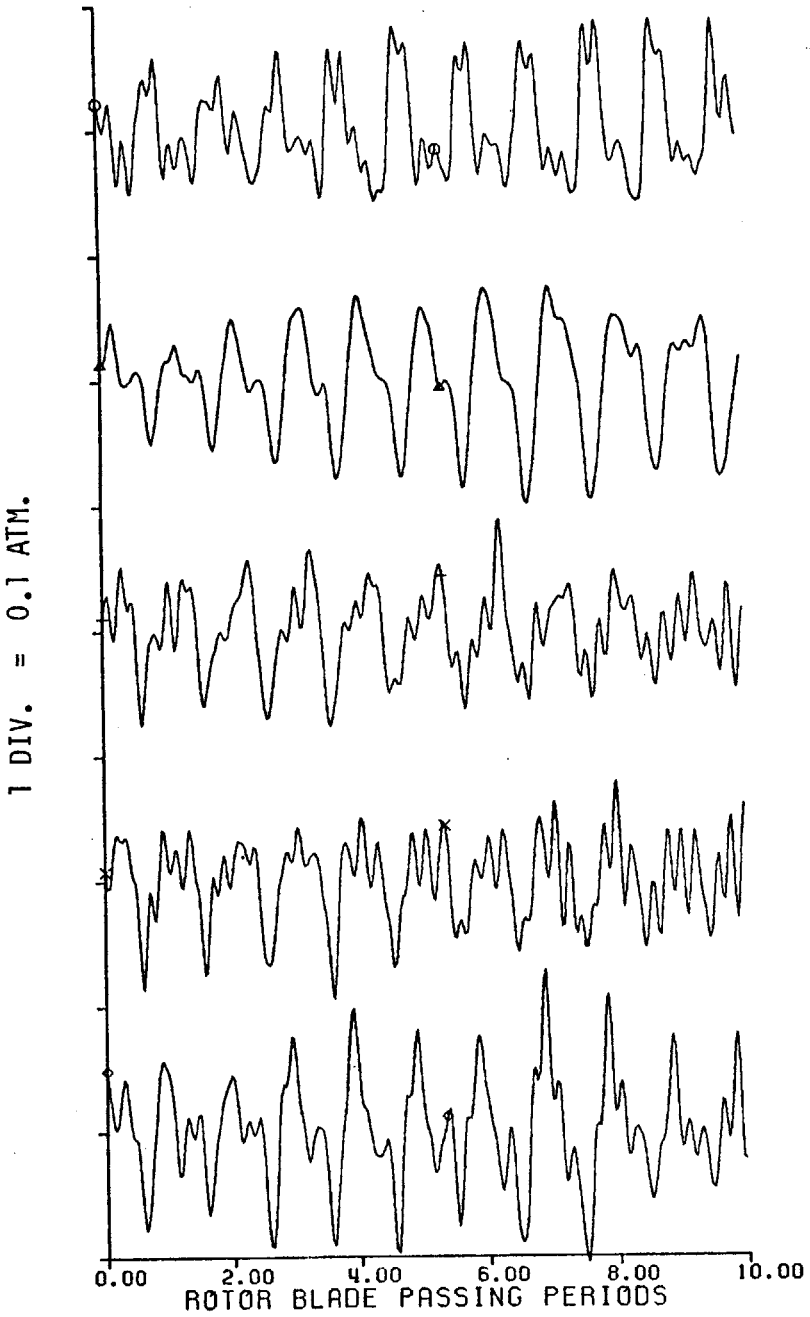

FIG. 4-38a Pressure Fluctuations over the Stator Blade, Pressure Side, $R/R_t = 0.92$

(from top to bottom at 20%, 35%, 50%, 65% and 80% of chord)

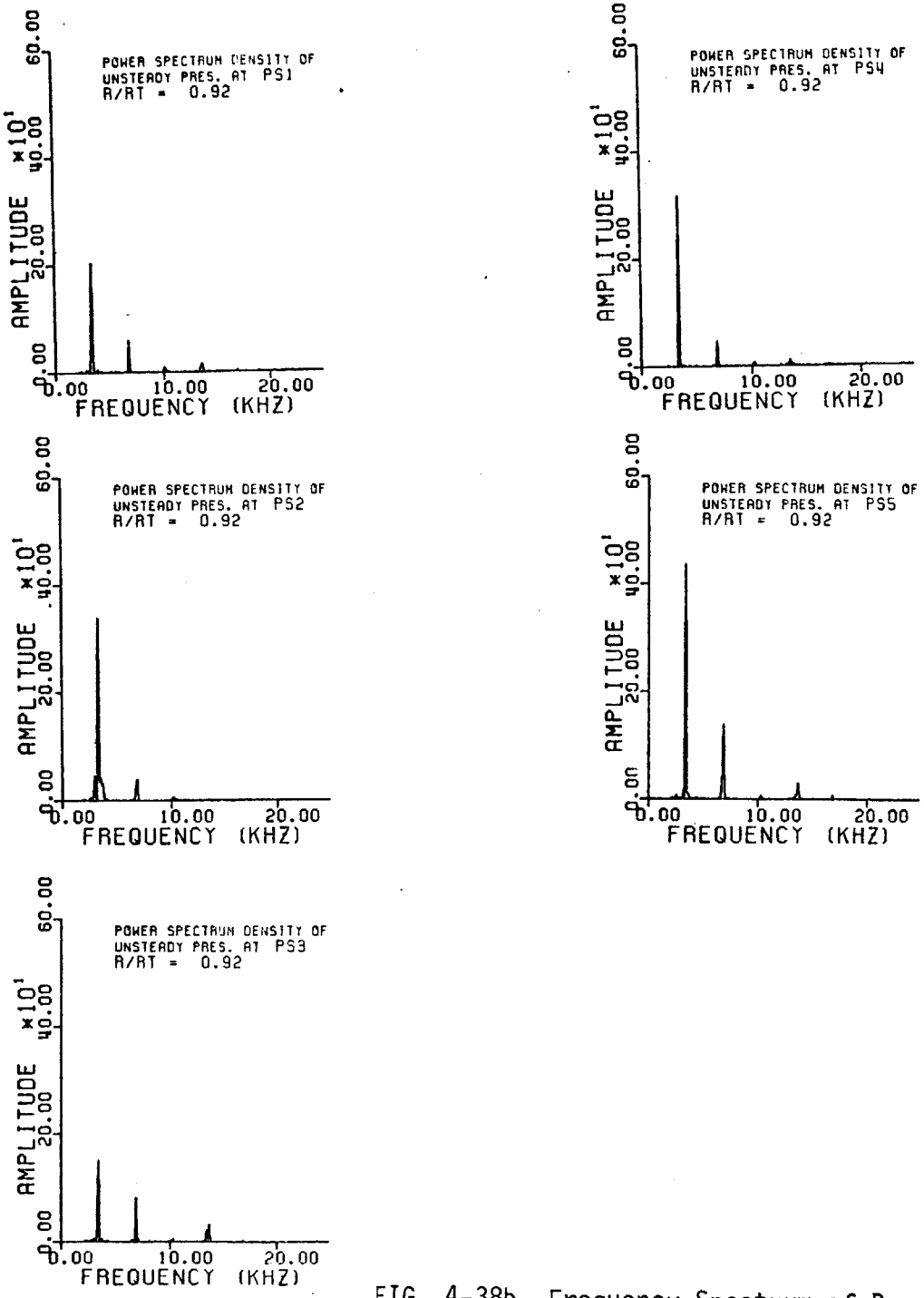

FIG. 4-38b Frequency Spectrum of Pressure Fluctuations over Stator Blade, Pressure Side, $R/R_t = 0.92$

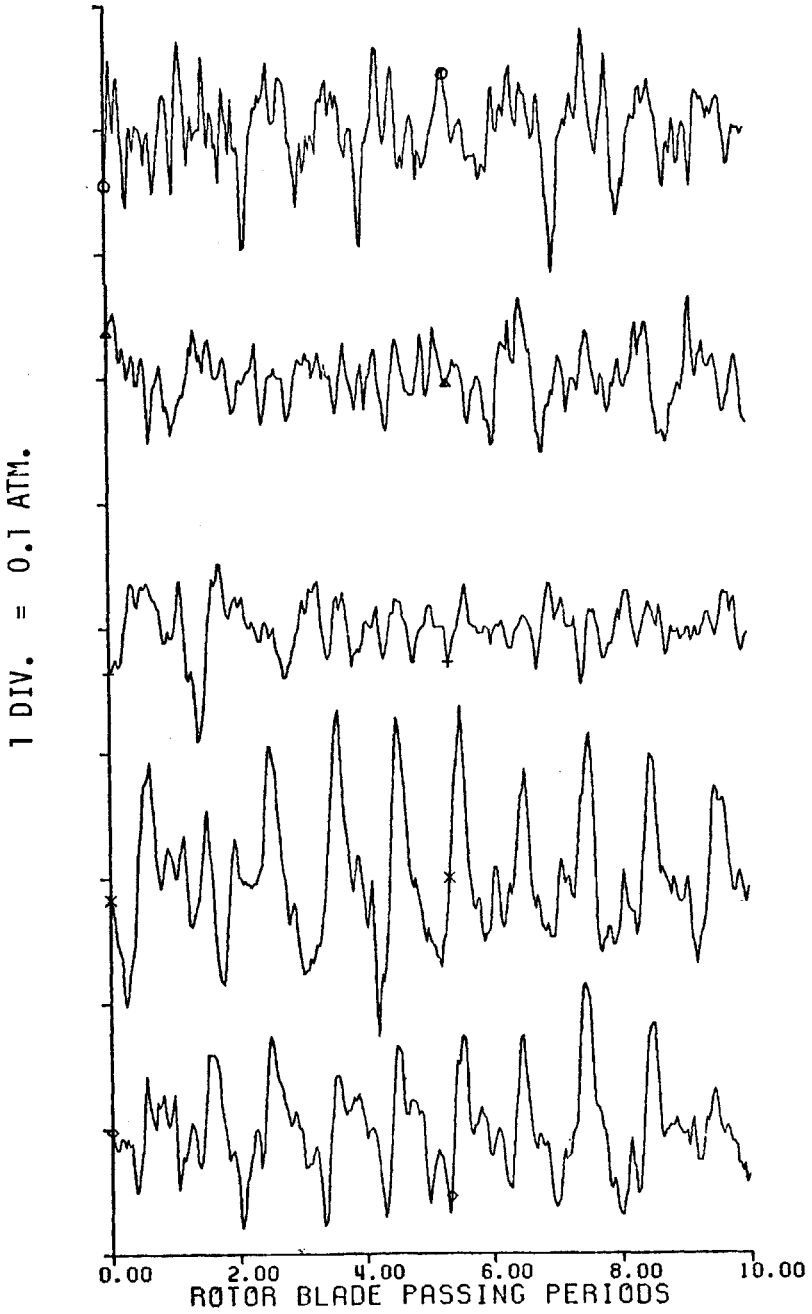

FIG. 4-39a Pressure Fluctuations over the Stator Blade, Suction Side, $R/R_t = 0.92$

(from top to bottom at 20%, 35%, 50%, 65% and 80% of chord)

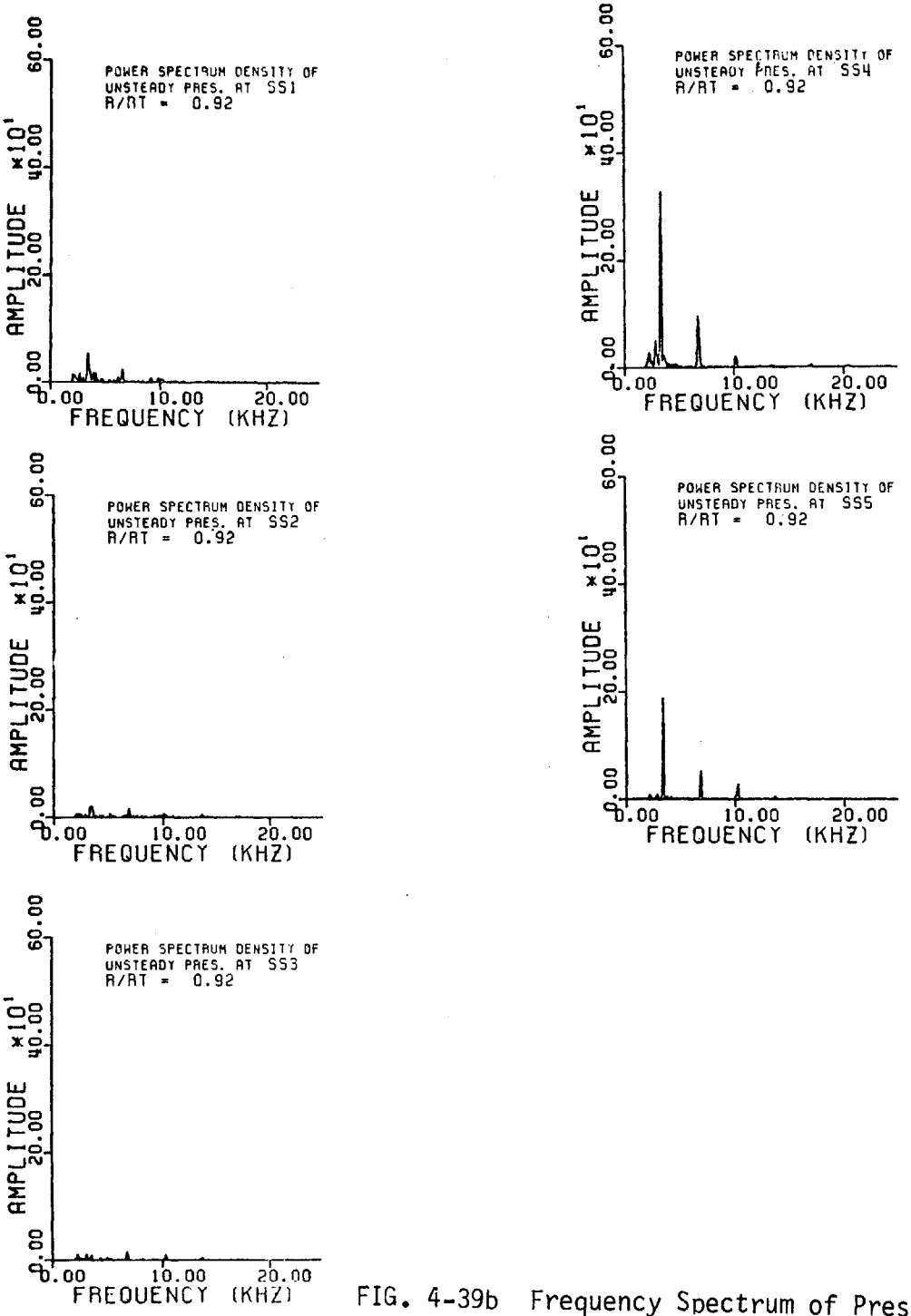

FIG. 4-39b Frequency Spectrum of Pressure Fluctuations over Stator Blade, Suction Side, $R/R_t = 0.92$

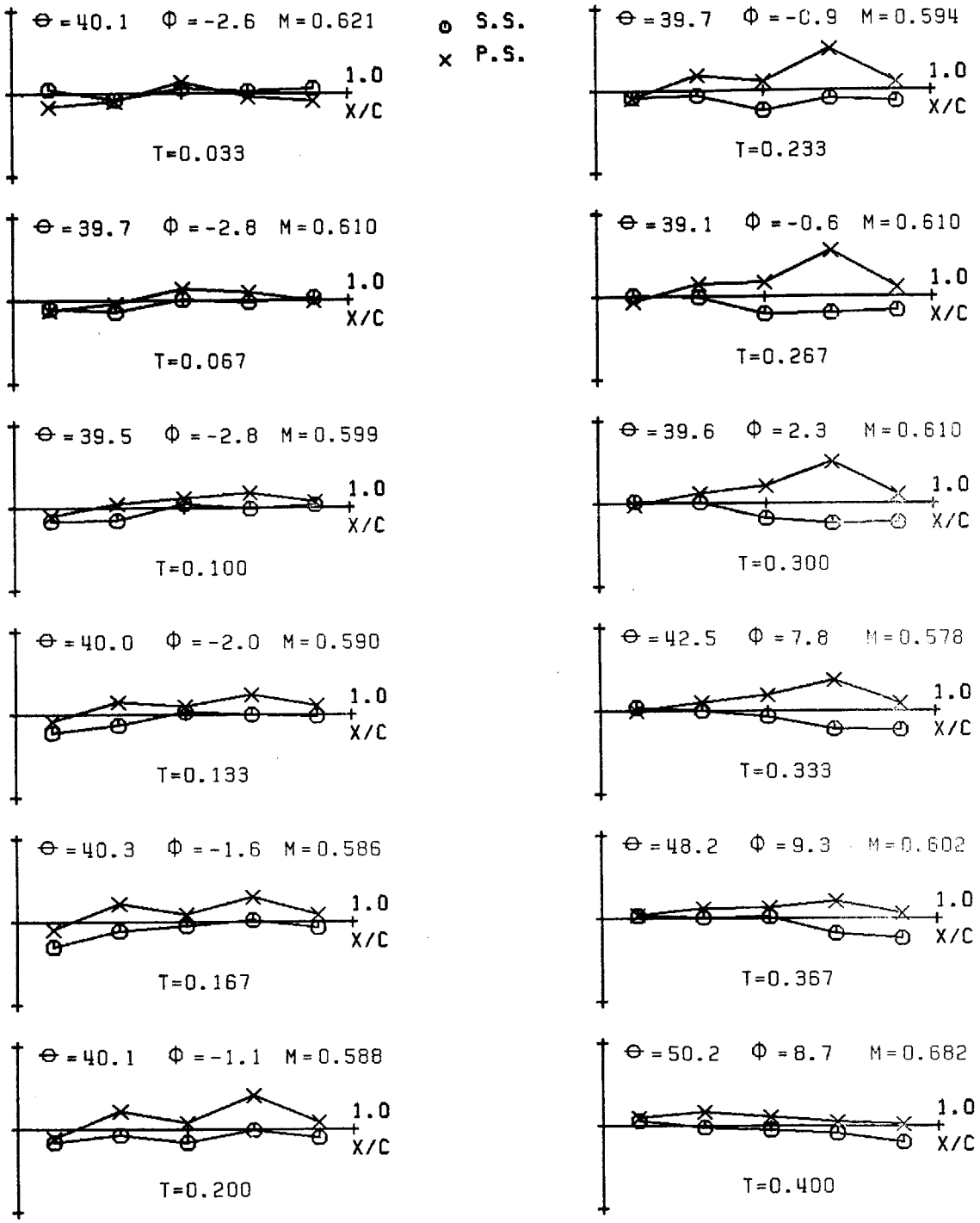

Θ=PITCHWISE FLOW ANGLE AT STATOR L.E.
Φ=RADIAL FLOW ANGLE AT STATOR L.E.
M=TOTAL MACH # AT STATOR L.E.
T=TIME / ROTOR BLADE PASSING PERIOD

TEST MIT 240 R/RT=0.72 SCALE: | =0.20 ATM

FIG. 4-40a Stator's Chordwise Distribution of Unsteady Pressure vs. Time

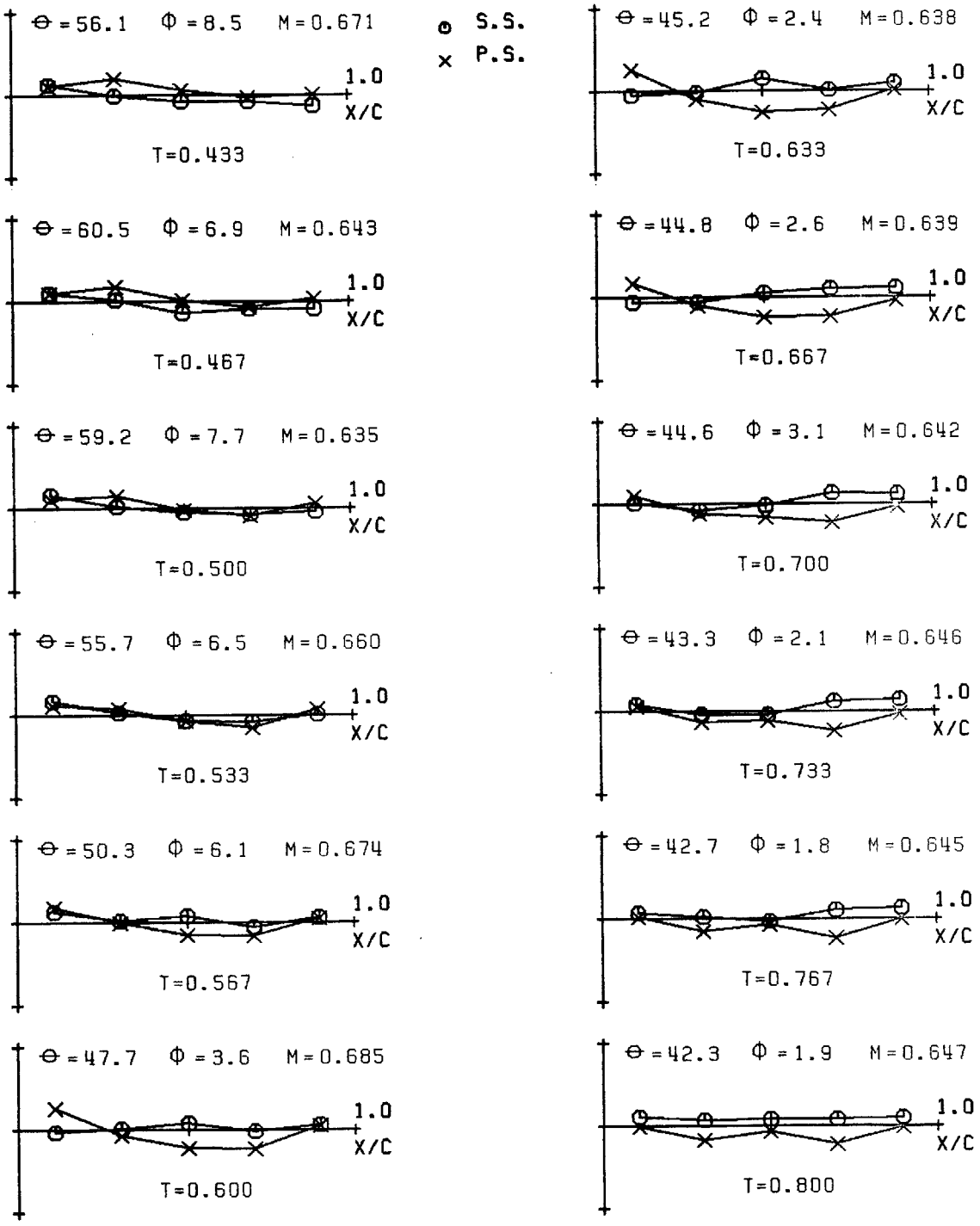

Θ=PITCHWISE FLOW ANGLE AT STATOR L.E.
Φ=RADIAL FLOW ANGLE AT STATOR L.E.
M=TOTAL MACH # AT STATOR L.E.
T=TIME / ROTOR BLADE PASSING PERIOD

TEST MIT 240 R/RT=0.72 SCALE: =0.20 ATM

FIG. 4-40b Stator's Chordwise Distribution of Unsteady Pressure vs. Time

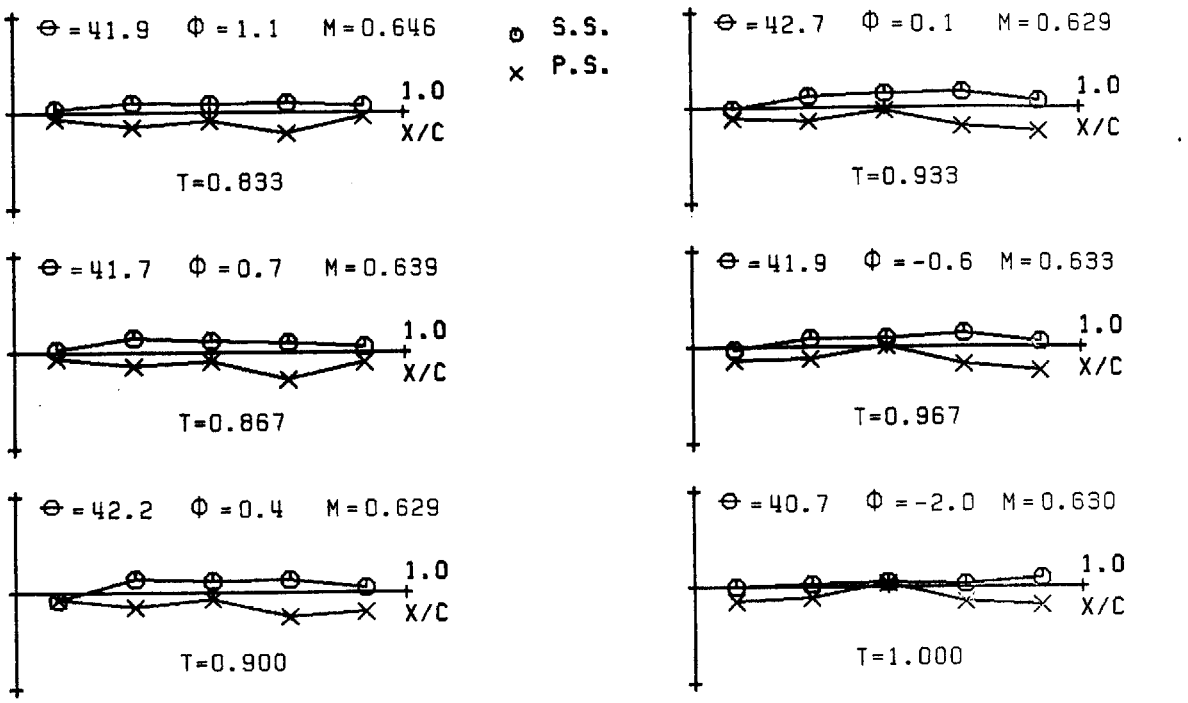

FIG. 4-40c Stator's Chordwise Distribution of Unsteady Pressure vs. Time

TEST MIT 240 R/RT=0.72 SCALE: =0.20 ATM

FIG. 4-40d Flow Angles and Mach No. at Stator Leading Edge, R/R_t = 0.72

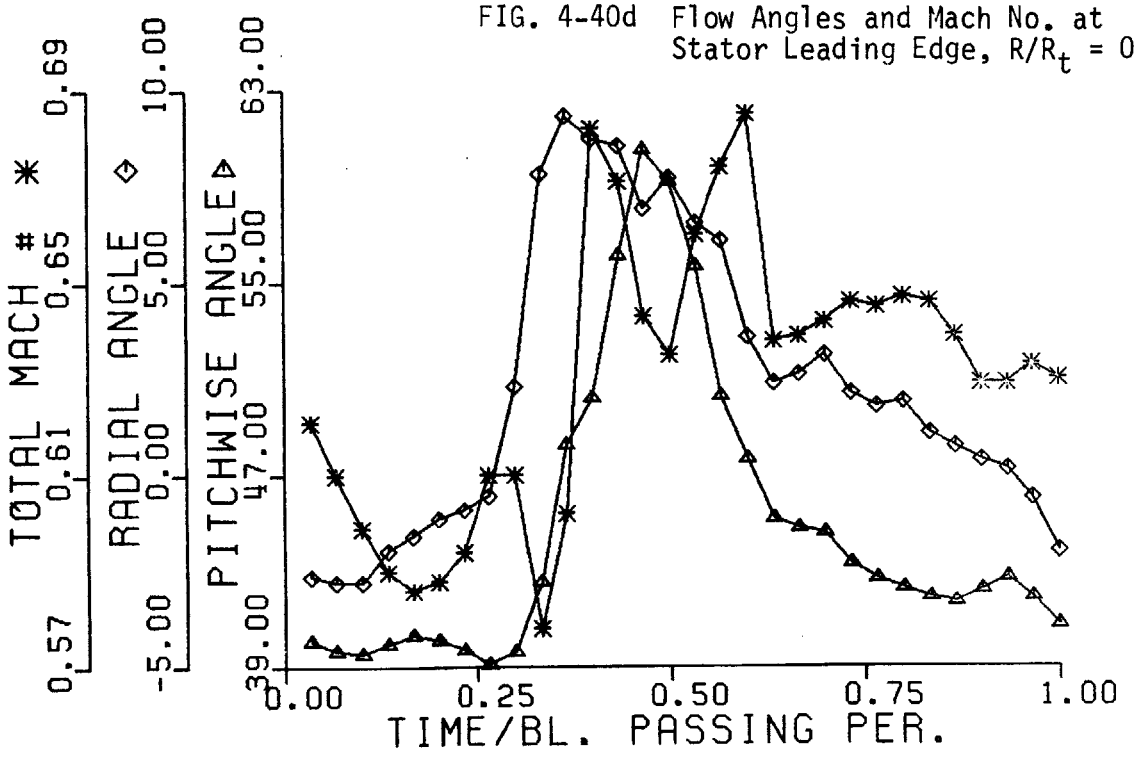

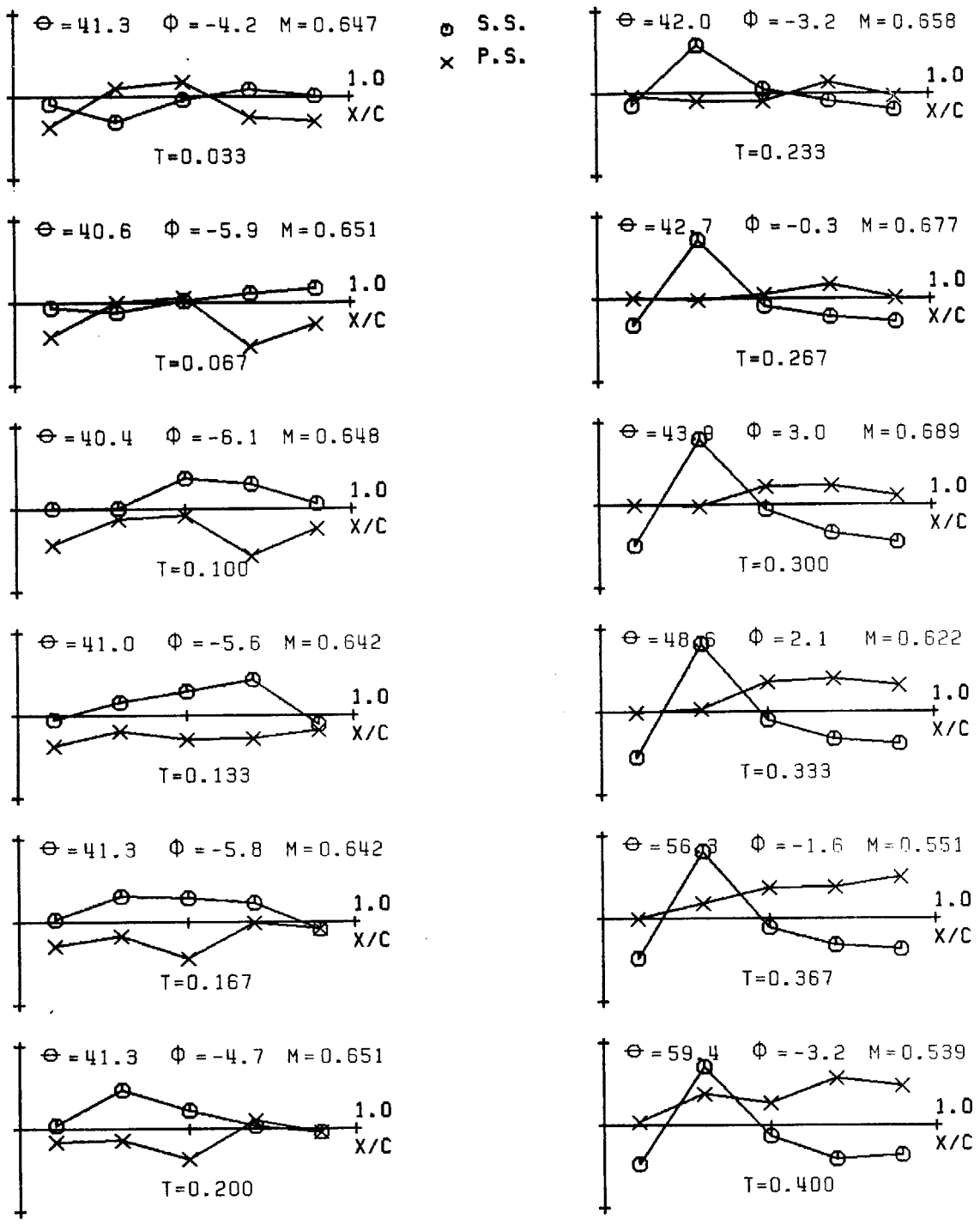

Θ=PITCHWISE FLOW ANGLE AT STATOR L.E.
Φ=RADIAL FLOW ANGLE AT STATOR L.E.
M=TOTAL MACH # AT STATOR L.E.
T=TIME / ROTOR BLADE PASSING PERIOD

TEST MIT 240 R/RT=0.82 SCALE: | =0.10 ATM

FIG. 4-41a Stator's Chordwise Distribution of Unsteady Pressure vs. Time

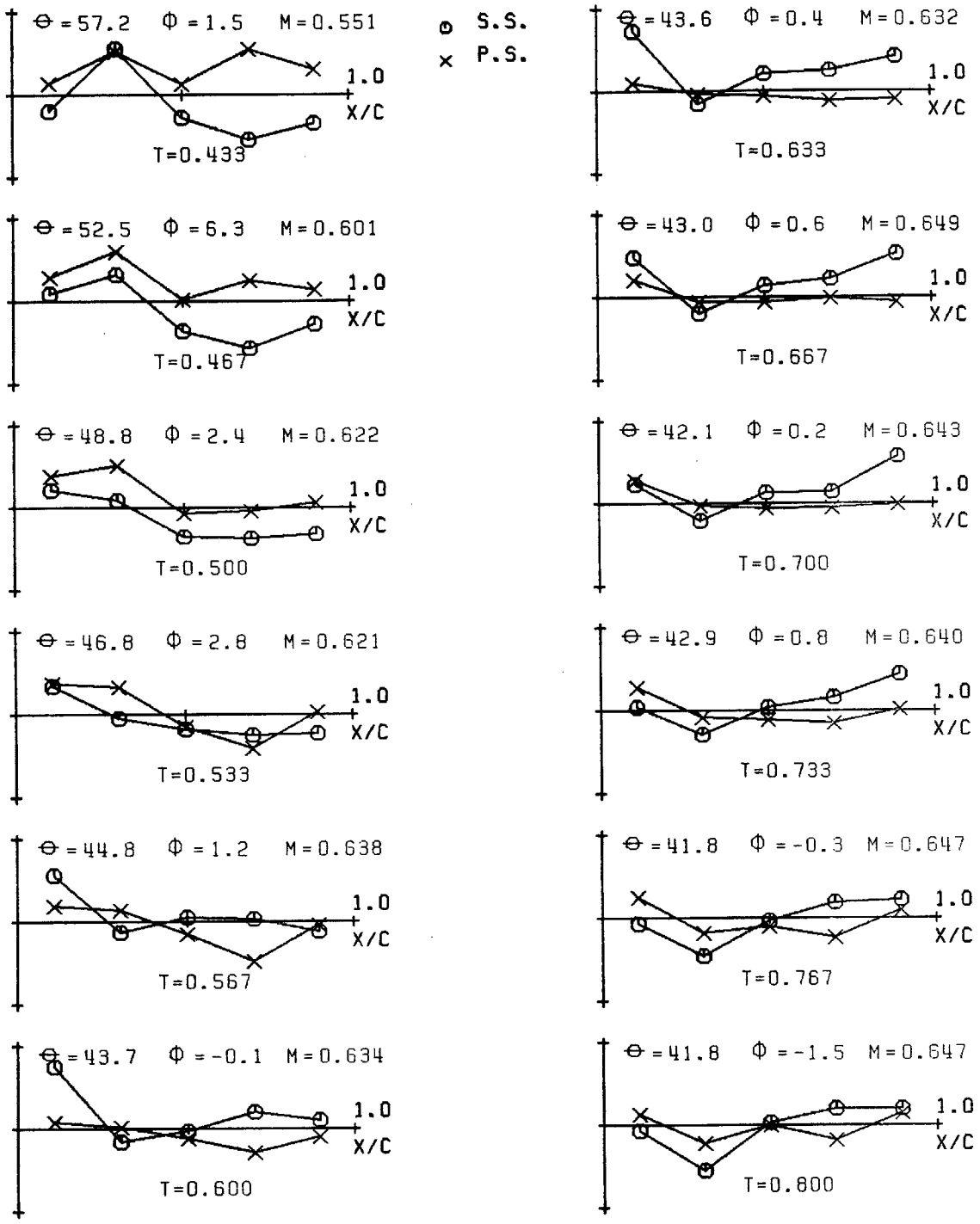

Θ=PITCHWISE FLOW ANGLE AT STATOR L.E.
Φ=RADIAL FLOW ANGLE AT STATOR L.E.
M=TOTAL MACH # AT STATOR L.E.
T=TIME / ROTOR BLADE PASSING PERIOD

TEST MIT 240 R/RT=0.82 SCALE: | =0.10 ATM

FIG. 4-41b Stator's Chordwise Distribution of Unsteady Pressure vs. Time

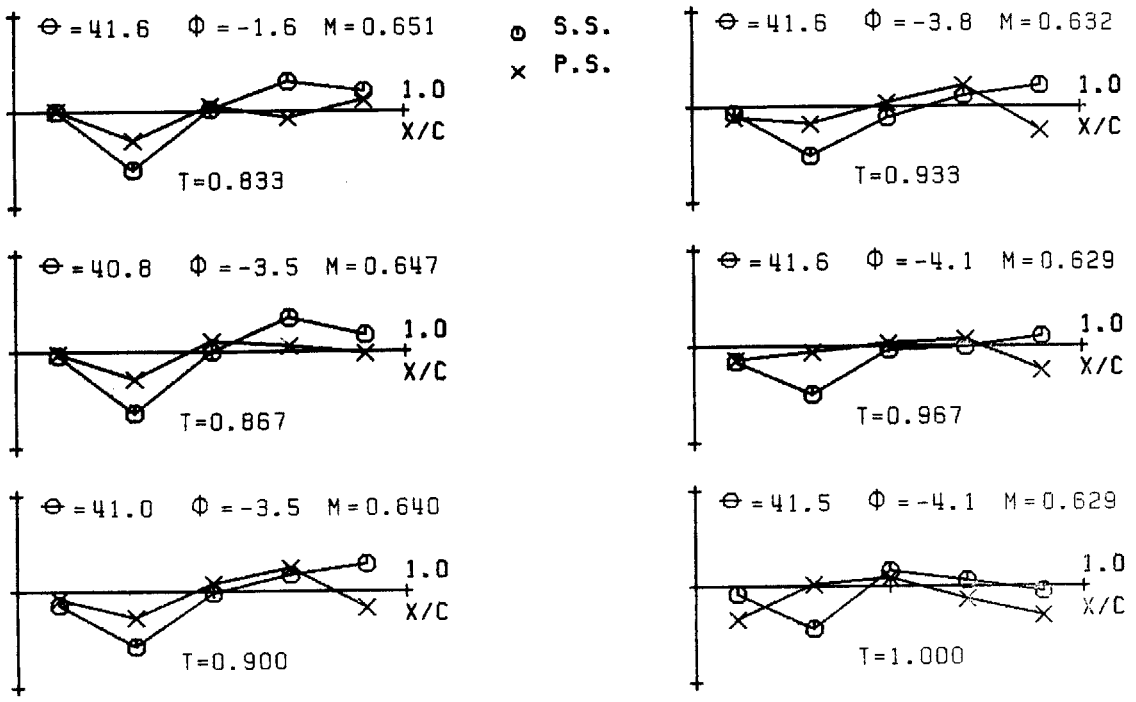

FIG. 4-41c Stator's Chordwise Distribution of Unsteady Pressure vs. Time

TEST MIT 240 R/RT=0.82 SCALE: =0.10 ATM

FIG. 4-41d Flow Angles and Mach No. at Stator Leading Edge, R/R_t = 0.82

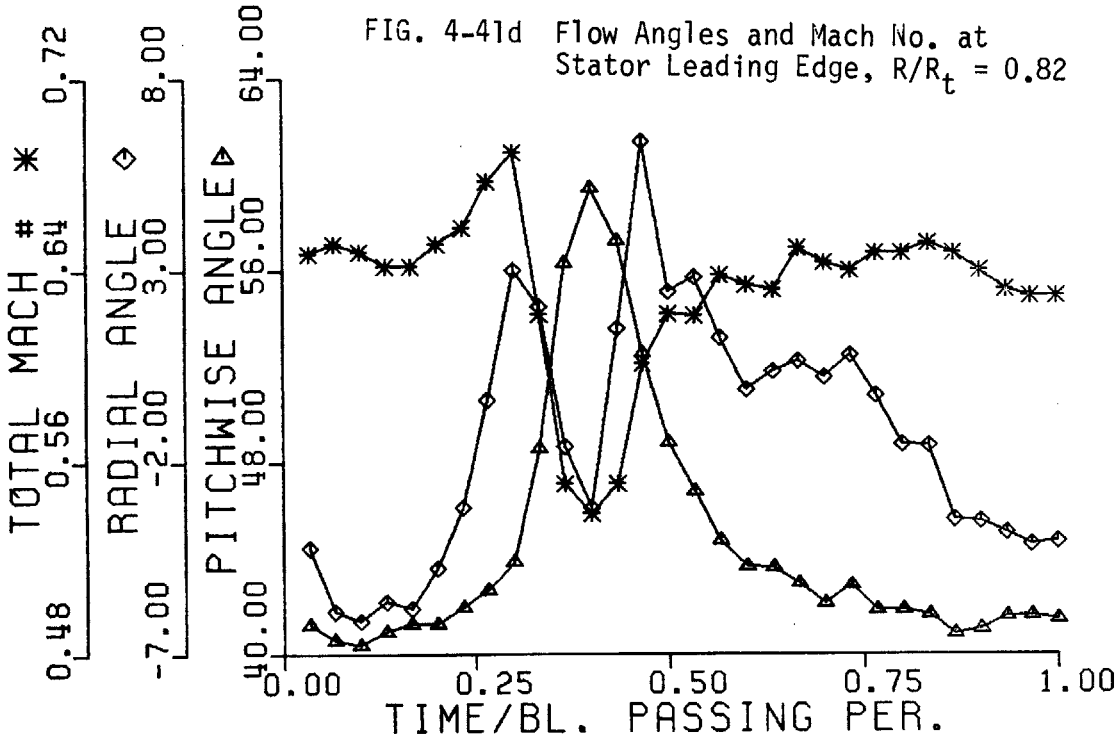

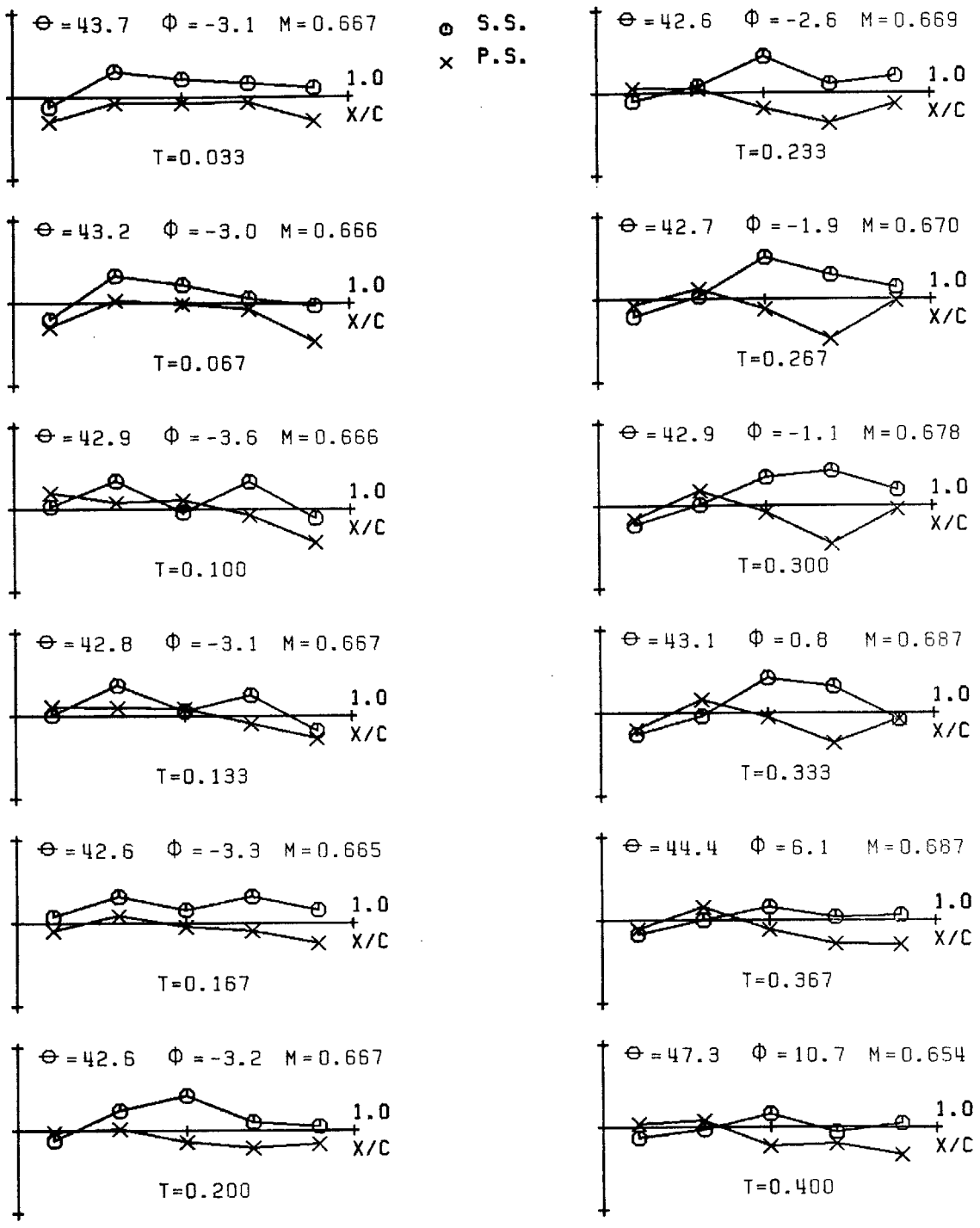

Θ=PITCHWISE FLOW ANGLE AT STATOR L.E.
Φ=RADIAL FLOW ANGLE AT STATOR L.E.
M=TOTAL MACH # AT STATOR L.E.
T=TIME / ROTOR BLADE PASSING PERIOD

TEST MIT 240 R/RT=0.92 SCALE: |=0.10 ATM

FIG. 4-42a Stator's Chordwise Distribution of Unsteady Pressure vs. Time

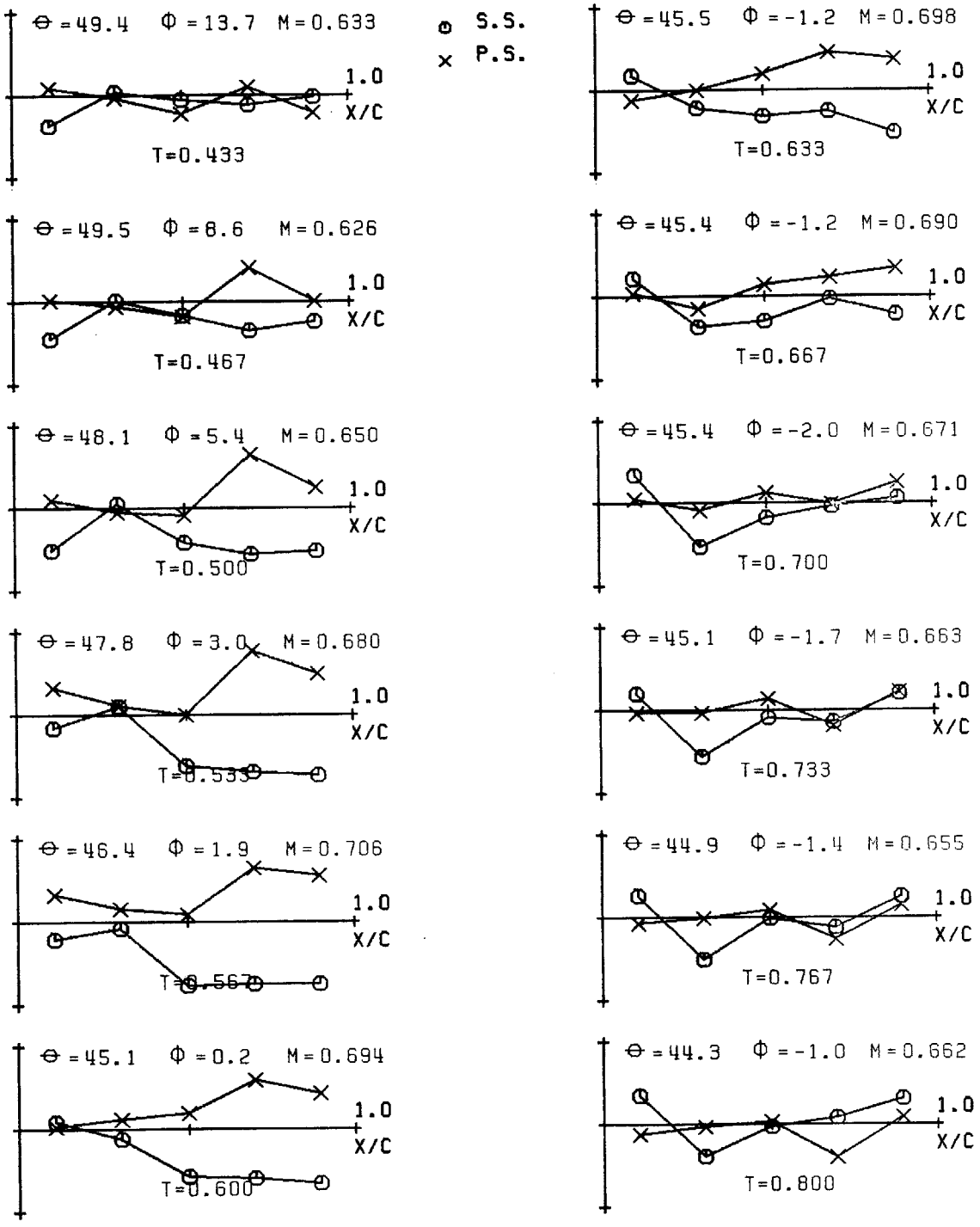

Θ=PITCHWISE FLOW ANGLE AT STATOR L.E.
Φ=RADIAL FLOW ANGLE AT STATOR L.E.
M=TOTAL MACH # AT STATOR L.E.
T=TIME / ROTOR BLADE PASSING PERIOD

TEST MIT 240 R/RT=0.92 SCALE: | =0.10 ATM

FIG. 4-42b Stator's Chordwise Distribution of Unsteady Pressure vs. Time

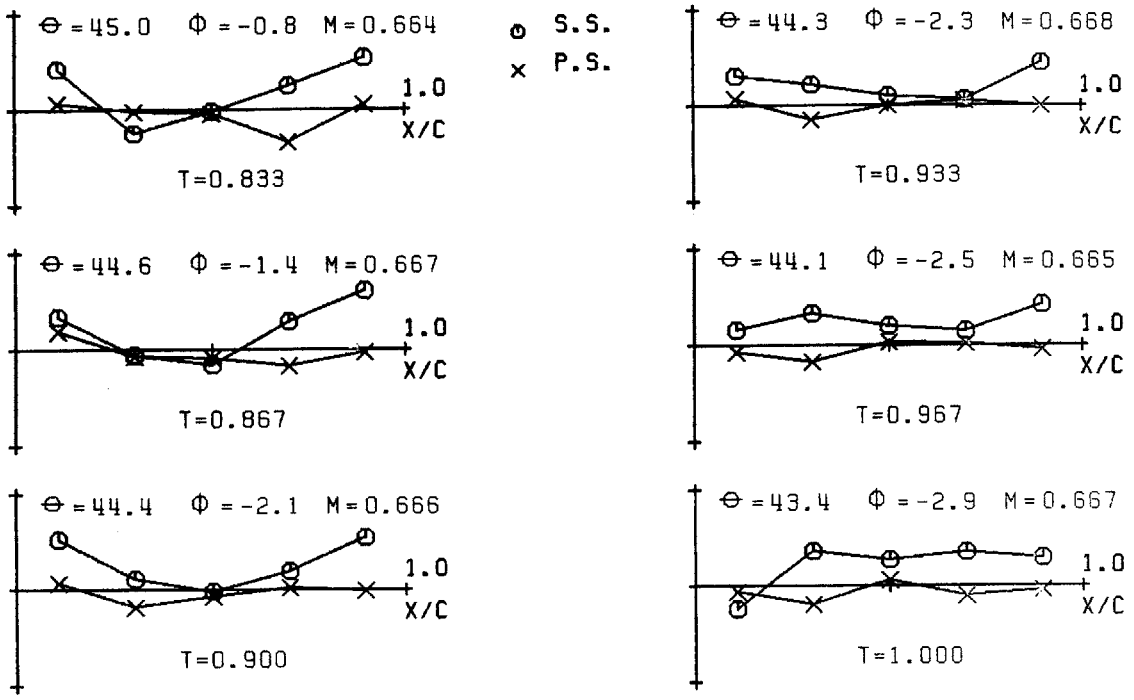

FIG. 4-42c Stator's Chordwise Distribution of Unsteady Pressure vs. Time

TEST MIT 240 R/RT=0.92 SCALE: =0.10 ATM

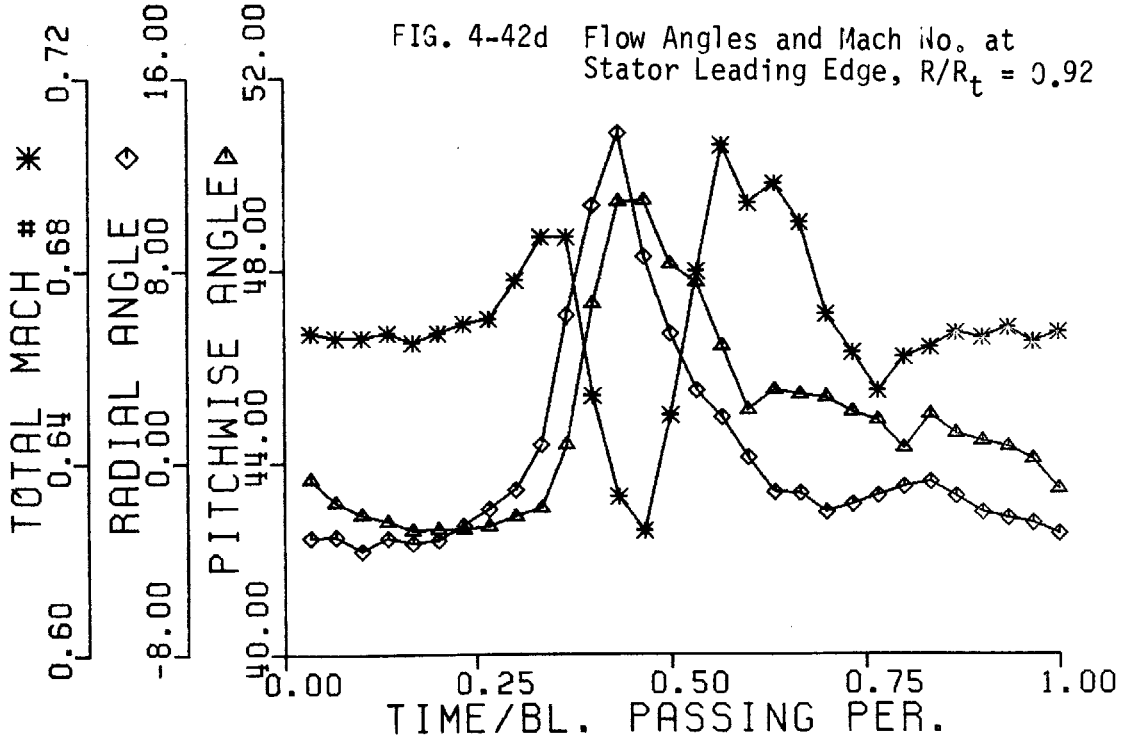

FIG. 4-42d Flow Angles and Mach No. at Stator Leading Edge, R/R_t = 0.92

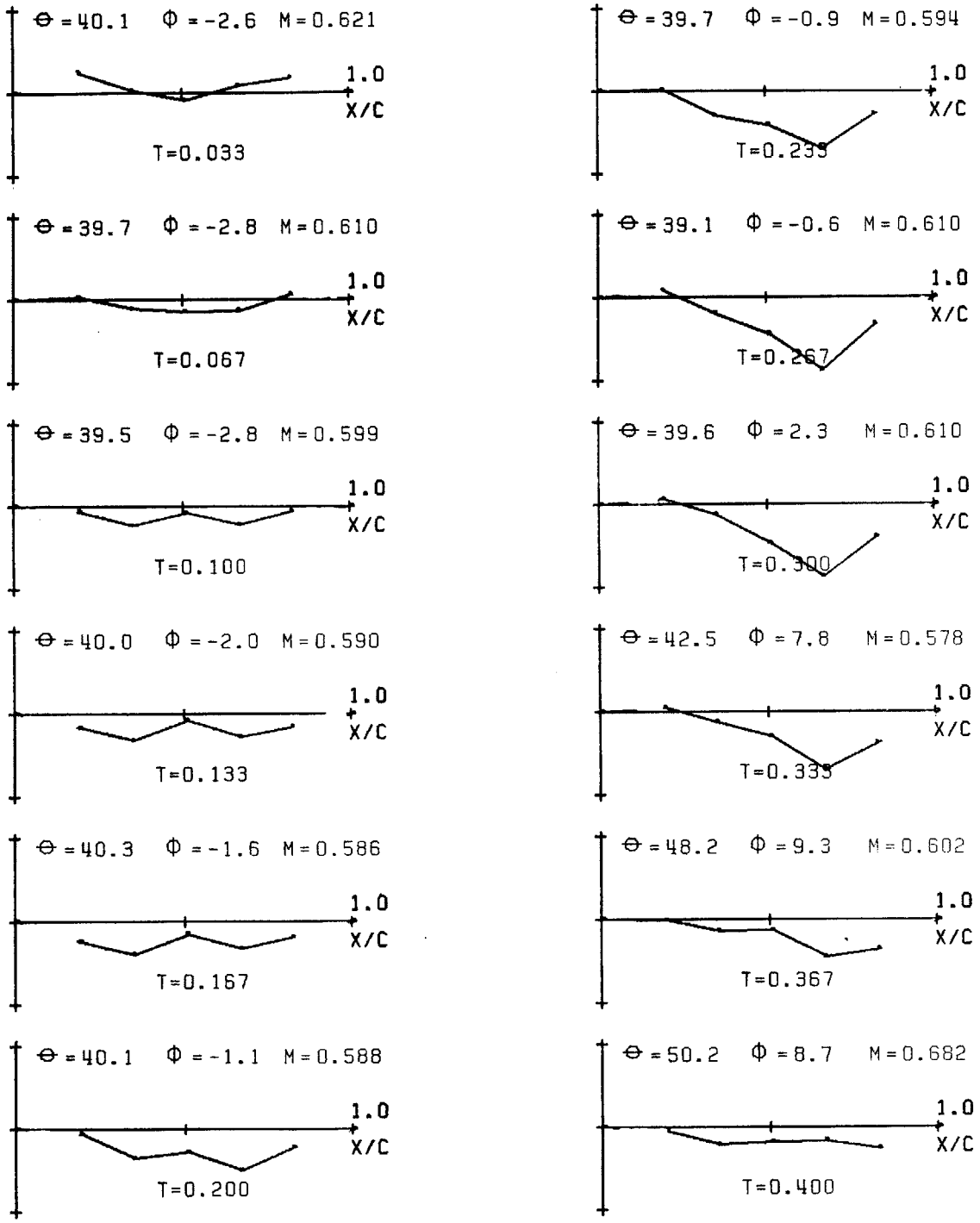

Θ=PITCHWISE FLOW ANGLE AT STATOR L.E.
Φ=RADIAL FLOW ANGLE AT STATOR L.E.
M=TOTAL MACH # AT STATOR L.E.
T=TIME / ROTOR BLADE PASSING PERIOD

"LIFT COEFFICIENT"

SCALE: | =0.50

TEST MIT 240 R/RT=0.72

FIG. 4-43a Stator's Chordwise Distribution of Unsteady Life Coefficient vs. Time

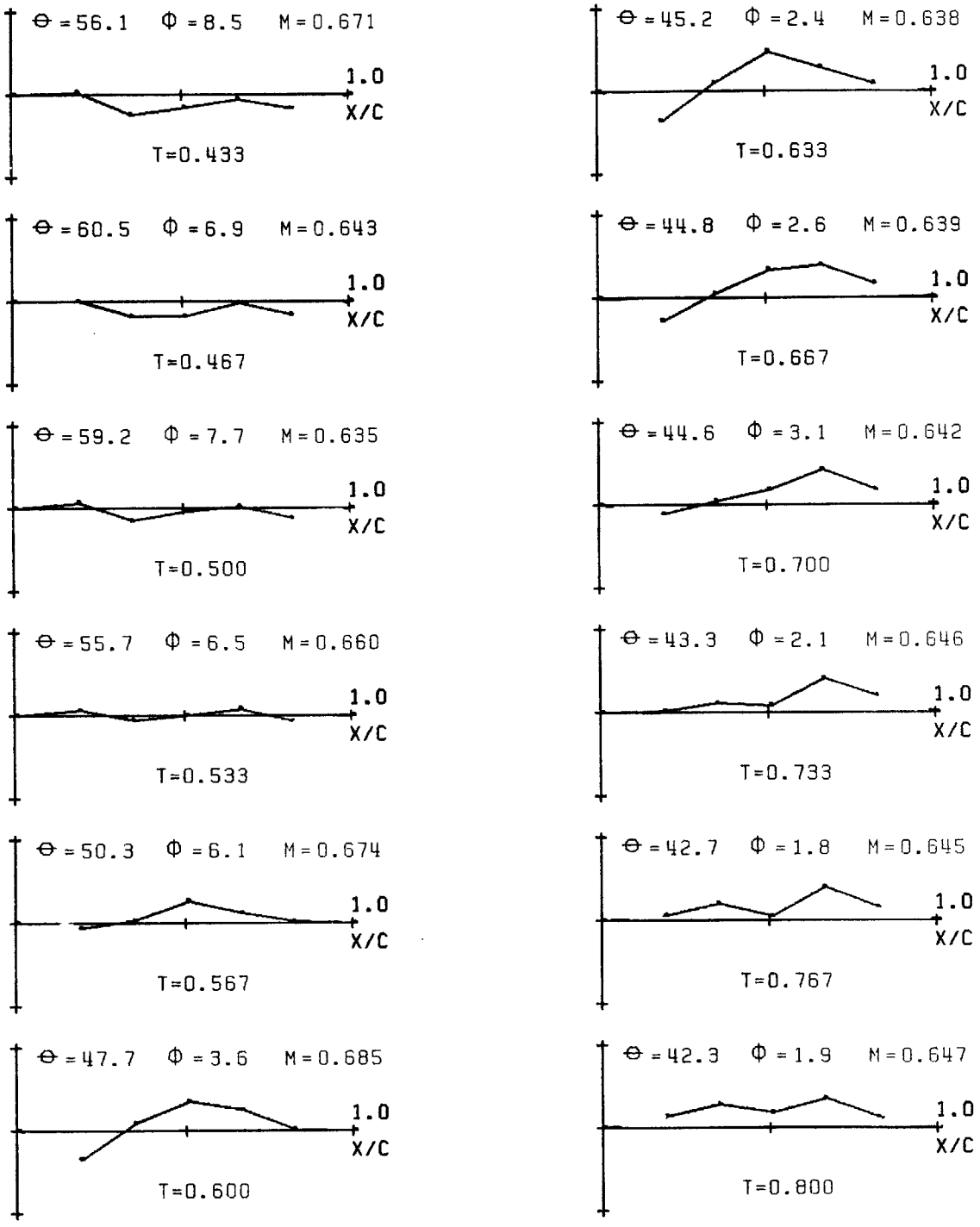

Θ=PITCHWISE FLOW ANGLE AT STATOR L.E.
Φ=RADIAL FLOW ANGLE AT STATOR L.E.
M=TOTAL MACH # AT STATOR L.E.
T=TIME / ROTOR BLADE PASSING PERIOD

"LIFT COEFFICIENT"

SCALE: | =0.50

TEST MIT 240 R/RT=0.72

FIG. 4-43b Stator's Chordwise Distribution of Unsteady Lift Coefficient vs. Time

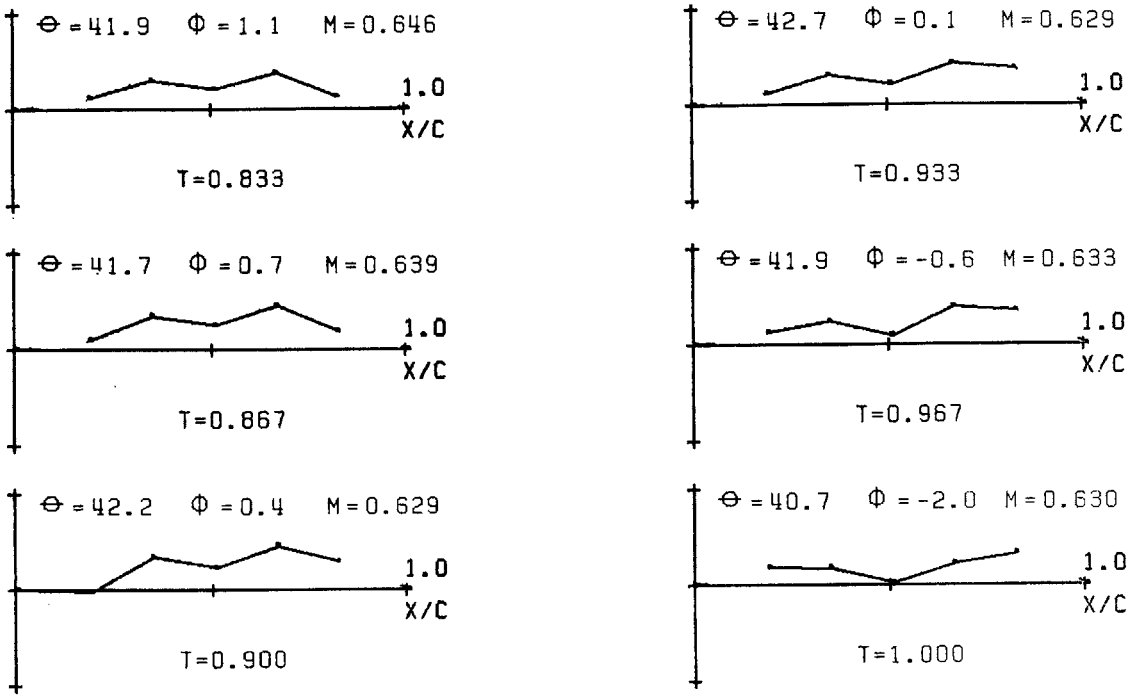

FIG. 4-43c Stator's Chordwise Distribution of Unsteady Lift Coefficient vs. Time

TEST MIT 240 R/RT=0.72 SCALE: =0.50

FIG. 4-43d Flow Angles and Mach No. at Stator Leading Edge, R/R_t = 0.72

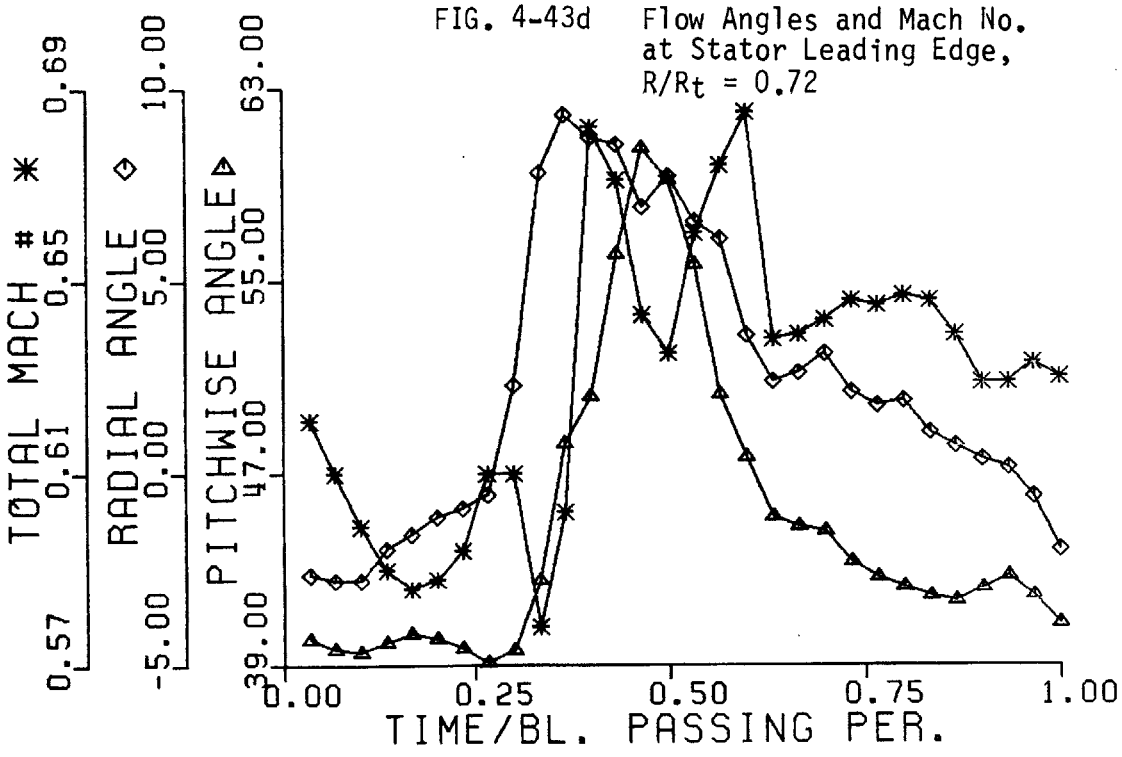

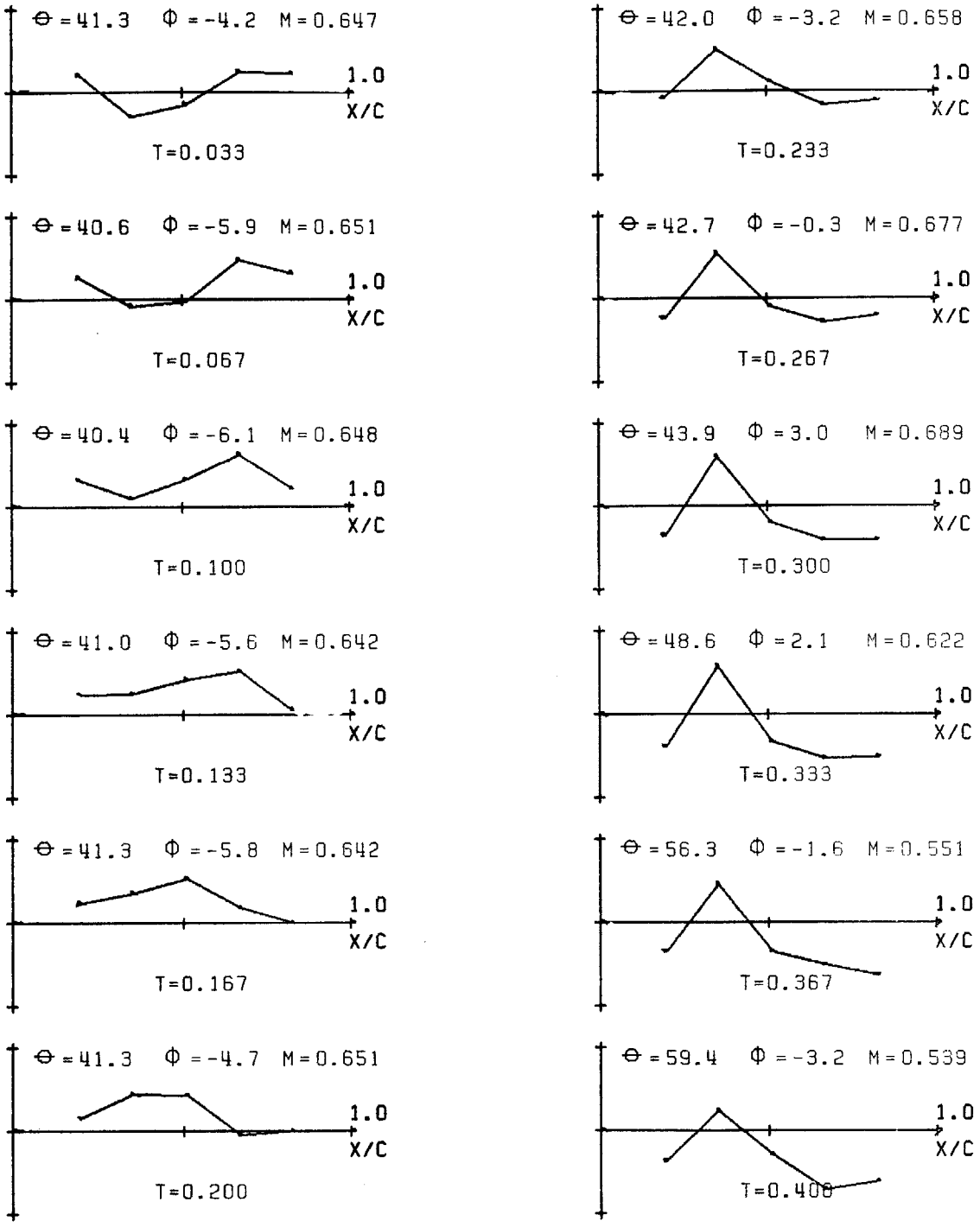

Θ=PITCHWISE FLOW ANGLE AT STATOR L.E.
Φ=RADIAL FLOW ANGLE AT STATOR L.E.
M=TOTAL MACH # AT STATOR L.E.
T=TIME / ROTOR BLADE PASSING PERIOD

"LIFT COEFFICIENT"

TEST MIT 240 R/RT=0.82 SCALE: | =0.40

FIG. 4-44a Stator's Chordwise Distribution of Unsteady Lift Coefficient vs. Time

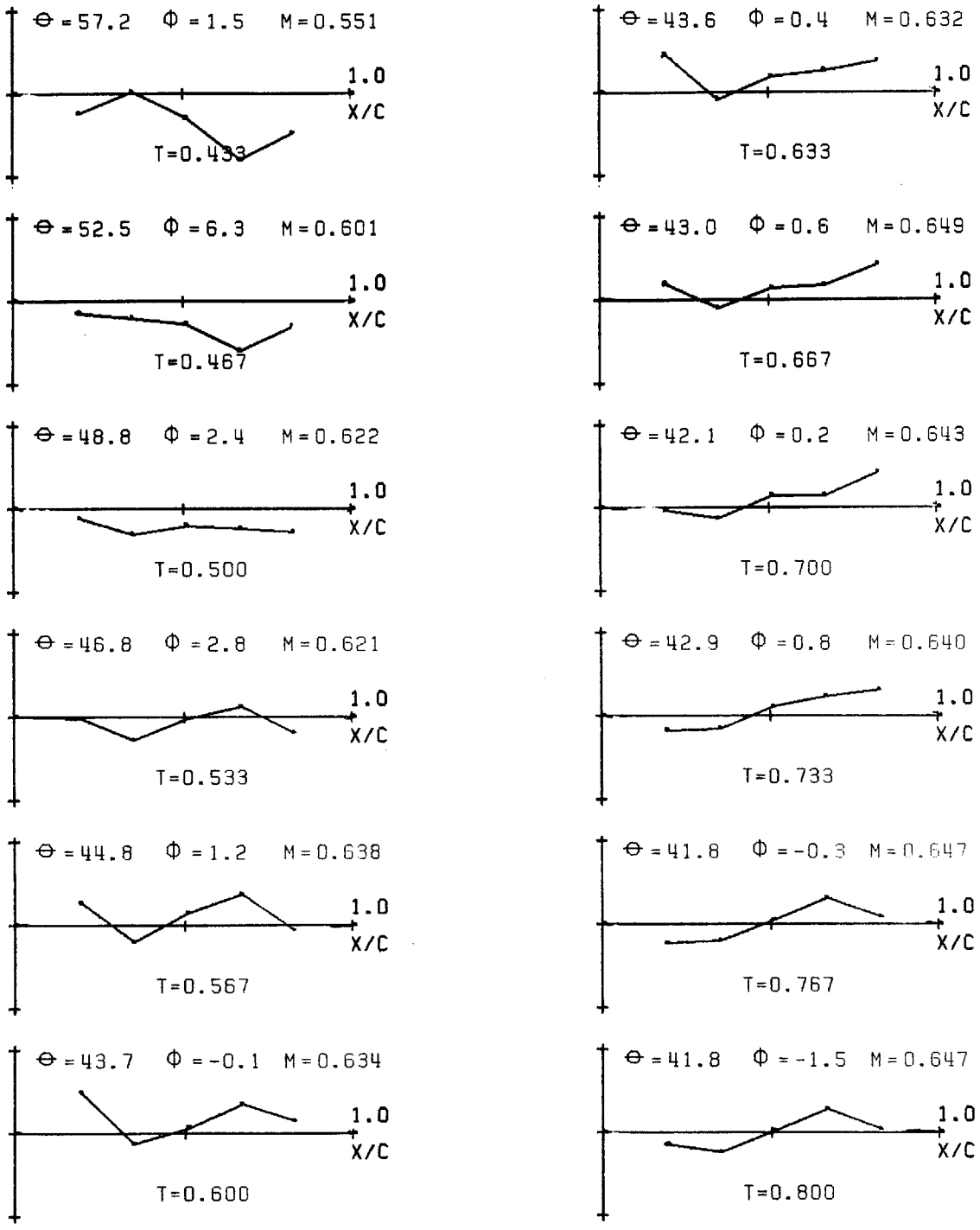

Θ=PITCHWISE FLOW ANGLE AT STATOR L.E.
Φ=RADIAL FLOW ANGLE AT STATOR L.E.
M=TOTAL MACH # AT STATOR L.E.
T=TIME / ROTOR BLADE PASSING PERIOD

"LIFT COEFFICIENT"

TEST MIT 240 R/RT=0.82 SCALE: | =0.40

FIG. 4-44b Stator's Chordwise Distribution of Unsteady Lift Coefficient vs. Time

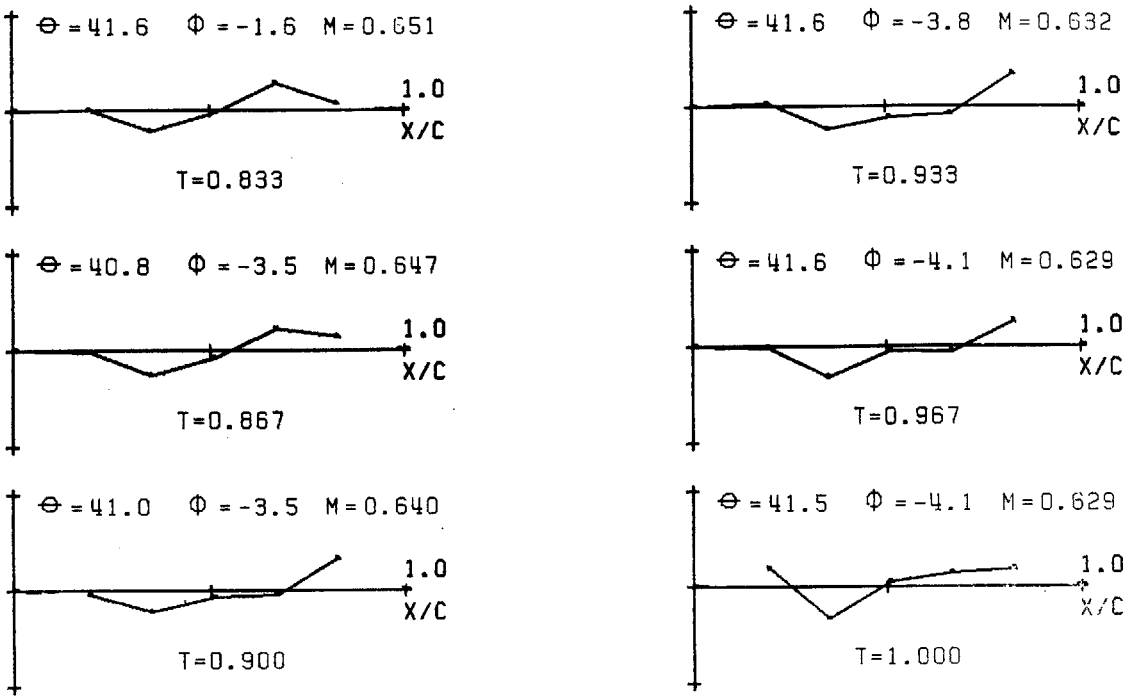

FIG. 4-44c Stator's Chordwise Distribution of Unsteady Lift Coefficient vs. Time

TEST MIT 240 R/RT=0.82 SCALE: =0.40

FIG. 4-44d Flow Angles and Mach No. at Stator Leading Edge, R/R_t = 0.82

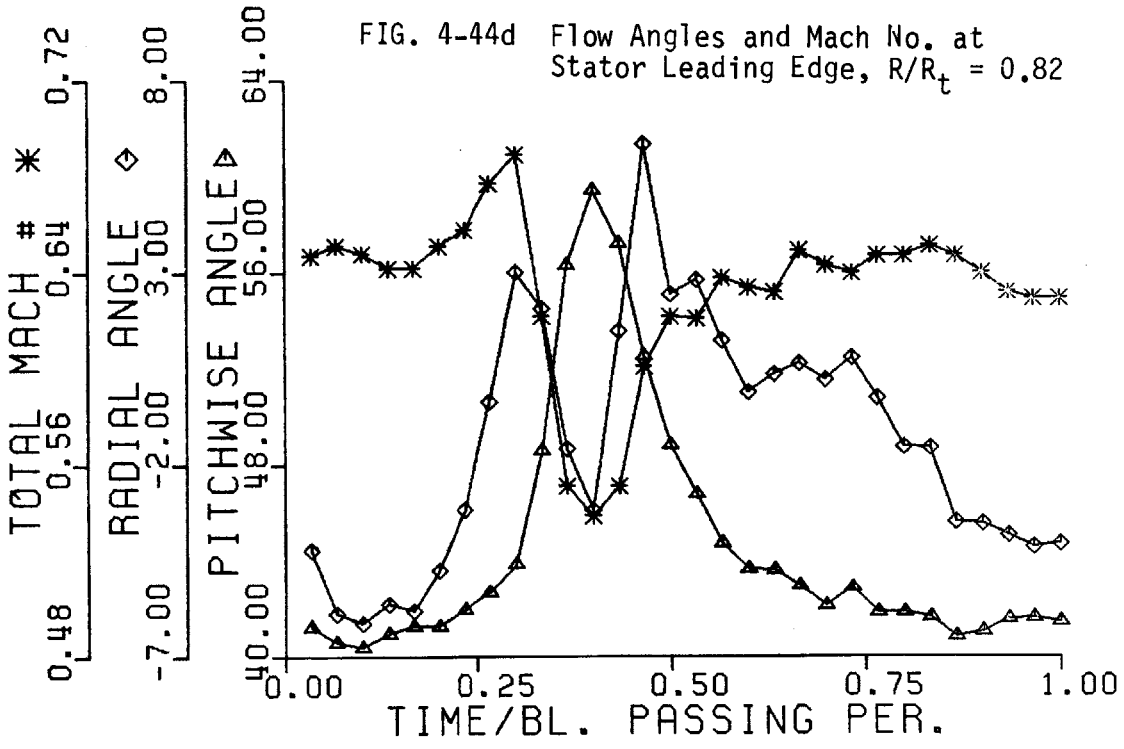

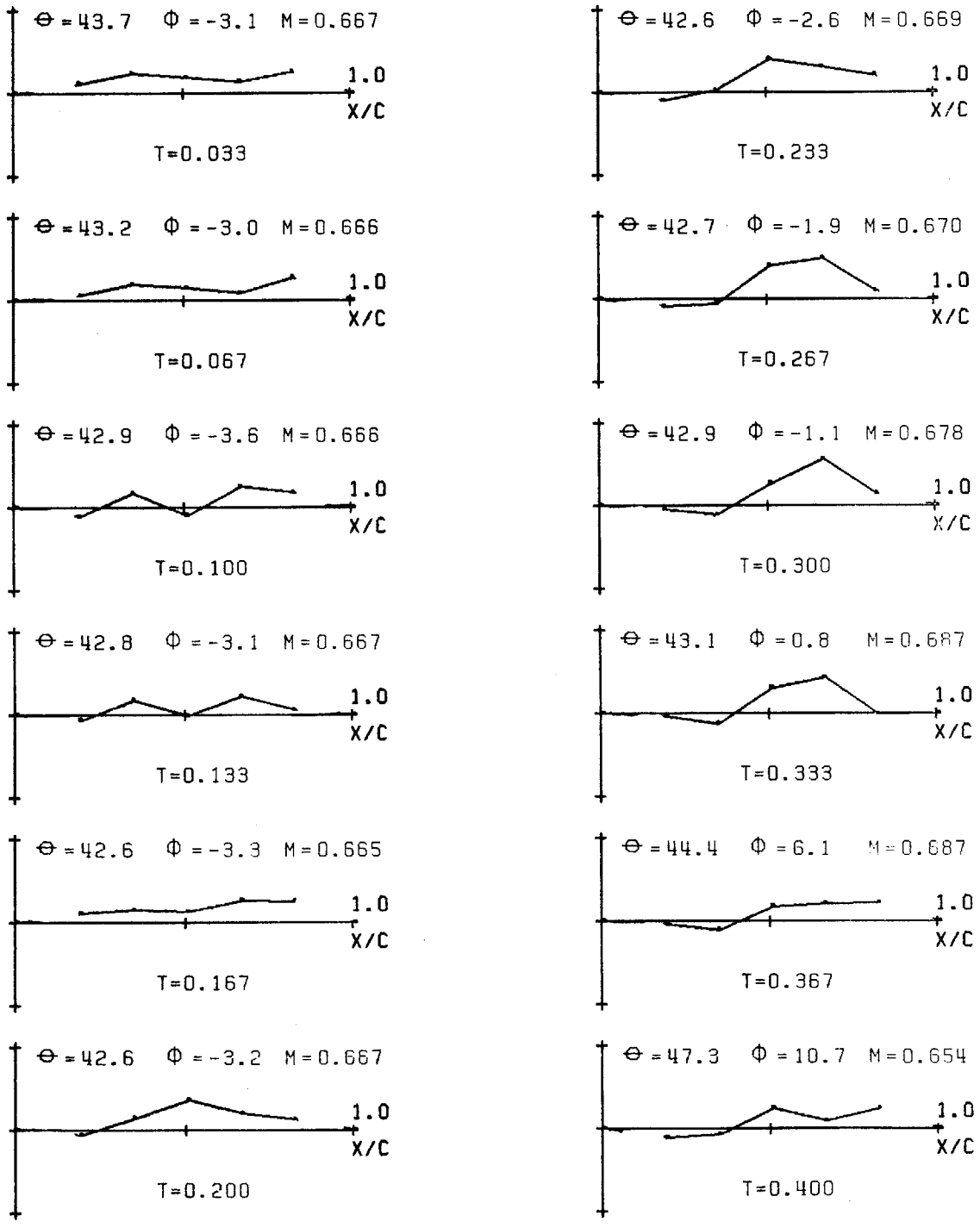

Θ=PITCHWISE FLOW ANGLE AT STATOR L.E.
Φ=RADIAL FLOW ANGLE AT STATOR L.E.
M=TOTAL MACH # AT STATOR L.E.
T=TIME / ROTOR BLADE PASSING PERIOD

"LIFT COEFFICIENT"

SCALE: | =0.40

TEST MIT 240 R/RT=0.92

FIG. 4-45a Stator's Chordwise Distribution of Unsteady Lift Coefficient vs. Time

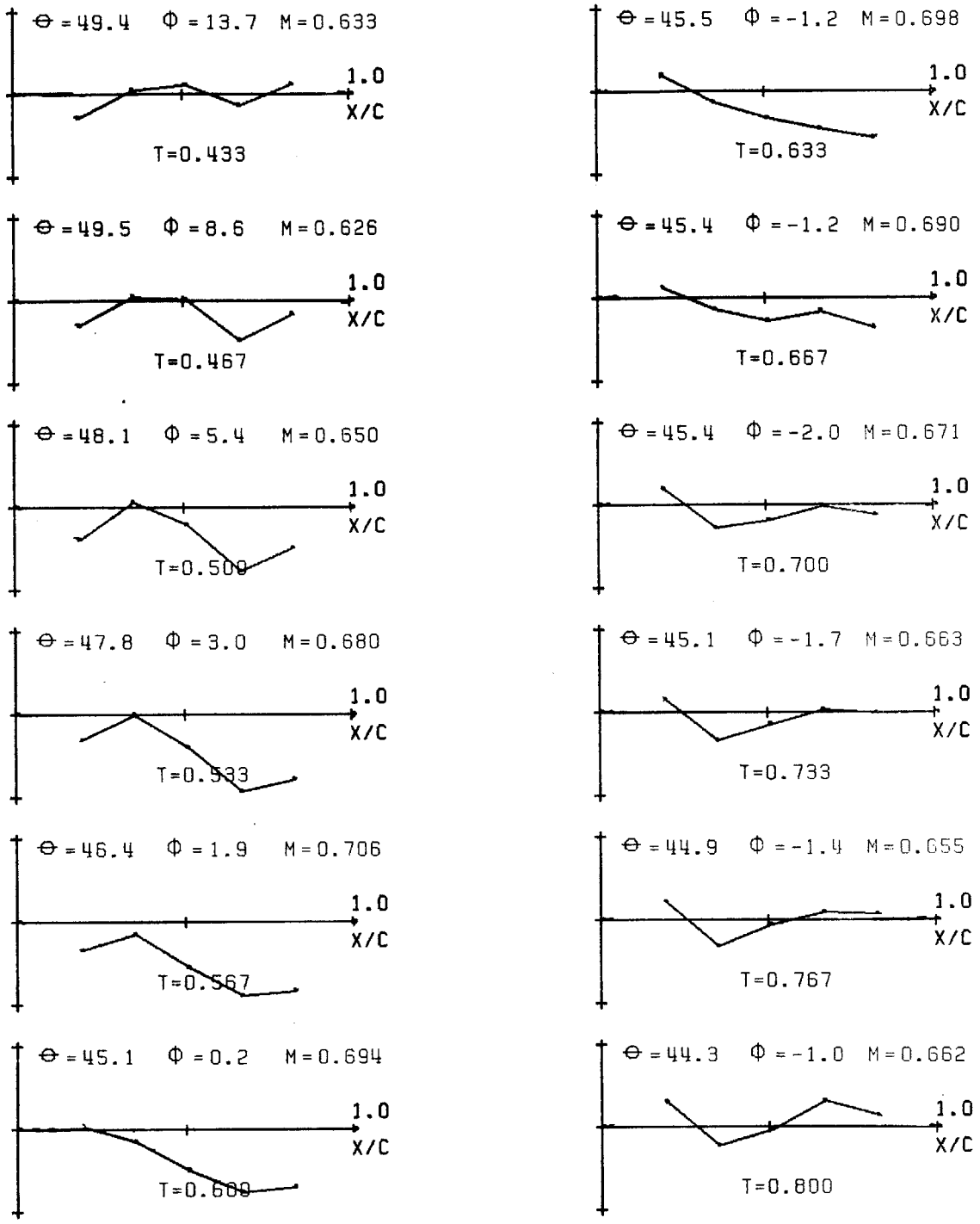

Θ=PITCHWISE FLOW ANGLE AT STATOR L.E.
Φ=RADIAL FLOW ANGLE AT STATOR L.E.
M=TOTAL MACH # AT STATOR L.E.
T=TIME / ROTOR BLADE PASSING PERIOD

"LIFT COEFFICIENT"

TEST MIT 240 R/RT=0.92 SCALE: | =0.40

FIG. 4-45b Stator's Chordwise Distribution of Unsteady Lift Coefficient vs. Time

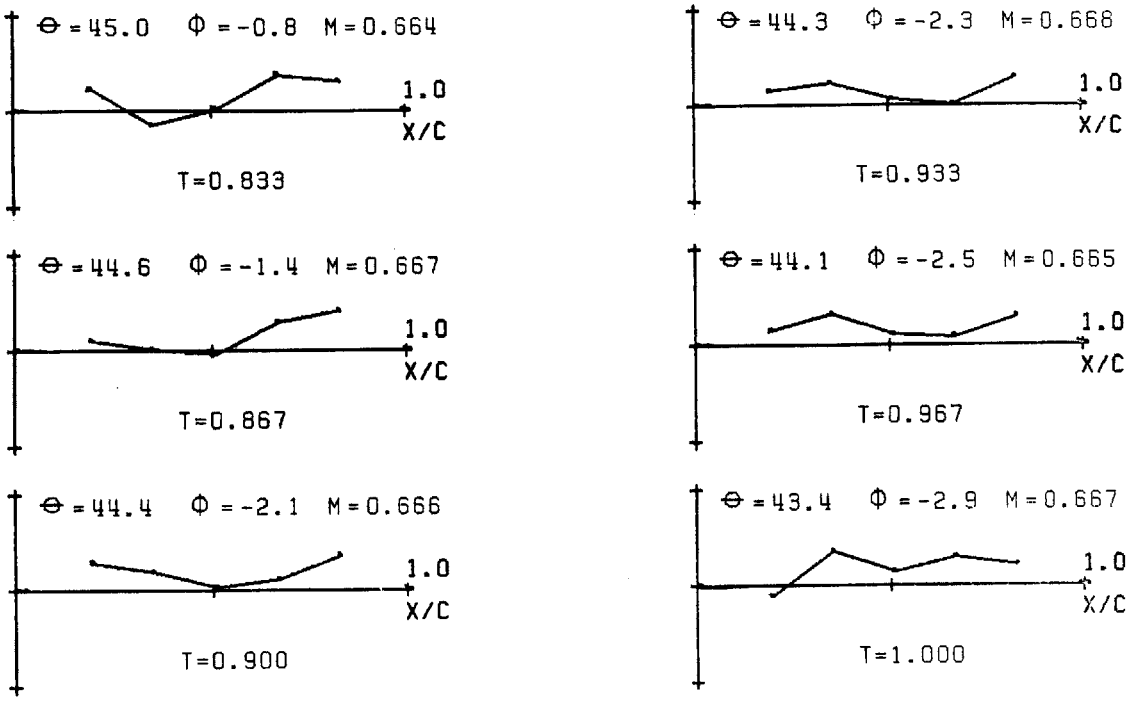

FIG. 4-45c Stator's Chordwise Distribution of Unsteady Lift Coefficient vs. Time

TEST MIT 240 R/RT=0.92 SCALE: =0.40

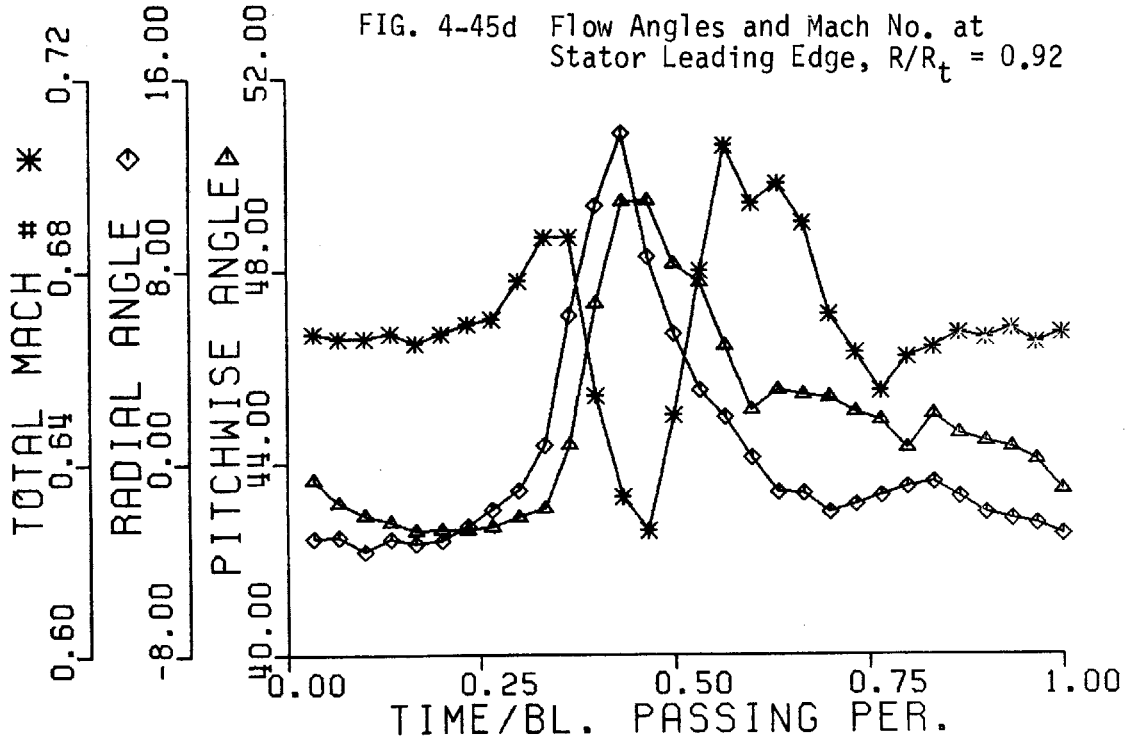

FIG. 4-45d Flow Angles and Mach No. at Stator Leading Edge, R/R_t = 0.92

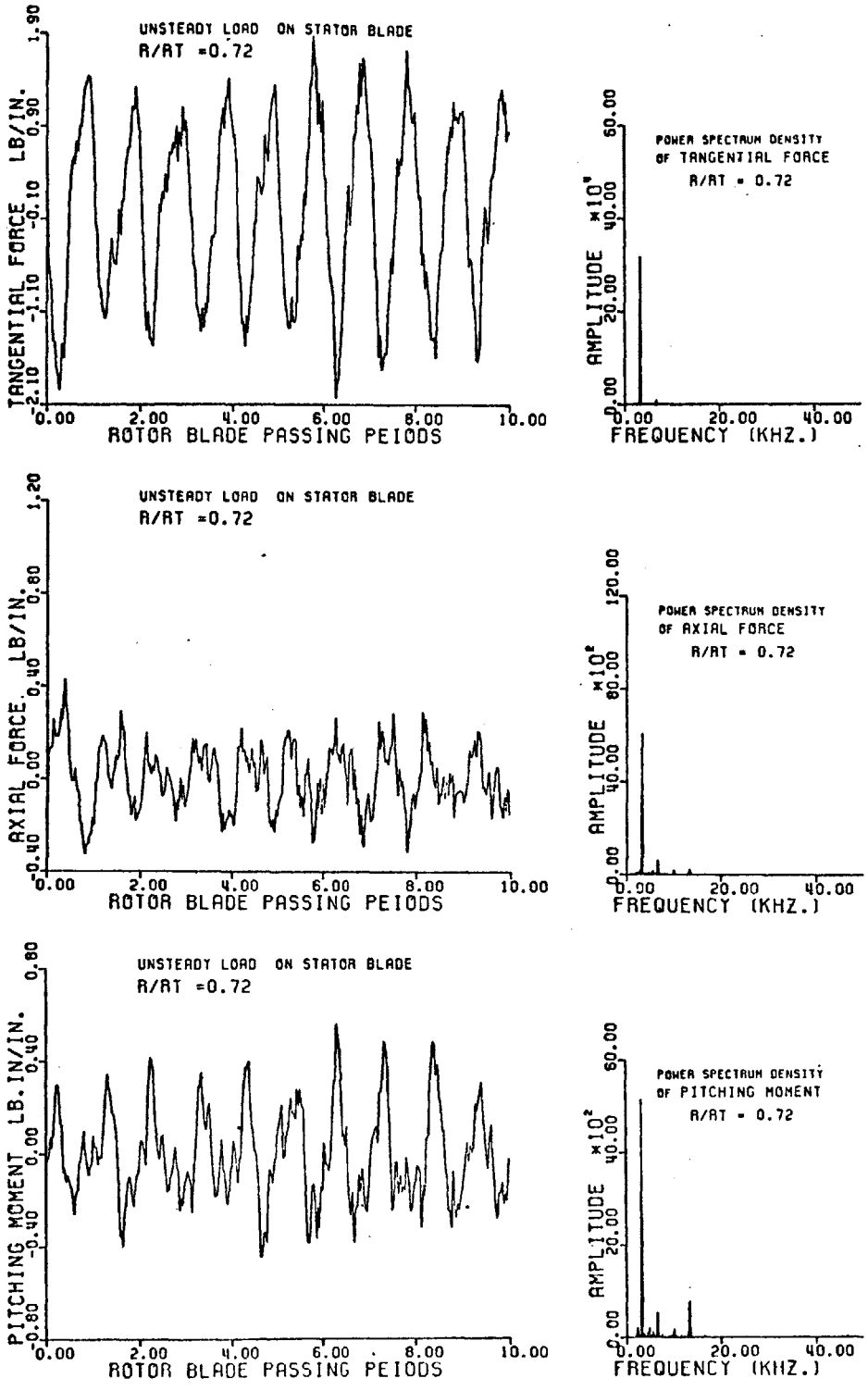

FIG. 4-46 Unsteady Loads on Stator Blade, $R/R_T = 0.72$

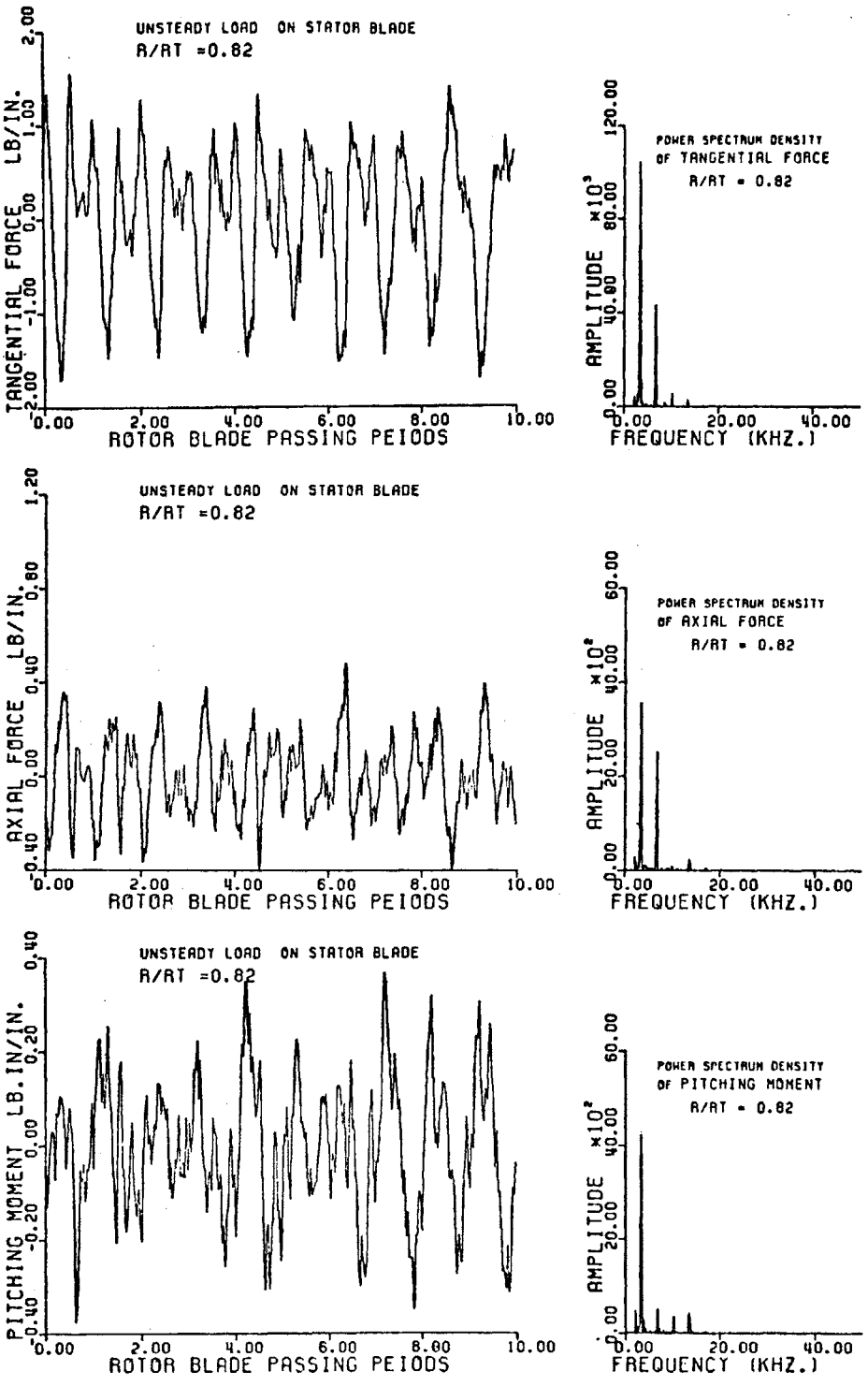

FIG. 4-47 Unsteady Loads on Stator Blade, $R/R_T = 0.82$

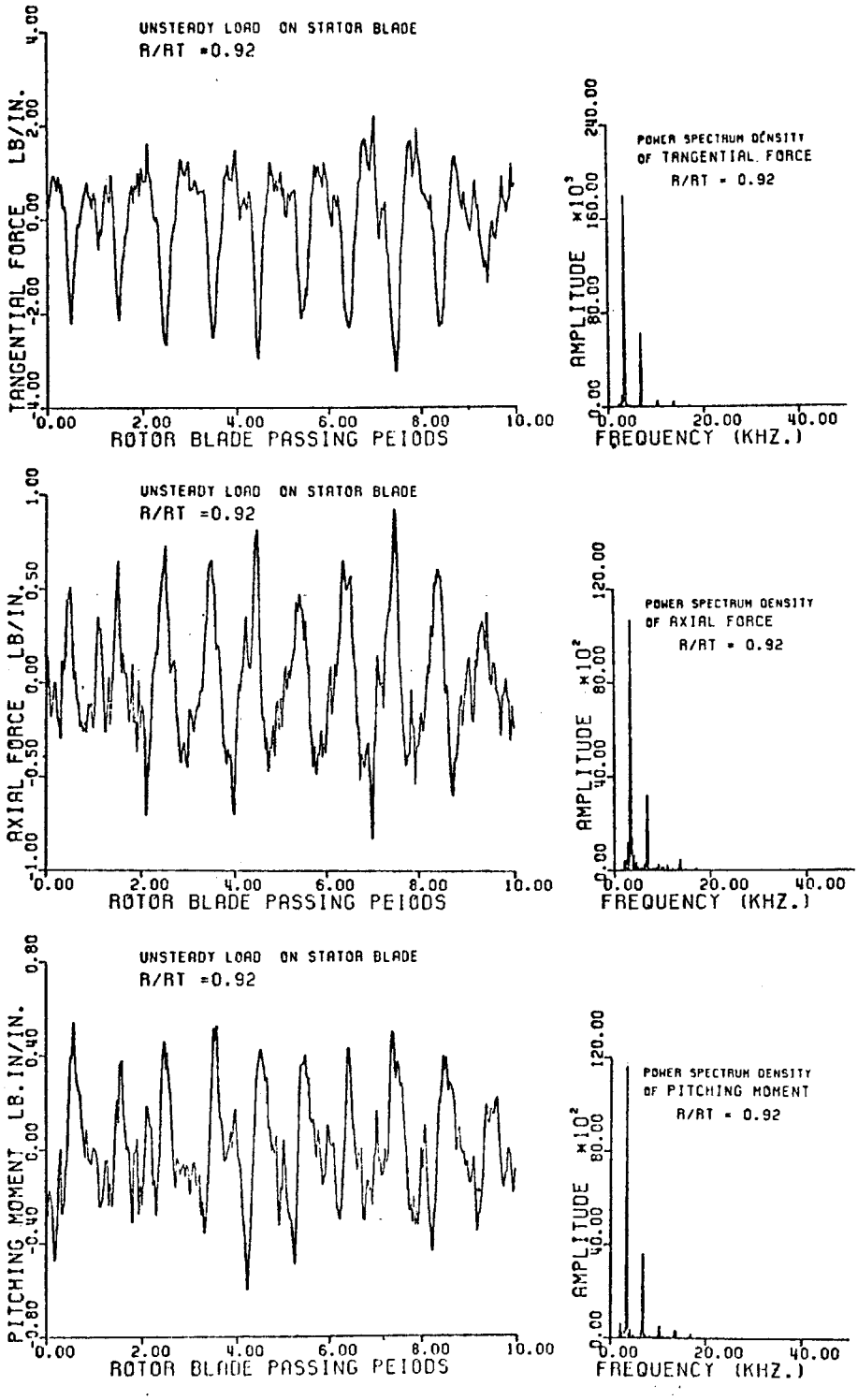

FIG. 4-48 Unsteady Loads on Stator Blade, $R/R_T = 0.92$

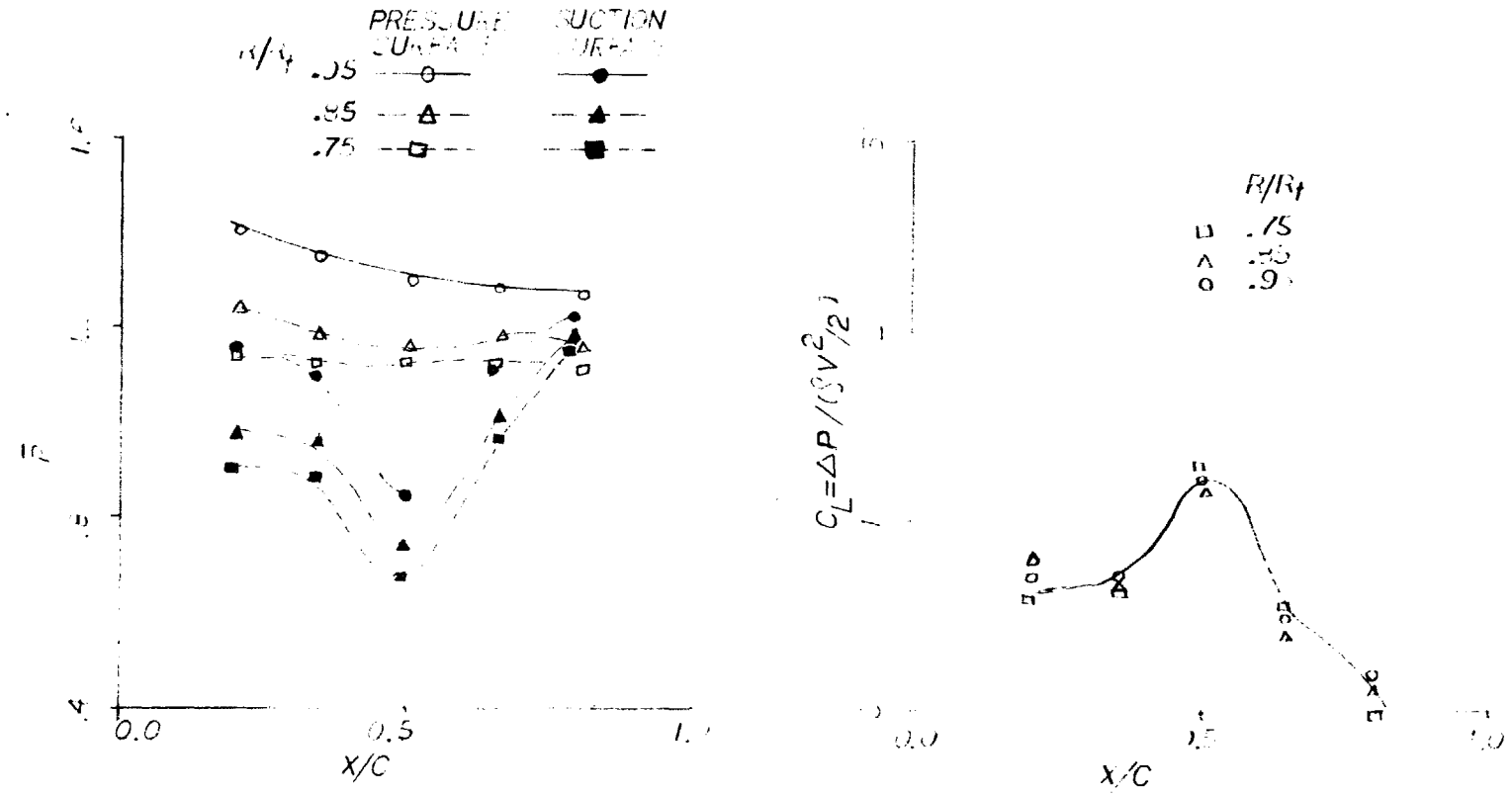

FIG. 4-49 Stator's Chordwise Distribution of Steady State Pressure and Lift Coefficient

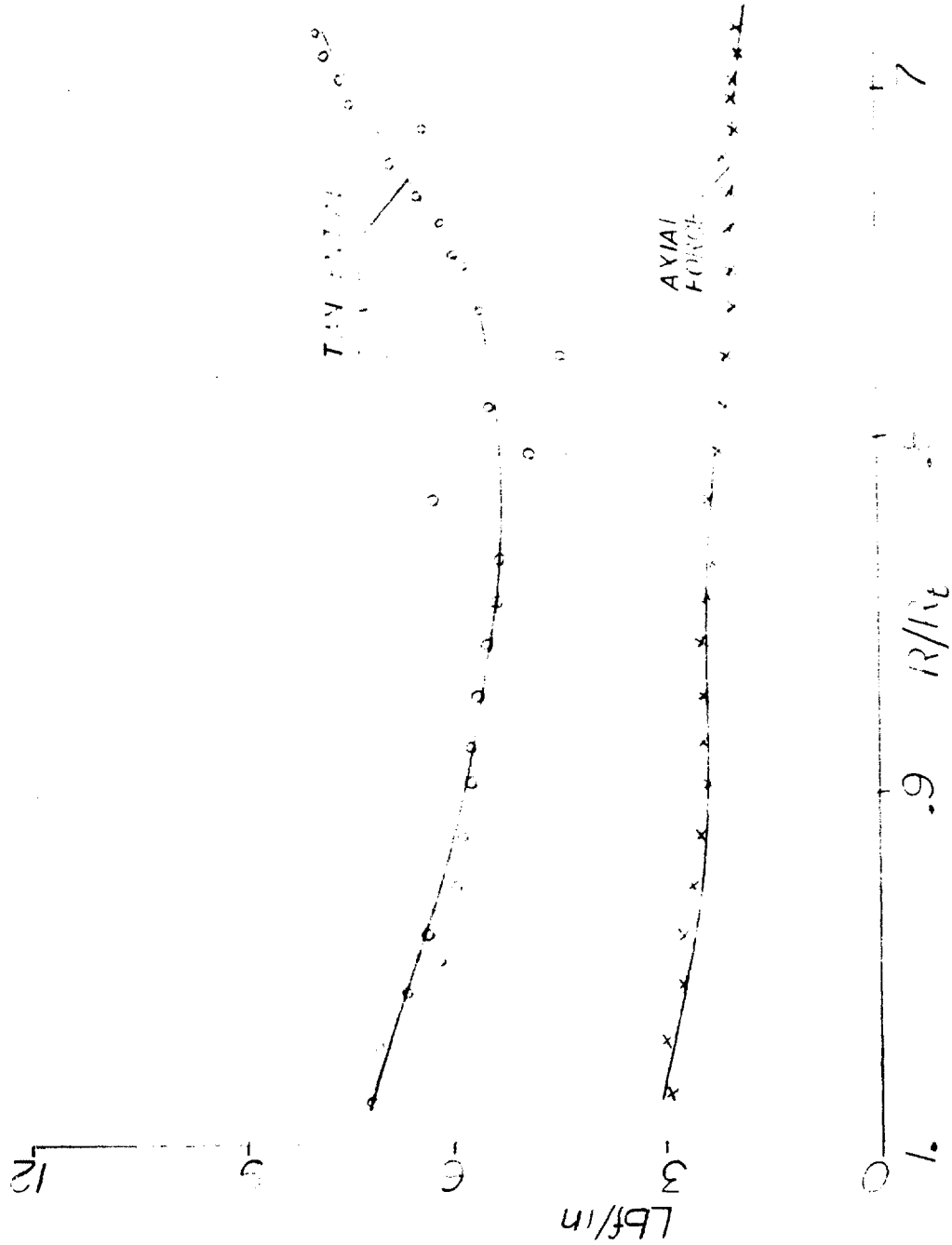

FIG. 4-50 Steady State Tangential and Axial Forces on Stator Blade vs. Radius

APPENDIX A

CALCULATION OF EFFICIENCY

The total-to-total adiabatic efficiency for a compressor rotor is

$$\eta = \frac{(P_{t2}/P_{t1})^{\frac{\gamma-1}{\gamma}} - 1}{(T_{t2}/T_{t1}) - 1} \tag{A1}$$

where subscripts 1 and 2 denote upstream and downstream of the rotor. The calculation of efficiency requires both total pressure and total temperature to be measured. It is not possible to measure total temperature in the Blowdown Facility, instead the Eulers equation is used to calculate total temperature rise across the rotor.

$$T_{t2} - T_{t1} = \frac{\Delta(r\ \omega\ V_\theta)}{cp}$$

or

$$T_{t2}/T_{t1} - 1 = \frac{r\ \omega\ V_{\theta 2}}{cp\ T_{t1}} \tag{A2}$$

The right hand side of A2 can be written as:

$$\begin{aligned} \frac{R\ \omega\ V_{\theta 2}}{cp\ T_{t2}} \cdot \frac{T_{t2}}{T_{t1}} &= \frac{R\ \omega\ V_\theta}{cp\ T_2(1 + \frac{\gamma-1}{2} M_2^2)} \cdot \frac{T_{t2}}{T_{t1}} \\ &= \frac{\gamma R\ (R\ \omega\ V\theta_2)}{cp(\gamma R T_2)(1 + \frac{\gamma-1}{2} M_2^2)} \cdot \frac{T_{t2}}{T_{t1}} \end{aligned} \tag{A3}$$

but speed of sound $a = \sqrt{\gamma RT}$ and

$$R\omega = \frac{R}{R_t} R_t\omega = \frac{R}{R_t} U_t$$

where U_t is the rotor tip speed. From Eqs. (A2) and (A3) we get

$$\frac{T_{t2}}{T_{t1}} = \frac{1}{1 - \dfrac{(\gamma-1)M_t M_{\theta 2}(R/R_t)}{(1 + \frac{\gamma-1}{2} M_2^2)}}$$

Therefore

$$\eta = \frac{\dfrac{(P_{t2}/P_{t1})^{\frac{\gamma-1}{\gamma}} - 1}{(\gamma-1) M_t M_{\theta 2} R/R_t}}{(1 + \frac{\gamma-1}{2} M_2^2) - (\gamma-1) M_t M_{\theta 2} R/R_t}$$

APPENDIX B

MASS FLOW CALCULATION

The mass flow through the rotor can be calculated four different ways. These four methods are as follows:

i) The rate of change of pressure in the supply tank is related to the mass flow as

$$\dot{w} = \frac{v}{(1+\delta)\, a_{10}^2} \left(\frac{T_{10}}{T_1} \right) \frac{dp_1}{dt}$$

where v is the supply tank volume, δ is percent of flow through the boundary layer bled, a_{10} and T_{10} are the temperature and speed of sound in the supply tank in the beginning of the test and p_1 and T_1 are supply tank pressure and temperature.

ii) Calculation of rotor inlet Mach number M_2 from pressure measurement upstream of the rotor leads to

$$\dot{w} = \frac{\gamma p_2 A_2}{a_{10}} \sqrt{\frac{2}{\gamma-1} \left(\frac{T_{10}}{T_1} \right) \left(\frac{p_1}{p_2} \right)^{\frac{\gamma-1}{\gamma}} \left[\left(\frac{p_1}{p_2} \right)^{\frac{\gamma-1}{\gamma}} - 1 \right]}$$

where 1 and 2 denote supply tank and rotor upstream conditions, respectively.

iii) Calculation of mass flow through the choked throttle orifice using the measured value of p_3, pressure upstream of the orifice gives

$$\dot{w} = \frac{\gamma p_3 A^*}{a_3} \left[\left(\frac{2}{\gamma+1} \right) \left(1 + \frac{\gamma-1}{2} M_3^2 \right) \right]^{\frac{\gamma+1}{2(\gamma-1)}}$$

where A^* is the orifice area and M_3 is determined by the area ratio A^*/A_3 .

iv) Radial integration of flow quantities measured by the 5-way probe leads to

$$\dot{w} = \int_{R_h}^{R_t} 2\pi R \, \rho \, V_x \, dr \tag{B4}$$

But

$$\rho \, v_x = \frac{p}{RT} V_x = \sqrt{\frac{\gamma}{R}} \frac{M_x p}{\sqrt{T}} \tag{B5}$$

$$T_2 = \frac{T_{t2}}{\left(1 - \frac{\gamma-1}{2} M^2 \right)} \tag{B6}$$

$$\eta_r = \frac{\left(P_{t2}/P_{t1} \right)^{\frac{\gamma-1}{\gamma}} - 1}{\left(T_{t2}/T_{t1} \right) - 1} \tag{B7}$$

Combining Eqs. (B6) and (B7) we get

$$T_2 = \frac{T_{t1} \left[1 + \left(P_{t2}/P_{t1} \right)^{\frac{\gamma-1}{\gamma}} - 1 \right)/\eta_r]}{1 + \frac{\gamma-1}{2} M^2}$$

The mass flow can then be computed from the measured Mach numbers and pressure ratios

$$\dot{w} = 2\pi R_t^2 \sqrt{\frac{\gamma}{R}} \int_h^t \left(\frac{R}{R_t}\right) \frac{M_x p}{\sqrt{T}} \, d\left(\frac{R}{R_t}\right) \quad .$$